2025-09-05

Toward realistic elements for long-distance quantum networks with solid-state spin systems

Taherizadegan, Shahrzad

UNIVERSITY OF CALGARY

Toward realistic elements for long-distance quantum networks with solid-state spin systems

by

Shahrzad Taherizadegan

A THESIS
SUBMITTED TO THE FACULTY OF GRADUATE STUDIES
IN PARTIAL FULFILLMENT OF THE REQUIREMENTS FOR THE
DEGREE OF DOCTOR OF PHILOSOPHY

GRADUATE PROGRAM IN PHYSICS AND ASTRONOMY

CALGARY, ALBERTA
SEPTEMBER, 2025

Abstract

Future global quantum networks, which rely on the ability to transfer quantum information over long distances, will enable various applications, including secure communication, distributed quantum computing, and new fundamental tests of quantum physics. While photons are ideal carriers of quantum information, transmission loss in communication channels and the no-cloning theorem, which prohibits quantum state amplification, led to the proposal of quantum repeaters to extend the range of quantum communication. They generate entanglement, store it over short distances, and extend it through entanglement swapping. To distribute entanglement over long distances, quantum repeaters require interfaces between flying qubits (photons) and stationary qubits (matter). The entangled quantum state remains stored in quantum memory until successful entanglement is established between two adjacent links. Quantum memories are also crucial in various other aspects of quantum technologies. Furthermore, performing quantum gates between stationary qubits is essential not only for processing quantum information in quantum computing but also for quantum repeaters to enable the generation, storage, and swapping of entanglement, which are fundamental to repeater functionality.

Solid-state spin systems provide a promising platform for implementing stationary qubits in quantum networks. In this thesis, we focus on advancing realistic components for such networks by studying two complementary approaches to quantum memory: ensemble-based and single-emitter-based systems. Both approaches enable the implementation of stationary qubits, but in different ways. First, we develop a theoretical model for a cavity-enhanced atomic frequency comb (AFC) quantum memory, which is an ensemble-based scheme implemented using a Tm:YAG crystal. Our model incorporates the effects of dispersion and shows good agreement with experimental results. It provides a semi-quantitative description of memory efficiency, describes its dependence on detuning, and captures certain qualitative features of experimental reflectivity, contributing to the practical prediction of the performance of cavity-enhanced AFC quantum memory.

In the second part of the thesis, we turn to single-emitter-based platforms. Motivated by the growing interest in T center defects in silicon, we investigate the feasibility of implementing various quantum gate schemes between individual T centers, including two probabilistic photon interference-based schemes, a near-deterministic photon scattering gate, and a deterministic magnetic dipole-based scheme. We analyze and quantify their performance while accounting for real-world imperfections to compare their potential based on current and near-future experimental capabilities. Our results indicate that probabilistic interference-based schemes are the most promising for T centers, with the photon interference-based scheme with feedback enabling the simultaneous achievement of high efficiency and fidelity in the near to medium term.

Preface

The following is a list of published and forthcoming journal papers resulting from my PhD research. This thesis includes material from papers 1 and 2. Both works were accomplished as part of a collaborative effort with several co-authors. Copyright permissions are provided in appendix A.

In addition, we collaborated with the experimental group at Simon Fraser University, which led to paper 3; however, that part of the work is not included in this thesis.

1. Shahrzad Taherizadegan, Jacob H. Davidson, Sourabh Kumar, Daniel Oblak, and Christoph Simon. *Towards a realistic model for cavity-enhanced atomic frequency comb quantum memories. Quantum Science and Technology, 9(3):035049, 2024.*

2. Shahrzad Taherizadegan, Faezeh Kimiaee Asadi, Jia-Wei Ji, Daniel Higginbottom, and Christoph Simon. *Exploring the feasibility of probabilistic and deterministic quantum gates between T centers in silicon. arXiv:2508.06474, 2025.*

3. Camille Bowness, Simon A. Meynell, Michael Dobinson, Chloe Clear, Kais Jooya, Nicholas Brunelle, Mehdi Keshavarz, Katarina Boos, Melanie Gascoine, Shahrzad Taherizadegan, Christoph Simon, Mike L. W. Thewalt, Stephanie Simmons, Daniel B. Higginbottom. *Laser-induced spectral diffusion and excited-state mixing of silicon T centres. arXiv:2504.09908, 2025.*

Below is a list of published and forthcoming peer-reviewed conference papers based on my PhD research.

1. Shahrzad Taherizadegan, Jacob H. Davidson, Sourabh Kumar, Roohollah Ghobadi, Daniel Oblak, and Christoph Simon. *Demonstration of a Model for Cavity-Enhanced Atomic Frequency Comb Quantum Memory. Quantum 2.0 Conference, QM4B.6, 2022.*

2. Shahrzad Taherizadegan, Sourabh Kumar, Jacob H. Davidson, Daniel Oblak, and Christoph Simon. *The Role of Dispersion in Cavity-Enhanced Atomic Frequency Comb Quantum Memories. Quantum 2.0 Conference, QM4C.6, 2023.*

3. Shahrzad Taherizadegan, Jacob H. Davidson, Sourabh Kumar, Daniel Oblak, and Christoph Simon. *Towards a Realistic Model for Cavity-Enhanced Atomic Frequency Comb Quantum Memories: The Critical Role of Dispersion. APS March Meeting Abstracts, LL03.001, 2024.*

4. Shahrzad Taherizadegan, Jacob H. Davidson, Sourabh Kumar, Daniel Oblak, and Christoph Simon. *Towards a Realistic Model for Cavity-Enhanced Atomic Frequency Comb Quantum Memories. IEEE Photonics Conference, Published in IEEE Xplore, 2024.*

5. Shahrzad Taherizadegan, Faezeh Kimiaee Asadi, Jia-Wei Ji, Daniel Higginbottom, and Christoph Simon. *Exploring the Feasibility of Various Quantum Gates Between T Centers in Silicon. Photonics for Quantum 13563, 24-30, 2025*

Acknowledgements

I would like to express my heartfelt gratitude to my supervisor Prof. Christoph Simon for his invaluable guidance, support, and thoughtful insights throughout this journey. His patience, encouragement, and belief in me played a vital role in both the progress of this work and my personal growth as a researcher. I am also grateful to all my teachers—from my first day of school to the professors at university—whose inspiration and passion for learning sparked my curiosity about nature and led me to the fascinating world of physics.

I sincerely thank Dr. Daniel Oblak, Prof. Barry Sanders, Dr. Shabir Barzanjeh, Dr. Erika Janitz, Dr. Shahpoor Moradi, and Dr. Lindsay LeBlanc for their insightful feedback, support, and for serving on my supervisory and examination committees. I am also deeply thankful to Dr. Jacob Davidson, Dr. Faezeh Kimiaee Asadi, Dr. Sourabh Kumar, Dr. Jiawei Ji, Dr. Daniel Oblak, and Dr. Daniel Higginbottom for valuable discussions and enriching collaborations.

I am immensely grateful to my family for their love and support throughout this journey: my parents, Saeed and Marzieh, and my only sister, Mehrzad, who always encouraged me to keep moving forward, despite the hardship of our separation and the distance between us. I also wish to express my deepest appreciation to my spouse, Meisam, who has always given me the love and strength to persevere. Without his daily sacrifices and inspiration, I could not have come this far.

Above all, I want to acknowledge with deepest gratitude the true light of my life — the one before all and beyond all — who never let me give up, even in the darkest moments.

Table of Contents

List of Figures and Illustrations

List of Tables

Chapter 1

Introduction

Exploiting the unique properties of quantum physics in information science has paved the way for quantum information processing, unlocking possibilities that were once mere dreams. A crucial milestone in advancing quantum information technology is the development of long-distance quantum networks [1, 2, 3, 4], which enable secure communication [5, 6, 7], distributed quantum computing [8], and novel fundamental tests of quantum physics [9]. In the long term, these advancements lay the foundation for the realization of a quantum internet, a global network of interconnected quantum processors [10, 11]. Long-distance quantum communication is limited by the inevitable loss of photons in transmission channels. Unlike classical communication, this loss cannot be compensated through amplification due to the no-cloning theorem [12]. To address this challenge, quantum repeaters have been proposed as a solution [13, 14, 15] where they distribute entanglement over long distances employing interfaces between flying qubits (photons) and stationary qubits (matter). Quantum memories store the entangled quantum states until entanglement is successfully established between two adjacent links, playing a crucial role in synchronizing entanglement distribution across the network to enable long-distance quantum communication [16, 17]. There are two complementary approaches for implementing quantum memories: ensemble-based systems and single-emitter-based systems. While both approaches aim to store quantum

states, there are differences in their physical implementation. Ensemble-based systems rely on the collective interaction of the atoms or ions in the ensemble which can lead to high multimode capacity and strong light-matter coupling through collective enhancement at the cost of limited control at the single-atom level. However, single-emitter-based systems such as color centers, allow individual addressing and precise control of qubits, typically with reduced storage capacity and weaker light-matter interaction compared to ensembles.

The aim of the works done in this thesis is to advance practical elements for quantum networks. Among the various protocols for implementing quantum memories, atomic frequency comb (AFC) quantum memory—a scheme that stores photons in a spectrally comb-shaped ensemble and retrieves them via a collective rephasing—is a promising candidate for quantum repeater applications [18]. Its efficiency is enhanced by placing the AFC inside an asymmetric optical cavity [19, 20]. However, the absence of a comprehensive theoretical model for cavity-enhanced AFC quantum memory makes it challenging to compare experimental results with theory and to infer system parameters from experiments. To address this, we develop a theoretical model for cavity-enhanced atomic frequency comb (AFC) quantum memory, contributing to the accurate predictions of its performance.

Following our work on quantum memories and in light of recent growing interest in T centers in silicon, we also explore the implementation of quantum gates between stationary qubits (single-atom memories), which are essential not only for quantum computing [21, 22, 23], but also for enabling entanglement generation, storage, and swapping in quantum repeaters [15, 24]. We investigate various quantum gate schemes between single T centers in silicon, quantifying their performance while accounting for real-world imperfections, and evaluating and comparing them based on current and near-future experimental capabilities.

The thesis is organized as follows: In chapter 1, I will provide some of the fundamental principles of quantum communication and networks. In chapter 2, I discuss key aspects of quantum networks, including the elements required to realize them and their potential

applications. Chapter 3 focuses on the physical platforms used to implement the elements of quantum networks, with particular emphasis on those explored in this thesis. Chapters 4 and 5 present two papers that form the core of this work. Finally, chapter 6 concludes the thesis and offers an outlook on future directions.

1.1 Quantum bits (Qubits) and Bloch sphere representation

In classical information science, information is encoded and represented using binary states (bit) 0 or 1. This principle originates from classical physics, where a system exists in a well-defined state—analogous to a cat being either alive or dead. However, the state of a quantum system can be much more complex than simply being 0 or 1. Therefore, quantum information science introduces the quantum bit (qubit) as the fundamental unit of information. Unlike classical bits, a qubit can exist in a combination of both 0 and 1 simultaneously, as allowed by the principles of quantum mechanics. This is similar to Schrödinger's cat which can be dead, alive or in a superposition of both states [25]. A pure state $|\psi\rangle$ of a two level quantum system (qubit) can be expressed in the computational basis as

$$|\psi\rangle = a|0\rangle + b|1\rangle \tag{1.1}$$

where a and b are complex numbers representing the probability amplitudes. Since the probabilities of being in states $|0\rangle$ and $|1\rangle$ are $|a|^2$ and $|b|^2$, respectively, and the total probability must sum to 1, $|a|^2+|b|^2 = 1$. As the global phase of a quantum state is irrelevant and only the relative phase matters, the unit probability condition suggests representing the qubit state using two free parameters: the polar angle ($0 \leq \theta \leq \pi$) and the azimuthal angle ($0 \leq \phi < 2\pi$). This representation helps visualize the state of a qubit on a three-dimensional sphere called the Bloch sphere, where the state is represented by a Bloch vector (see figure 1.1), which is written as

$$|\psi\rangle = \cos\frac{\theta}{2}|0\rangle + e^{i\phi}\sin\frac{\theta}{2}|1\rangle. \tag{1.2}$$

The north pole of this unit sphere represents the state $|0\rangle$, while the south pole represents the state $|1\rangle$. A qubit can exist at any point on the surface of this sphere, while classical

bits are limited to the north or south poles.

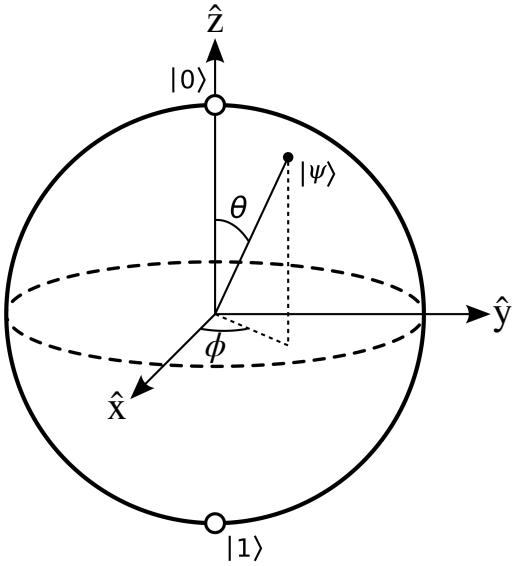

Figure 1.1: Visualization of a qubit state on the Bloch sphere. The state of any two-level quantum system can be represented as a point on the Bloch sphere, with the Bloch vector $|\psi\rangle$ describes the qubit's state in three-dimensional space.

So far, I have discussed pure states, which represent precise and well-defined quantum states about which we have complete information. However, in realistic open quantum systems, we often encounter mixed states, which describe situations where we lack complete knowledge of the system. A mixed state represents a statistical ensemble of different pure states, each occurring with a certain probability. Mixed states are described by a density matrix ρ rather than a state vector $|\psi\rangle$, which provides a unified framework for representing both pure and mixed states. A general mixed state, composed of pure states $|\psi_i\rangle$ with corresponding probabilities p_i, is written as

$$\rho = \sum_i p_i |\psi_i\rangle\langle\psi_i| \tag{1.3}$$

where the probabilities $0 \leq p_i \leq 1$ and $\sum_i p_i = 1$. For a pure state, the density matrix satisfies $\mathrm{Tr}(\rho^2) = 1$, while for mixed states, $\mathrm{Tr}(\rho^2) < 1$, reflecting a loss of coherence or purity. In the Bloch sphere representation, pure states lie on the surface of the sphere, while mixed states correspond to points inside the sphere. The distance from the center, i.e., the

length of the Bloch vector indicates the degree of purity, with states closer to the surface being more pure.

1.2 No-cloning theorem

In classical physics, the concept of cloning or copying information is natural and unproblematic. For instance, classical bits can be duplicated to create backups in computers, or copied and amplified to overcome losses in transmission channels. However, this is not the case in quantum physics. The no-cloning theorem [12, 26, 27, 28] states it is fundamentally impossible to make a perfect copy of an arbitrary unknown quantum state. Considering an unknown state $|\psi\rangle$, there is no quantum operation that can take $|\psi\rangle$ and make two copies of it. The authors in Ref. [12] proved the no-cloning theorem by employing the linearity of quantum mechanics, while later work in Ref. [29] provided a proof based on the properties of unitary evolution. Let us assume the existence of a universal cloning machine represented by a unitary operator $\hat{U}$, which can copy any arbitrary quantum state $|\psi\rangle$ and would satisfy

$$\hat{U}\left(|\psi\rangle \otimes |0\rangle\right) = |\psi\rangle \otimes |\psi\rangle\,. \tag{1.4}$$

In principle, the cloning machine would be capable of producing a copy of any quantum state. Now, consider two different input states, $|\psi\rangle$ and $|\varphi\rangle$. The cloning machine operation would result in

$$\hat{U}\left(|\psi\rangle \otimes |0\rangle\right) = |\psi\rangle \otimes |\psi\rangle\,, \tag{1.5}$$

$$\hat{U}\left(|\varphi\rangle \otimes |0\rangle\right) = |\varphi\rangle \otimes |\varphi\rangle\,. \tag{1.6}$$

If one applies $\hat{U}$ to a superposition of the two states, then

$$\hat{U}\left(\frac{1}{\sqrt{2}}(|\psi\rangle + |\varphi\rangle) \otimes |0\rangle\right), \tag{1.7}$$

by the linearity of quantum mechanics, equation 1.7 must equal

$$\frac{1}{\sqrt{2}}\hat{U}\left(|\psi\rangle \otimes |0\rangle\right) + \frac{1}{\sqrt{2}}\hat{U}\left(|\varphi\rangle \otimes |0\rangle\right) = \frac{1}{\sqrt{2}}\left(|\psi\rangle \otimes |\psi\rangle + |\varphi\rangle \otimes |\varphi\rangle\right). \tag{1.8}$$

However, this is not the same as cloning the superposition state itself that is

$$\left(\frac{1}{\sqrt{2}}(|\psi\rangle + |\varphi\rangle)\right) \otimes \left(\frac{1}{\sqrt{2}}(|\psi\rangle + |\varphi\rangle)\right) = \frac{1}{2}\left(|\psi\rangle \otimes |\psi\rangle + |\psi\rangle \otimes |\varphi\rangle + |\varphi\rangle \otimes |\psi\rangle + |\varphi\rangle \otimes |\varphi\rangle\right). \tag{1.9}$$

The two expressions 1.8 and 1.9 are generally not equal unless either $|\psi\rangle = |\varphi\rangle$ or $\langle\psi|\varphi\rangle = 0$ [28, 27]. This contradiction shows that cloning an arbitrary unknown quantum state violates the linearity of quantum mechanics. Therefore, no such universal unitary cloning operator $\hat{U}$ can exist. The impossibility of cloning mixed quantum states was later established by [30]. Although perfect cloning of an arbitrary unknown quantum state is forbidden by the no-cloning theorem, one can still create imperfect copies with the maximum achievable fidelity of 0.83 [31].

The no-cloning theorem underpins the security of quantum key distribution (QKD) protocols such as BB84 [6], as it prevents eavesdropping on quantum information in transmission channels without disturbing it. Conversely, it prohibits cloning and amplification of transmitted quantum states posing significant challenges for long-distance quantum communication. As a result, quantum entanglement is used as a resource to perform a variety of quantum tasks. In particular, quantum repeaters [13, 14, 15] employ entanglement swapping to extend secure communication distance without violating the no-cloning theorem.

1.3 Quantum entanglement

Entanglement is one of the fundamental features of quantum physics, with no counterpart in classical mechanics. It refers to a non-classical correlation between two or more particles,

independent of the distance between them [32]. In an entangled system of particles, it is impossible to describe the quantum state of the entire system as a tensor product of the individual quantum states. In the case of mixed states, the whole quantum state cannot be expressed as a convex combination of product states. The state of two unentangled quantum systems can be written as a separable state

$$|\psi\rangle_{A,B} = |\psi\rangle_A \otimes |\psi\rangle_B$$

Two separable mixed states can be written as

$$\rho_{A,B} = \sum_i p_i \, \rho_A^{(i)} \otimes \rho_B^{(i)}$$

where p_i are the corresponding probabilities, with the condition that $\sum_i p_i = 1$. The state of two qubits can be in any linear combination of basis states $|00\rangle$, $|01\rangle$, $|10\rangle$, and $|11\rangle$. If we have two particles in the state

$$\frac{1}{\sqrt{2}} \left(|1\rangle_A |0\rangle_B + |0\rangle_A |1\rangle_B \right)$$

it is not possible to express this state as a separable state, as shown in equation (1.3), implying that the two qubits are entangled. When the first qubit is measured to be in the state $|1\rangle_A$, the state of the second qubit is instantaneously projected into the state $|0\rangle_B$. However, prior to the measurement, the second qubit exists in a superposition of both $|0\rangle_B$ and $|1\rangle_B$ states, corresponding to equal probabilities of $\frac{1}{2}$.

The instantaneous projection of a quantum state cannot be explained by any signal traveling between the two particles to transmit information as such communication would be constrained by the speed of light. Moreover, since the outcomes are inherently random, it is impossible to control the result on one side to send a message to the other. This phenomenon violates local realism, and was first highlighted in the EPR paradox [33], which pointed out the apparent contradiction between the principles of quantum entanglement and

local realism, ultimately arguing against the completeness of quantum mechanics. Therefore, local hidden variable (LHV) theories were proposed as a trial to restore classical intuitions of realism and localism to quantum physics. However, subsequent work by Bell and others [34, 35] demonstrated that LHV theories cannot fully reproduce all the statistical predictions of quantum mechanics. In particular, both Bell's inequality and the Clauser-Horne-Shimony-Holt (CHSH) inequality are violated by quantum correlations which has been consistently confirmed in numerous quantum experiments [36, 37, 38, 39, 40, 41].

These experimental validations have established entanglement as an intrinsically quantum phenomenon that defies classical explanation. Entanglement transforms a group of particles into a unified quantum system, where the individual components can no longer be described as independent entities. As a foundational resource in quantum information science, entanglement plays a central role in enabling quantum networks, where significant effort is dedicated to generating and distributing entanglement between distant quantum systems.

1.4 Bell-state measurement

The maximally entangled states known as Bell states are

$$
\begin{aligned}
|\Phi^+\rangle &= \frac{1}{\sqrt{2}}\left(|00\rangle + |11\rangle\right) \\
|\Phi^-\rangle &= \frac{1}{\sqrt{2}}\left(|00\rangle - |11\rangle\right) \\
|\Psi^+\rangle &= \frac{1}{\sqrt{2}}\left(|01\rangle + |10\rangle\right) \\
|\Psi^-\rangle &= \frac{1}{\sqrt{2}}\left(|01\rangle - |10\rangle\right)
\end{aligned}
$$

which form a complete orthonormal basis for two-qubit space. One simple way to generate Bell states is through performing a Hadamard ($\hat{H}$) gate and a Controlled-NOT (CNOT) gate on the input (see section 2.3 in chapter 4.1). For example if one take the computational

basis $|00\rangle$ as the input

$$|00\rangle \xrightarrow{\hat{H}\otimes I} \left(\frac{1}{\sqrt{2}}(|0\rangle + |1\rangle)\right) \otimes |0\rangle = \frac{1}{\sqrt{2}}(|00\rangle + |10\rangle)$$
$$\xrightarrow{\text{CNOT}} \frac{1}{\sqrt{2}}(|00\rangle + |11\rangle) = |\Phi^+\rangle$$

Thus, the final state after these operations is the Bell state

$$|\Phi^+\rangle = \frac{1}{\sqrt{2}}(|00\rangle + |11\rangle)$$

A Bell-state measurement is a joint quantum measurement on two qubits in the Bell basis that projects the system's state onto one of the Bell states. A partial Bell state measurement can be done by sending a pairs of encoded photons (p_a, p_b) entering the two input ports a and b of a Beam splitter (BS). Their encoded state belongs to the four dimentional state of a two qubit system. In principle one can encode quantum information in various degrees of freedom of photons such as polarization, frequency, and arrival time (early or late). To complete the Bell-state measurement, two measurement devices are put at the two output ports of the beam splitter that are capable of distinguishing between two orthogonal modes of the degree of freedom used to encode the qubits (for example, for polarization-encoded photons, the measurement device at each port can be a polarizing beam splitter followed by two detectors). The unitary operation associated with a 50:50 beam splitter acting on two input modes is given by $U_{\text{BS}} = \frac{1}{\sqrt{2}} \left(\begin{smallmatrix} 1 & i \\ i & 1 \end{smallmatrix} \right)$. The input creation operators are related to the output creation operators via the following beam splitter transformation

$$\begin{pmatrix} \hat{a}_c^\dagger \\ \hat{a}_d^\dagger \end{pmatrix} = \frac{1}{\sqrt{2}} \begin{pmatrix} 1 & i \\ i & 1 \end{pmatrix} \begin{pmatrix} \hat{a}_a^\dagger \\ \hat{a}_b^\dagger \end{pmatrix}$$

Merging the photons at a beam splitter (BS) erases any which-path information. Applying the unitary operator U_{BS} to the input photon states results in their projection onto one

of the Bell states. If the output modes of the BS are denoted by c and d, the action of the BS operator on the Bell states is given by [42, 43]

$$
\begin{aligned}
|\Psi^+\rangle_{a,b} &= \frac{1}{\sqrt{2}}\left(|01\rangle_{a,b} + |10\rangle_{a,b}\right) \rightarrow \frac{i}{\sqrt{2}}\left(|01\rangle_{c,c} + |10\rangle_{d,d}\right) \\
|\Psi^-\rangle_{a,b} &= \frac{1}{\sqrt{2}}\left(|01\rangle_{a,b} - |10\rangle_{a,b}\right) \rightarrow \frac{1}{\sqrt{2}}\left(|01\rangle_{c,d} - |10\rangle_{c,d}\right) \\
|\Phi^\pm\rangle_{a,b} &= \frac{1}{\sqrt{2}}\left(|00\rangle_{a,b} \pm |11\rangle_{a,b}\right) \rightarrow \frac{i}{2}\left(|00\rangle_{c,c} + |00\rangle_{d,d} \pm |11\rangle_{c,c} \pm |11\rangle_{d,d}\right).
\end{aligned}
$$

Where $|0\rangle$ and $|1\rangle$ can be associated with the two orthogonal modes of the polarization-encoded photons. Thus, detecting photons simultaneously in orthogonal states $|0\rangle$ and $|1\rangle$ from different output ports of the beam splitter results in a projection into the $|\Psi^-\rangle$ state. Conversely, detecting photons in orthogonal states but from the same output port leads to a projection into the $|\Psi^+\rangle$ state. We can see that this measurement setup cannot distinguish between the other two Bell states, $|\Phi^+\rangle$ and $|\Phi^-\rangle$, but they can still be distinguished from the $|\Psi^+\rangle$ and $|\Psi^-\rangle$ states. Since only two of the four Bell states can be identified through the measurement outcomes, the maximum success rate for this scheme which is limited to linear optics without additional resources is 50%. In principle, the maximum success rate can be increased by methods such as using ancillary photons [44, 45] experimentally demonstrated in [46]. While the success probability can approach unity with more complex ancillary states, this comes at the expense of greater experimental complexity, and the need for multi-photon detection, limiting their practicality. Bell state measurements play an important role in quantum information processing tasks such as quantum teleportation and entanglement swapping discussed in the following sections.

1.5 Quantum teleportation

Quantum teleportation is an important method that enables the transfer of quantum information, such as the state of a qubit, from one location to another without physically moving the particle itself. It relies on the principles of quantum entanglement and classical

communication. Suppose that we want to teleport a quantum state $|q\rangle_C = \alpha|0\rangle_C + \beta|1\rangle_C$ from Alice to Bob. The protocol starts with Alice and Bob sharing a maximally entangled Bell state. This shared state is predetermined by mutual agreement between them and can be any of the four Bell states. The specific choice does not affect the outcome. As shown in figure 1.2, we assume the shared state is Φ^+_{AB} in the teleportation protocol. At this point, Alice possesses two particles, the one she intends to teleport, C, and A, which is part of the entangled pair, while Bob holds the third particle, B.

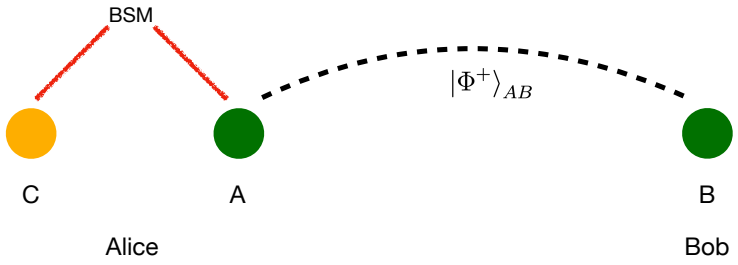

Figure 1.2: Quantum teleportation protocol illustrating the transfer of an unknown quantum state $|q\rangle_C$ from Alice to Bob, facilitated by the shared entangled state $|\Phi^+\rangle_{AB}$.

The combined quantum state of these three particles is described by

$$|Q\rangle_{CAB} = |q\rangle_C \otimes |\Phi^+\rangle_{AB} = (\alpha|0\rangle_C + \beta|1\rangle_C) \otimes \left(\frac{1}{\sqrt{2}}(|0\rangle_A|0\rangle_B + |1\rangle_A|1\rangle_B)\right)$$

Now, it is most convenient to write the state of Alice's two qubits (A, and C) as a superposition of the Bell basis states. All the two-qubit basis states can be expressed in terms of the Bell states as following

$$|00\rangle = \frac{1}{\sqrt{2}}\left(|\Phi^+\rangle + |\Phi^-\rangle\right)$$

$$|01\rangle = \frac{1}{\sqrt{2}}\left(|\Phi^+\rangle - |\Phi^-\rangle\right)$$

$$|10\rangle = \frac{1}{\sqrt{2}}\left(|\Psi^+\rangle + |\Psi^-\rangle\right)$$

$$|11\rangle = \frac{1}{\sqrt{2}}\left(|\Psi^+\rangle - |\Psi^-\rangle\right)$$

Therefore, the quantum state of the three particles ($|Q\rangle_{CAB}$) can be rewritten in the Bell

basis of particles A and C as

$$|Q\rangle_{CAB} = \frac{1}{2}\big[\,|\Phi^+\rangle_{CA}\,(\alpha\,|0\rangle_B + \beta\,|1\rangle_B) + |\Phi^-\rangle_{CA}\,(\alpha\,|0\rangle_B - \beta\,|1\rangle_B) \\ + |\Psi^+\rangle_{CA}\,(\alpha\,|1\rangle_B + \beta\,|0\rangle_B) + |\Psi^-\rangle_{CA}\,(\alpha\,|1\rangle_B - \beta\,|0\rangle_B)\big] \tag{1.10}$$

As a result of this change, the joint state can be expressed as a superposition of Bell states between C and A, each correlated with a corresponding state of B. At this stage, no interaction has yet occurred between Alice and Bob and the total state is still tripartite and does not represent direct entanglement between C and A, since the overall state is still factorizable. This expression highlights the correlations between C-A and B that enable teleportation: once Alice performs a Bell-state measurement (BSM) on C and A, Bob's qubit collapses into one of the four above superposition states determined by Alice's BSM measurement outcome. Then Alice uses classical communication to inform Bob about her BSM outcome, so that Bob can correct his by applying a unitary operator on his state to obtain the original state that aimed to be teleported to him ($|q\rangle_C$). For example, if the result of BSM is $|\Psi^+\rangle_{CA}$, the correction operator Bob employs to retrieve the original quantum state is Pauli-X (bit-flip) operator. It should be emphasized that the 50% limit on success probability of linear-optical Bell state measurements does not imply a fundamental limitation of quantum teleportation itself. In fact, if Bell state measurements are implemented within a quantum circuit using entangling gates such as a Hadamard followed by a CNOT, all four Bell states can be distinguished, making teleportation deterministic in principle. Since classical communication is a necessary part of the protocol, quantum teleportation cannot be used to transmit information faster than light.

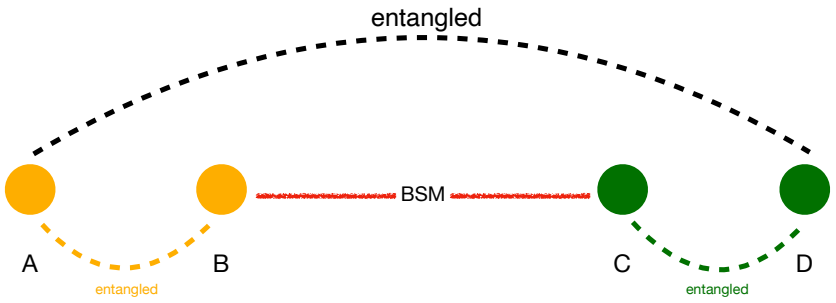

Figure 1.3: Entanglement Swapping: A BSM on the two central particles, B and C, creates entanglement between spatially separated left and right particles, A and D.

1.6 Entanglement swapping

Entanglement swapping is effectively the teleportation of entanglement. It involves two separate pairs of entangled particles. By interfering with one particle from each pair and performing a Bell-state measurement (BSM) on them, the remaining particles—originally unentangled—are projected into an entangled state. For example if the entangled states are $|\Phi^+\rangle_{AB}$ and $|\Phi^+\rangle_{CD}$, it can be shown that the overall state of the system can be expressed as a superposition of maximally entangled pairs between A and D, and, B and C

$$|\Phi^+\rangle_{AB}\,|\Phi^+\rangle_{CD} = \frac{1}{2}\big(\,|\Phi^+\rangle_{AD}\,|\Phi^+\rangle_{BC} + |\Phi^-\rangle_{AD}\,|\Phi^-\rangle_{BC} + |\Psi^+\rangle_{AD}\,|\Psi^+\rangle_{BC} + |\Psi^-\rangle_{AD}\,|\Psi^-\rangle_{BC}\,\big) \tag{1.11}$$

By performing a Bell-state measurement (BSM) on particles B and C, and projecting them into a specific Bell state, such as $|\Psi^+\rangle_{BC}$, particles A and D are correspondingly projected into a Bell state as well, e.g., $|\Psi^+\rangle_{AD}$ (see figure 1.3).

Chapter 2

Quantum networks

In this chapter, I will discuss the key components required to implement quantum networks, with a particular focus on the elements explored in the projects presented in this thesis. I will also highlight potential applications of future quantum networks.

2.1 Quantum repeaters

In the previous chapter, I discussed quantum teleportation and entanglement swapping as fundamental building blocks for quantum repeaters. Quantum communication is made possible through the quantum teleportation scheme, where Alice can send an unknown quantum state to Bob, provided they share an entangled Bell state. Thus, the primary challenge in quantum communication is how to distribute entanglement between two parties, Alice and Bob.

Directly sending photons over long distances is constrained by photon loss and attenuation in the transmission channel. In principle, the transmission efficiency in optical fiber is described by $\eta = e^{(-L/L_{att})}$ which is the result of the Beer-Lambert law. For photons in the telecommunication wavelength range ($1530 - 1565\,\text{nm}$), the attenuation length is $L_{att} = 22\,\text{km}$, which implies that for every $50\,\text{km}$ traveled, the transmittance is reduced to 10% of its previous value [13]. In classical communication, signal loss is mitigated using am-

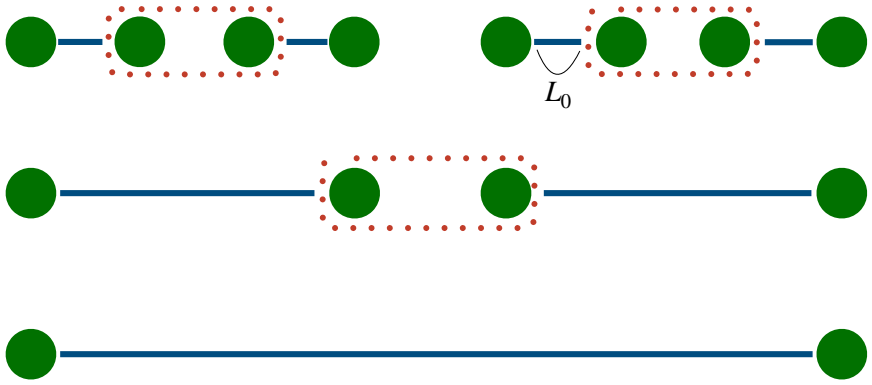

Figure 2.1: The figure illustrates a quantum repeater with four elementary links $N = 4$, each of length L_0, spanning a total distance of L for entanglement distribution. The dark blue dotted squares indicate entanglement swapping between neighboring elementary links, while the green nodes represent the quantum memories required within the repeaters.

plifiers that boost the signal along the channel by regenerating the original signal through duplication. However, classical amplifiers cannot be applied in quantum communication due to the no-cloning theorem discussed in section 1.2, which prohibits the creation of an exact copy of an unknown quantum state. To address this limitation, quantum repeaters have been proposed [14]. Quantum repeaters distribute entanglement across a channel of length L by generating entanglement in smaller elementary links of length $L_0 = L/N$, where N is the number of elementary links. The success of entanglement generation in these links is announced by a heralding signal. Entanglement is then extended to longer distances through entanglement swapping, as discussed in section 1.6 (see figure 2.1). Since entanglement generation and swapping schemes are generally probabilistic, and the linear-optical implementation of BSM has a success probability of at most 50%, it is not feasible to simultaneously generate entanglement across all elementary links. This is where quantum memories become crucial. They store the entanglement created in an elementary link until entanglement is established in the adjacent links. Once this condition is met, entanglement swapping is performed between the quantum memories of neighboring links, thereby extending entanglement across the channel. There have been numerous experimental demonstrations of entangling quantum memories over large distances, including metropolitan-scale implementations span-

ning both two-node configurations and multi-node networks [47, 48, 49, 50, 51, 52, 53]. The most recent breakthrough achieved entanglement between two atomic ensemble quantum memories over a record distance of 420 km via fiber [54]. These accomplishments represent significant progress and foundational demonstrations toward realizing quantum repeaters and developing scalable quantum networks.

2.2 Quantum memory

Optical quantum memory is a device capable of storing and retrieving the quantum states of light, serving as a crucial component for quantum networks, including long-distance quantum communication based on quantum repeaters [55, 3, 16, 17]. Quantum memories allow for the synchronization of probabilistic quantum processes by enabling the temporary storage of quantum states. This capability is vital for the implementation of quantum repeaters and underpins a range of important applications in quantum information science. Quantum memories (QMs) can be broadly categorized into two main types: ensemble-based QMs and single- particle QMs. Ensemble-based quantum memories utilize the collective interaction between light and the atomic ensemble to store quantum information, with no need to monitor individual atomic contributions. This method takes advantage of collective interference effects within the ensemble to enhance the efficiency of the light–matter interface. A variety of protocols have been developed for implementing ensemble-based quantum memories, which will be explored in the following sections. These protocols are realized using different physical platforms, including cold atomic ensembles [53, 47, 56, 57, 58, 59, 60], warm atomic vapors [61, 62, 63, 64, 65, 66], and rare-earth-ion-doped crystals (REICs) [3, 55, 67, 68, 69, 70], each offering unique advantages for quantum storage. The first project in this thesis contributes to developing a model for an ensemble-based cavity-enhanced quantum memory (see chapter 4).

On the other hand, single-particle QMs leverage the interaction between photons and indi-

vidual quantum systems, such as single atoms and ions. To strengthen light–matter coupling, these systems rely on high-quality resonant cavities. A major advantage of single-particle quantum memories is the ability to precisely control individual atomic qubits. Additionally, they are well-suited for single-photon generation, a critical resource for quantum computing and communication. Examples of physical systems used for single-particle quantum storage include single atoms [50, 71, 72, 73, 74], trapped ions [75, 76, 77], and defects in solid-state systems, such as nitrogen-vacancy (NV) centers [51, 78, 79, 80, 81], silicon-vacancy (SiV) centers [82, 52, 83, 84, 85], and single rare-earth ions embedded in solids [86, 87, 88, 89, 90]. More recently, T centers in silicon have also emerged as promising candidates for this goal [91, 92, 93, 94, 95]. The second project in this thesis contributes to analyzing various gate schemes between single T centers.

2.2.1 Figures of merit for quantum memory

There are various metrics to asses the performance of QMs including **efficiency**, **fidelity**, **storage time**, **bandwidth**, and **multimode capacity**. Although remarkable progress has been made in optimizing individual metrics across different platforms, achieving all these requirements simultaneously within a single device remains a major obstacle for all potential candidates.

The overall **efficiency** of a quantum memory is usually defined as the ratio of the energy (or photon number) of the retrieved pulse to that of the pulse initially sent for storage, when both are in the same mode (spectral or temporal). In cases where the memory is intended to modify the recalled photon, for example, by changing its wavelength or temporal profile, the efficiency is defined as the fraction of input photons that are successfully recovered in the desired output mode. An ideal quantum memory has a unit efficiency corresponding to no lost in energy during the storage.

Fidelity is a measure of the similarity between the input and output retrieved states of a quantum memory, with an ideal memory achieving a fidelity of one, indicating an exact

reproduction of the input quantum state. Fidelity can be expressed as $F = \langle\psi|\rho|\psi\rangle$, where $|\psi\rangle$ represents the input quantum state, and ρ is the density matrix of the output state after retrieval from the memory, conditioned on the detection of an emitted single photon.

The **storage time** refers to the duration for which a quantum memory can preserve the quantum state of light. An ideal quantum memory would be capable of storing these quantum states indefinitely and retrieving them on demand. In practice, the storage time—whether for on-demand recall or a predetermined delay—is typically limited by the coherence times of the atomic transitions utilized for memory storage. Long storage times can be achieved through spin-wave storage, where quantum states of photons are mapped onto spin excitations in the ground states, which generally have much longer coherence times. The required storage time varies depending on the application. For quantum repeater applications, it is determined by the time it takes for a photon to travel from a repeater node to a link node. In practical scenarios, it must also be long enough to accommodate the classical communication time between nodes for entanglement swapping and heralding. This typically translates to storage times ranging from milliseconds to seconds, making them suitable for quantum repeaters.

The memory **bandwidth** represents the maximum spectral range over which the memory can efficiently store an input quantum state. It will determine how short the storage pulse is and is crucial for effective integration with quantum light sources [96]. Moreover, for the majority of applications, the memory's storage time needs to be significantly longer than the duration of the stored pulse.

The potential for **multimode capacity** in a quantum memory is a critical figure of merit, characterizing its ability to store multiple independent optical modes simultaneously and efficiently. These modes can span different degrees of freedom, such as temporal, spatial, and frequency domains, significantly enhancing the throughput of quantum communication protocols by enabling parallel storage of quantum states [97]. High multimode capacity is particularly advantageous for probabilistic quantum applications, as it can greatly increase

the rate of successful events. The total multimode capacity is determined by the product of the number of modes across all relevant domains. This capacity scales differently with the optical depth of the memory medium (d), a dimensionless measure of the medium's absorption strength, defined by the product of absorption coefficient and length ($d = \alpha L$), depending on the quantum memory protocol [98]. Moreover, in single-particle quantum memories, multiplexed atom–photon interfaces have been realized by simultaneously addressing multiple atoms arranged within a single device [99, 100]. Among ensemble-based quantum memory approaches, the Atomic Frequency Comb (AFC) protocol is particularly well-suited for multimode storage due to its independence from the optical depth of the storage medium [98]. This property enables AFC memories to achieve large-scale temporal and frequency multiplexing. In the next section, I will discuss the AFC quantum memory protocol in detail.

2.2.2 Atomic frequency comb (AFC) quantum memory

Among various protocols to implement ensemble-based quantum memories, Atomic frequency comb (AFC) quantum memory [18, 101] is a promising candidate in quantum repeaters applications. An AFC memory consists of an ensemble of inhomogeneously broadened atoms that correspond to the absorption line of an atomic transition, spectrally engineered into a periodic series of comb-like peaks with the separation of Δ. This can be done through frequency-selective optical pumping of atoms from the ground state to another ground state which is a metastable state, e.g. a hyperfine state (see figure 4.1 in chapter 4). A resonant input pulse with the bandwidth matches the comb bandwidth is collectively absorbed. After absorption at $t = 0$, photon will be stored as a single excitation, distributed collectively across all the atoms in the ensemble that are resonant with its frequency. The resulting collective state is described by a Dicke state

$$|\psi\rangle = \sum_{m=1}^{N} c_m \, e^{i2\pi\delta_m t} e^{-ikz_m} \, |g_1 \dots e_m \dots g_N\rangle \tag{2.1}$$

where z_m is the position of atom m, k is the light field wave number, $\delta_m = n\Delta$ is the atomic detuning from the laser frequency, with n taking integer values, and the state amplitudes c_m depend on both frequency and spatial position of each atom. The collective excitation initially begins to dephase due to variations in atomic frequencies. However, the periodic structure of the comb results in a synchronized rephasing after a predetermined time interval of $t = 1/\Delta$ derived from the condition $e^{i2\pi n\Delta t} = 1$, the excitation will be in phase again which lead to the echo pulse. Therefore, in the original AFC protocol, once the comb shape is created, the storage time of the memory is set. By transferring the collective optical coherence between $|g\rangle$ and $|e\rangle$ to a spin excitation in the ground states employing an optical π pulse resonant with the transition from $|e\rangle$ to an unoccupied state $|s\rangle$ [102, 103], the photons are stored as spin waves between $|g\rangle$ and $|s\rangle$, with the storage duration being limited by the spin coherence lifetime, provided that spin transition is homogeneous. To retrieve the stored excitation, a second π pulse resonant with the $|e\rangle \leftrightarrow |s\rangle$ transition is applied, converting the spin excitation back into an optical one. The total storage time is given by $T_s + 1/\Delta$, where T_s is the time interval between the two π pulses. Consequently, the spin-wave AFC protocol allows for on-demand retrieval with extended storage lifetimes. Storage times ranging from milliseconds to up to an hour have been demonstrated using the AFC protocol [104, 105], by employing long-lived spin states.

The AFC memory achieves high temporal multimode capacity by leveraging the large inhomogeneous broadening of rare-earth ions (REI) in solid-state materials [106, 107]. The multimode capacity (N_{modes}) of an AFC memory is determined by the ratio of the AFC memory bandwidth to the peak spacing, $N_{\text{modes}} \sim \Gamma/\Delta$, which is independent from the optical depth of the medium. Multimode storage in other degrees of freedom, such as spectral and spatial modes, has been demonstrated using the AFC technique [108, 109]. In the case of multiplexing, the requirements on storage time are relaxed due to the increased success probability enabled by simultaneous entanglement generation attempts across multiple modes. The original AFC scheme (two level) can achieve near-noiseless operation, as atomic

decoherence has no effect on the re-emitted photon's state [110, 111]. As a result, it enables extremely high conditional fidelities, with values reported as high as 99.9% [112]. For three-level AFC (spin-wave storage), generally the storage process is not entirely noise-free, with the achieved fidelity depending on the quality of the applied π pulses [113, 103]. Storage fidelities ranging between 75% and 85% for AFC spin-wave memories have been demonstrated [114, 105].

Although AFC quantum memories theoretically have the potential to achieve nearly 100% efficiency with sufficiently large optical depth and optimized comb finesse, practical limitations often arise. These challenges include insufficient atomic absorption and difficulties in creating well-structured spectral combs. Moreover, maintaining both high optical depth and long coherence times simultaneously is particularly demanding, as coherence time generally decreases with increasing doping concentration. Consequently, to achieve longer coherence times, it is often advantageous to work with rare-earth doped crystals of lower optical depth. One promising solution to overcome these limitations is the integration of the memory into an optical cavity, which can significantly enhance light–matter interaction and improve overall efficiency.

Cavity-enhanced AFC quantum memory

Embedding the storage medium within an asymmetric optical cavity enhances the light–matter interaction. When the impedance-matching condition is satisfied, unity efficiency is theoretically achievable with an effective optical depth as low as one. Under these conditions, the memory's efficiency is constrained only by intrinsic atomic dephasing [19, 20] and can approach unity with sufficiently high comb finesse (F), defined as the ratio of the comb spacing to the individual tooth linewidth (FWHM) ($F = \Delta/\gamma$).

For an AFC quantum memory with an effective optical depth $\tilde{d}$ and crystal length L inside a general asymmetric cavity with mirror reflectivities R_1 and R_2 (where $R_1 < R_2 \approx 1$), the reflected amplitude $E_{\text{out}}/E_{\text{in}}$ can be derived by incorporating absorption into the standard

"sum-over-all-roundtrips" method used for Fabry–Pérot cavities [19]:

$$\frac{E_{\text{out}}}{E_{\text{in}}} = \frac{-\sqrt{R_1} + \sqrt{R_2}e^{-\tilde{d}}}{1 - \sqrt{R_1 R_2}e^{-\tilde{d}}} \tag{2.2}$$

Perfect absorption is achieved when the impedance-matching condition $\sqrt{R_1} = \sqrt{R_2}e^{-\tilde{d}}$ is met. This implies that, for a given setup and comb preparation, there exists an optimal optical depth that enables perfect absorption—unlike the no-cavity case, where high optical depth is required to achieve high efficiency.

Several experiments have explored impedance-matched optical cavities to enhance storage efficiency in AFC-based quantum memories [115, 116, 117, 118, 119, 120, 121, 122]. The highest efficiency reported so far is 62% for a 2 μs storage time [120], representing a notable improvement over systems without a cavity. Despite these enhancements, accurately characterizing AFC properties—such as the optical depth (OD)—within an impedance-matched cavity remains experimentally challenging [115, 118]. In contrast to the no-cavity case, Beer's law is no longer directly applicable for extracting OD from transmission spectra.

Moreover, the impedance-matching proposal (equation 2.2) assumes that the quantum memory bandwidth is much narrower than the cavity bandwidth, ensuring resonance condition. Consequently, it does not account for the combs prepared at frequencies detuned from cavity resonance. It also neglects background absorption resulting from imperfect optical pumping used when crafting the comb. The lack of a comprehensive and general theoretical model for cavity-enhanced AFC quantum memories poses a significant challenge for interpreting experimental results. In particular, it hampers direct comparison with theory and complicates the extraction of system parameters from measurements. The first project in this thesis addresses these limitations by developing a theoretical model for cavity-enhanced AFC quantum memories (see chapter 4).

The readout efficiency of a cavity-based AFC quantum memory—the ratio of the re-emitted electric field after the storage time to the input electric field—can be derived via the

same "sum-over-paths" method. This approach generalizes the efficiency formula from [19] by including both the frequency comb and background absorption.

To extend the impedance-matching scheme to off-resonant combs with arbitrary bandwidth, we incorporate the phase accumulated along each photon path in the cavity. We begin with equation (A19) from [18], which gives the efficiency for a cavity-less AFC memory:

$$\frac{E_f(L,t)}{E_f(0,t-\frac{2\pi}{\Delta})} = \int_0^L dz\, e^{-\frac{\tilde{\alpha}z}{2}} \tilde{\alpha} e^{-\frac{\tilde{\alpha}(L-z)}{2}} = \tilde{\alpha} L e^{-\frac{\tilde{\alpha}L}{2}} \tag{2.3}$$

Here, α is the absorption coefficient; $\alpha(\nu)L = d$ is the optical depth due to the AFC; and $\alpha_0 L = d_0$ corresponds to background absorption. Here the first factor under the integral represents the amplitude of photon transmission to the point z, and the second one, $\tilde{\alpha}$ is the amplitude of photon re-emission in the z-direction. The last factor represents the amplitude of the emitted photon transmission from point z to the end of the crystal [18].

Now, to derive the readout efficiency of the cavity memory, we consider the photon's multiple round trips before absorption and after re-emission. The transmission to point z becomes

$$E_c(z) = \frac{\sqrt{T_1} e^{-\frac{\tilde{\alpha}z}{2}} e^{-\frac{\alpha_0 z}{2}} e^{-ikz}}{1 - \sqrt{R_1 R_2} e^{-\tilde{\alpha}L} e^{-\alpha_0 L} e^{-i\Phi}} \tag{2.4}$$

where $T_1 = 1 - R_1$ and the total round-trip phase is $\Phi = 2kL$. The term associated with the amplitude of the transmission of the emitted photon from point z to the end of the crystal in equation (2.3) can be written as

$$E_c(L-z) = \frac{e^{-\frac{(\tilde{\alpha}+\alpha_0)(L-z)}{2}} e^{-ik(L-z)} e^{-\frac{(\tilde{\alpha}+\alpha_0)L}{2}} e^{-ikL} \sqrt{T_1 R_2}}{1 - \sqrt{R_1 R_2} e^{-(\tilde{\alpha}L + \alpha_0 L)} e^{-i\Phi}} \tag{2.5}$$

It is worth noting that the amplitude of photon re-emission in the z-direction, i.e., the $\tilde{\alpha}$ term in equation (2.3), will not be modified since the desirable coherent re-emission of a photon only stems from the atoms in the AFC and not the atoms in the background [101].

The full expression for the cavity-enhanced AFC memory efficiency, derived from equation

(2.3), is

$$2\int_0^L dz\ \frac{\sqrt{T_1}e^{-\frac{\tilde{\alpha}z}{2}}e^{-\frac{\alpha_0 z}{2}}e^{-ikz}\,\tilde{\alpha}e^{-\frac{(\tilde{\alpha}+\alpha_0)(L-z)}{2}}e^{-ik(L-z)}e^{-\frac{(\tilde{\alpha}+\alpha_0)L}{2}}e^{-ikL}\sqrt{T_1R_2}}{\left(1-\sqrt{R_1R_2}e^{-\tilde{\alpha}L}e^{-\alpha_0 L}e^{-i\Phi}\right)\left(1-\sqrt{R_1R_2}e^{-(\tilde{\alpha}L+\alpha_0 L)}e^{-i\Phi}\right)} \tag{2.6}$$

The factor of 2 accounts for absorption during both forward and backward propagation. We also take into account the irreversible atomic dephasing $\sqrt{\eta_F}$ in the Fourier transform of the comb atomic spectral distribution, which stems from the reduction in the peak height after the storage time of the AFC memory with respect to the central peak [18]. Simplifying equation (4) and multiplying by $\sqrt{\eta_F}$ yields the final efficiency expression

$$\sqrt{\eta} = \frac{2\,\tilde{d}\,T_1\sqrt{R_2}\,e^{(\tilde{d}+d_0)}e^{-i\Phi}}{(1-\sqrt{R_1R_2}\,e^{-(\tilde{d}+d_0)}e^{-i\Phi})^2}\sqrt{\eta_F} \tag{2.7}$$

where $\eta_F = e^{-t^2\tilde{\gamma}^2}$, t is the storage time of the quantum memory and $\tilde{\gamma}$ is the comb width. $\tilde{\gamma}$ is related to FWHM peak width γ through $\gamma = \sqrt{8\ln 2}\tilde{\gamma}$. Equation (2.7) generalizes equation 14 in [19] to the off-resonant cavity-enhanced AFC quantum memory with background absorption.

Dispersion effect

To accurately model cavity-enhanced AFC quantum memory, it is essential to include the dispersion effects arising from the engineered atomic absorption used to generate the comb. While prior studies [123, 124] have explored the role of dispersion in AFC—particularly in the context of its connection to slow-light-based storage protocols—there is no theoretical model that incorporates the dispersion caused by absorption engineering within a cavity-enhanced AFC system.

To model light propagation in a dispersive and absorptive medium, it is essential to consider the complex refractive index $\tilde{n}(\nu)$. This complex quantity captures both the phase and attenuation characteristics of the medium. A plane wave traveling through such a

medium acquires both phase and amplitude changes according to the expression

$$E(x) = E_0 \exp(i\tilde{k}x) = E_0 \exp(i\tilde{n}k_0 x) = E_0 \exp(i\mathrm{Re}[\tilde{n}]k_0 x) \exp(-\mathrm{Im}[\tilde{n}]k_0 x), \tag{2.8}$$

where $k_0 = 2\pi/\lambda_0$ is the vacuum wave number and x is the propagation distance. The complex refractive index can be written as $\tilde{n}(\nu) = n(\nu)+ik(\nu)$. The real part of $\tilde{n}(\nu)$, denoted $\mathrm{Re}[\tilde{n}(\nu)] = n(\nu)$, governs the phase velocity of the wave governs and is responsible for the dispersive behavior critical to AFC, while the imaginary part $\mathrm{Im}[\tilde{n}(\nu)] = k(\nu)$, denoted via the absorption coefficient $\alpha(\nu) = 2k_0\mathrm{Im}[\tilde{n}(\nu)]$, leads to the exponential decay in intensity due to absorption. The absorption coefficient $\alpha(\nu)$ enters the Beer–Lambert law, which describes the spatial decay of intensity $I(z)$ in the medium

$$\frac{dI}{dz} = -\alpha I \quad \Rightarrow \quad I(z) = I_0 e^{-\alpha z}, \tag{2.9}$$

highlighting the role of engineered absorption in tailoring the spectral response of quantum memories. The real and imaginary components of the complex refractive index $\tilde{n}(\nu)$ are connected via the Kramers–Kronig relations [125, 126, 127] (see chapter 4 for more details). This formalism is crucial for modeling cavity-enhanced AFC quantum memory where dispersion and absorption are inherently linked through the atomic comb structure. In chapter 4, we show that, by incorporating dispersion, our model demonstrates close agreement with experimental results and, in particular, enables prediction of memory efficiency across arbitrary detunings from the cavity resonance.

2.2.3 Other quantum memory protocols

There are several protocols for implementing quantum memories. A comprehensive review of both experimental and theoretical efforts across different schemes to implement quantum memory can be found in [128, 17, 16, 55]. Here, we briefly describe some of the most popular and widely studied ensemble-based light storage protocols.

Electromagnetically induced transparency-based quantum memory

Electromagnetically induced transparency (EIT), first demonstrated in [129] is a nonlinear optical effect where an initially absorbing medium becomes transparent to a resonant probe laser in the presence of a control field. EIT is observed in a three-level Λ system, in which two long-lived ground states are each coupled to a excited state. The probe field, which carries the quantum information to be stored, is a weak optical signal resonant with one transition and interacts with the medium under the influence of a control field that couples the other ground state to the same excited level. When there is no control field, the probe is absorbed by the medium. However, the presence of the control field opens a narrow transparency window in the absorption spectrum of the medium through quantum interference, leading to the probe transmission through the medium. This is accompanied by steep change in the refractive index (real part of the complex refractive index) which significantly reduces the group velocity of the probe the so-called "slow light" effect. By gradually turning off the control field while the probe is inside the medium, its group velocity is reduced to zero, and the optical excitation is mapped into a collective ground-state spin coherence (spin wave) in the medium. This process involves no real population of the excited state, as the optical excitation is directly mapped onto the spin-wave excitation via adiabatic elimination. To retrieve the stored signal, the control field is turned back on, converting the spin coherence back into an optical field that exits the medium as the original probe pulse. Although storage efficiencies as high as 92% have been demonstrated [130], and storage times on the order of seconds have been achieved using EIT-based schemes [131], their inherently limited multimode capacity reduces their appeal for applications in quantum networks [98].

Off-resonant Raman-based quantum memory

The Raman memory protocol [132] employs a three-level Λ system, where a weak probe signal field and a strong control field interact with the atoms. Both fields are equally detuned far from the excited state, leading to an off-resonant quantum memory while EIT-based scheme

relies on resonant interactions (see figure 2.2). In the absence of the control field, the probe signal passes through the medium. However, when the control field is present, the probe can be virtually absorbed resulting in a population transfer between the two ground states via stimulated Raman scattering. This transfer generates a collective spin-wave coherence within the ensemble. Switching off the control field effectively stores the excitation in the medium, and reactivating it later retrieves the stored information by converting the spin-wave back into a photonic signal. Raman-based quantum memory has been experimentally demonstrated [133, 134, 135], with bandwidths above 1 GHz [134].

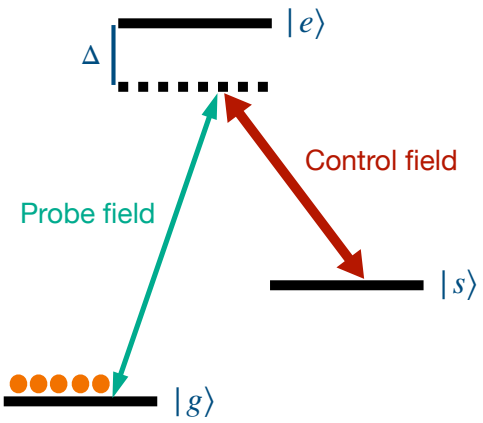

Figure 2.2: A three-level (Λ) system is driven by a control field and a probe field, both detuned by Δ from the excited state.

Controlled reversible inhomogeneous broadening quantum memory

The controlled reversible inhomogeneous broadening (CRIB) scheme, along with the gradient-echo memory (GEM) (see next discussed scheme) and the previously mentioned AFC protocol, are are all part of the broader category of photon-echo-based quantum memories. Similar to EIT and Raman-based approaches, these protocols are based on mapping the coherence of an optical signal onto a collective atomic excitation. However, photon-echo-based memories specifically exploit the inhomogeneous broadening found in the absorption spectra of certain media, such as rare-earth-ion-doped crystals (see chapter 3 for more details). In the photon-echo-based schemes, an incoming optical pulse is absorbed by an ensemble of atoms

with slightly different transition frequencies that causes the atoms to accumulate different phases over time, leading to dephasing of the collective excitation. A controlled time-reversal of the dephasing process is then employed to rephase the atomic ensemble, resulting in the re-emission of the original signal, referred to as the echo pulse. Consider an ensemble of two-level atoms with ground and excited states denoted by $|g\rangle$ and $|e\rangle$, respectively. Initially, all atoms are prepared in the ground state, forming a product state $|g_1, g_2, ..., g_N\rangle$. When a photon enters the medium, its excitation is collectively absorbed, forming a collective state that is a coherent superposition state across the ensemble, as described in equation (2.1). Due to the inhomogeneous broadening, each atom's transition frequency is detuned from the signal frequency by an amount δ_m resulting in collective state dephasing. Various photon-echo-based memory schemes implement different rephasing techniques to reverse this dephasing and enable retrieval of the optical signal. The CRIB, GEM, and AFC protocols differ in both the prepared structure of the inhomogeneous broadening and the method applied to achieve rephasing. In CRIB quantum memory [136, 137, 138] an initially narrow absorption line of a medium such as a rare-earth-ion-doped crystal is broadened by applying an inhomogeneous external electric or magnetic field, designing a controlled absorption profile. The broadened ensemble can absorb an incoming optical pulse with a bandwidth larger than the initial linewidth but narrower than the final broadening. Due to the inhomogeneous detunings introduced by the external field, the atomic ensemble dephases after absorption. To recover the signal, the external field is reversed (external field with opposite polarity) at time $t = T$, which inverts the detuning of each atom to $-\delta_m$, and effectively time-reverses the dephasing process (there will be a factor of $e^{-i2\pi\delta_m t}$ in equation (2.1)). As a result, all atoms rephase at time $t = 2T$, leading to the collective re-emission of the echo pulse. Similar to AFC protocol, control pulses can be applied to transfer the collective coherence to a long-lived hyperfine ground-state. This protocol has been experimentally demonstrated in solid-state media and shows promise for efficient, on-demand quantum memory applications [139].

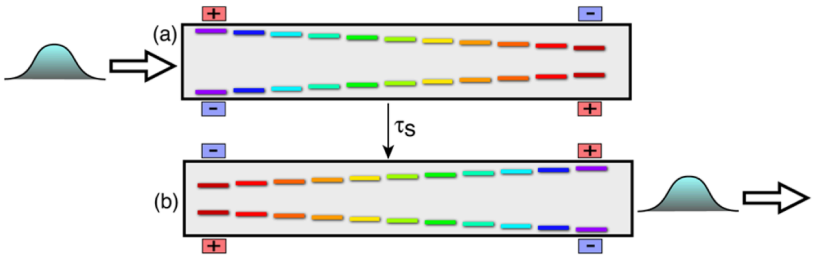

Figure 2.3: The figure illustrates the gradient-echo-based quantum memory protocol. **(a)** A linear electric field is applied along the length of the storage medium, inducing a position-dependent Stark shift such that different locations correspond to different resonant frequencies. The storage pulse then enters the medium. **(b)** After reversing the polarity of the electric field, the stored light is re-emitted as a forward-propagating echo. Figure from Ref. [140]. Reprinted with permission from Phys. Rev. Lett. 101, 203601 (2008). Permission to include the figure can be found in appendix A.

Gradient-echo quantum memory

The gradient echo memory (GEM) protocol, also known as longitudinal CRIB (LCRIB), is a photon-echo-based quantum memory technique that evolved from the CRIB protocol. One of the primary challenges in early CRIB implementations was the need for backward retrieval to mitigate re-absorption of the re-emitted signal and improve the efficiency. However, it was later shown [141, 142] applying a spatially varying external electric field along the direction of light propagation (longitudinally) causes position-dependent frequency shifts across the medium and can suppress re-absorption, enabling efficient forward retrieval (see figure 2.3). The longitudinal broadening in GEM ensures that different regions of the medium absorb and re-emit at distinct frequencies avoiding re-absorption of the echo in forward direction. Some of the most significant experimental results in ensemble-based quantum memories have been achieved using the GEM protocol [143, 144, 145, 64], including 87% recall efficiency in a warm rubidium vapour [64].

Autler-Townes effect-based quantum memory

In spectroscopy, the Autler–Townes effect (also known as the AC Stark effect) describes the splitting of an atomic absorption line when a strong, resonant electromagnetic field

couples two quantum states. This phenomenon forms the foundation for a light storage protocol known as the Autler–Townes splitting (ATS)-based quantum memory protocol [146, 147, 148]. Consider a three-level Λ system configuration where a weak, resonant probe field interacts with the $|g\rangle - |e\rangle$ transition, while a strong control field drives the $|s\rangle - |e\rangle$ transition. When the Rabi frequency of the control field (Ω_C) exceeds the spontaneous decay rate (Γ_{ge}), the probe absorption spectrum splits into two peaks separated by Ω_C, enabling the coherent storage of the probe field. As the Autler–Townes splitting is directly linked to the strength of the control field, the memory bandwidth is dynamically tunable, making the ATS protocol inherently suitable for broadband quantum storage [147]. Depending on the temporal configuration of the control field, realization of on-demand operation is possible in ATS scheme [147]. By switching off the control field just before the first recall begins, the storage is initiated by effectively freezing the optical excitation as a long-lived spin coherence. Assuming negligible spin decoherence, the spin excitation is preserved during the storage period. By reapplying the control field, retrieval process is triggered which maps the spin-excitation back onto optical excitation, leading to re-emission of the stored light into the output photonic mode. ATS quantum memories have experimentally achieved a bandwidth of 15 MHz [147], and storage efficiencies as high as 30% have been reported [149]. In addition, theoretical study on implementing cavity-enhanced ATS memories with T centers has shown promising potential [150].

2.3 Quantum Gates

Quantum gates are foundational for manipulating qubits in a quantum computer. Analogous to classical logic gates, quantum gates operate on qubits through unitary transformations, which preserve the norm of the quantum state. Mathematically, a quantum gate acting on n qubits is represented by a $2^n \times 2^n$ unitary matrix ($\hat{U}$)

$$\hat{U}\hat{U}^\dagger = \hat{U}^\dagger\hat{U} = I,$$

where $\hat{U}^\dagger$ is the conjugate transpose of $\hat{U}$, and I is the identity matrix. Principles of quantum mechanics, in particular superposition and entanglement allows quantum gates to perform computations that have no direct classical analogs. These gates can not only perform bit flips but also introduce phase flips, create entangled states, and rotate states of qubits on the Bloch sphere.

2.3.1 Single-qubit gates

Single-qubit gates act on individual qubits and are represented by 2×2 unitary matrices. Their operation corresponds to the rotations of the Bloch vector (qubit state) on the Bloch sphere. Among the most fundamental single-qubit gates are the Pauli gates and the Hadamard gate.

Pauli Gates

The Pauli gates: $\hat{X}$, $\hat{Y}$, and $\hat{Z}$, are a set of basic operations that perform qubit state rotations by π around the $\hat{x}$, $\hat{y}$, and $\hat{z}$ axes of the Bloch sphere.

Pauli-X (Bit-flip) Gate:

$$\hat{X} = \begin{pmatrix} 0 & 1 \\ 1 & 0 \end{pmatrix}$$

In vector notation, the qubit states $|0\rangle$ and $|1\rangle$ are denoted as $|0\rangle = \begin{pmatrix} 1 \\ 0 \end{pmatrix}$, and $|1\rangle = \begin{pmatrix} 0 \\ 1 \end{pmatrix}$. Pauli-X gate swaps the computational basis states as $\hat{X}|0\rangle = |1\rangle, \quad \hat{X}|1\rangle = |0\rangle$, similar to a classical NOT gate.

Pauli-Z (Phase-flip) Gate:

$$\hat{Z} = \begin{pmatrix} 1 & 0 \\ 0 & -1 \end{pmatrix}$$

This gate leaves $|0\rangle$ unchanged and flips the sign of $|1\rangle$ ($\hat{Z}|0\rangle = |0\rangle, \quad \hat{Z}|1\rangle = -|1\rangle$).

Pauli-Y (Bit and Phase Flip) Gate:

$$\hat{Y} = \begin{pmatrix} 0 & -i \\ i & 0 \end{pmatrix}$$

The $\hat{Y}$ gate combines the effects of $\hat{X}$ and $\hat{Z}$ All Pauli gates are both unitary and Hermitian (they are equal to their own conjugate transposes).

Rotation Gates

More general single-qubit operations can be achieved by rotation gates, which are defined as exponentials of the Pauli matrices:

$$R_X(\theta) = e^{-i\theta\hat{X}/2}, \quad R_Y(\theta) = e^{-i\theta\hat{Y}/2}, \quad R_Z(\theta) = e^{-i\theta\hat{Z}/2}$$

These gates correspond to continuous rotations around the relevant axes of the Bloch sphere. Any arbitrary 2×2 unitary matrix can be expressed into a product of these rotations as

$$\hat{U} = e^{i\delta} R_X(\theta_1) R_Z(\theta_2) R_X(\theta_3),$$

where δ is a global phase and $\theta_1, \theta_2, \theta_3$ are rotation angles. The above expression shows that any single-qubit state can be transformed into any other state through unitary matrix U using a sequence of such gates, confirming their universality for single-qubit operations.

Hadamard Gate

The Hadamard gate ($\hat{H}$) is one of the most used quantum gates in quantum computing due to its ability to create superposition states. Its matrix form is

$$\hat{H} = \frac{1}{\sqrt{2}} \begin{pmatrix} 1 & 1 \\ 1 & -1 \end{pmatrix}$$

which maps the computational basis states as follows

$$\hat{H}|0\rangle = \frac{1}{\sqrt{2}}(|0\rangle + |1\rangle), \quad \hat{H}|1\rangle = \frac{1}{\sqrt{2}}(|0\rangle - |1\rangle)$$

The Hadamard gate performs a π rotation around the axis $(\hat{x} + \hat{z})/\sqrt{2}$ on the Bloch sphere, moving the qubit state from the poles to the equator.

2.3.2 Two-qubit gates

Two-qubit gates are the quantum analogues of two-bit logic gates in classical computation. They are crucial for generating entanglement which is a fundamental resource for quantum information processing, and for enabling universal quantum computation by creating non-classical correlations between qubits.

Controlled-NOT (CNOT) Gate

The controlled-NOT (CNOT) gate, also known as the controlled-X gate, performs a NOT operation on the target qubit conditioned on the control qubit being in the state $|1\rangle$. Its matrix representation is

$$\text{CNOT} = \begin{bmatrix} 1 & 0 & 0 & 0 \\ 0 & 1 & 0 & 0 \\ 0 & 0 & 0 & 1 \\ 0 & 0 & 1 & 0 \end{bmatrix}$$

If it is applied to a product state, the CNOT gate can produce an entangled state. For example

$$\text{CNOT}\left[\left(\alpha\left|0\right\rangle+\beta\left|1\right\rangle\right)\otimes\left(\gamma\left|0\right\rangle+\delta\left|1\right\rangle\right)\right]$$

results in a two-qubit state that cannot be expressed as the tensor product of individual qubit states.

Controlled-Z (CZ) Gate

The controlled-Z (CZ) gate is a two-qubit gate that applies a Z operation, i.e., a phase flip to the target qubit if the control qubit is in state $|1\rangle$. It can be represented as

$$\text{CZ}=\begin{bmatrix}1&0&0&0\\0&1&0&0\\0&0&1&0\\0&0&0&-1\end{bmatrix}$$

which leaves the basis states $|00\rangle$, $|01\rangle$, and $|10\rangle$ unchanged, but maps $|11\rangle$ to $-|11\rangle$. Similar to the CNOT gate, CZ can also generate entanglement. These two gates are related via the Hadamard transformation

$$\text{CZ}=(I\otimes\hat{H})\ \text{CNOT}\ (I\otimes\hat{H})$$

that shows how changing the basis of the target qubit with a Hadamard gate transforms between the CZ and CNOT operations.

Controlled-Phase (CPhase) Gate

The controlled-Phase (CPhase) gate generalizes the CZ gate by applying an arbitrary phase shift ϕ to the $|11\rangle$ state

$$\text{CPhase}(\phi) = \begin{bmatrix} 1 & 0 & 0 & 0 \\ 0 & 1 & 0 & 0 \\ 0 & 0 & 1 & 0 \\ 0 & 0 & 0 & e^{i\phi} \end{bmatrix}$$

When $\phi = \pi$, the CPhase gate becomes equivalent to the CZ gate. These two-qubit gates (CNOT, CZ, and CPhase) form the foundation for creating entanglement and implementing quantum operations on multi-qubits. They can form a universal set of gates if combined with a sufficient set of single-qubit gates.

2.4 Applications

In this section, I discuss some of the main applications of future global quantum networks.

2.4.1 Secure communications

One of the most important applications of quantum networks is the ability for quantum-secure communication through quantum key distribution (QKD) over long distances [151]. Among various quantum technologies, QKD is one of the most mature, both theoretically and experimentally [7]. In classical communication a secret key exchanged between two distant parties can be intercepted and copied without detection, however, QKD leverages fundamental quantum principles to detect any eavesdropping attempts. The most well-known QKD scheme is the BB84 protocol, introduced by Bennett and Brassard in 1984 [6]. It uses single photons prepared in one of the four polarization states—vertical, horizontal, 45°, or 135°—which correspond to two mutually unbiased (conjugate) polarization bases, to encode key bits. Alice randomly prepares and sends these photons to Bob, and he measures

them in a randomly chosen basis. After the transmission, Alice and Bob communicate over an authenticated classical channel to announce their choice of basis and keep only the measurements made in matching bases, resulting in the sifted key.

Due to the no-cloning theorem and the non-commutativity of measurements in conjugate bases, an eavesdropper (Eve) cannot gain information about the key without introducing disturbances (errors). In a common eavesdropping strategy, Eve can guess about the basis of each qubit, and make a measurement based on that which is called the intercept-and-resend attack. Therefore, the probability that Alice and Bob can detect Eve is 1/4 for one qubit when Alice and Bob use the same basis. By increasing the number of qubits in the transmitted key (n), this probability is $1 - (3/4)^n$ which gets close to 1 for large n values [152]. There are various protocols to realize QKD, such as the one proposed by Ekert in 1991 the 'E91 protocol', which employs quantum entanglement for cryptographic applications [153]. Numerous experimental demonstrations of quantum key distribution (QKD) over long distances have been reported, including [154, 155, 156, 157, 158]. To extend QKD beyond the limits of direct transmission, quantum repeaters are essential for mitigating photon loss in optical fibers during key distribution. Alternatively, satellite-based QKD has enabled secure key exchange over distances exceeding 7000 km [156]. Although practical device imperfections continue to pose challenges, QKD offers information-theoretic security that is fundamentally unattainable with classical approaches, establishing it as a cornerstone of secure communication in future quantum networks.

2.4.2 Distributed quantum computing

Although, the advancements in quantum computing can revolutionize various fields, current and near-future quantum processors operate in the NISQ era of noisy intermediate-scale quantum devices with up to a few hundred qubits that are susceptible to errors and lack full fault tolerance [159]. Scaling these systems to support large-scale, error-corrected quantum computations is a big challenge [160, 161, 162]. Distributed Quantum Computing (DQC) is

a promising approach to overcome such limitations by connecting multiple smaller quantum processors containing a relatively small number of qubits through classical and quantum communication channels [163, 164, 165, 166]. This approach transforms the scaling problem into the task of building modular units and establishing reliable connections between them [8].

The ability to perform entangling operations such as CNOT gates, between qubits located in different modules is a critical requisite for DQC. As direct transmission of quantum information between modules is prone to loss, DQC often relies on quantum teleportation as a key protocol for transferring information (quantum states) between qubits located in different modules (see section 1.5). Broadening this concept, quantum gate teleportation (QGT) allows for the implementation of non-local quantum gates between distant qubits employing an entangled Bell pair and classical communication [167].Assuming each node can perform arbitrary single-qubit and two-qubit gates locally, QGT scheme provides the remaining ingredient to realize a universal set of quantum gates for distributed quantum computing [168]. The communication distance between modules can be extended by utilizing quantum repeaters, leading to reliable teleportation operations over long distances (see section 2.1). There have been various experimental demonstrations of DQC [169, 170, 171] including the one where distributed quantum computing between two photonically connected modules separated by two meters was experimentally realized, a controlled-Z (CZ) gate was teleported between the modules, and a distributed version of Grover's search algorithm spanning both modules was executed successfully [172]. Recently, DQC protocols have been demonstrated in T centers, highlighting their potential as a platform for distributed quantum computing [93].

2.4.3 Quantum internet

Quantum internet that consists of a network of connected quantum processors and communication nodes globally is the ultimate goal of quantum information processing [10, 173, 174].

Such a network can transform various quantum technologies from QKD to DQC by allowing users around the world to access quantum resources remotely and securely [174]. Eventually, it could outperform even the most advanced monolithic quantum computers by enabling distributed processing across multiple nodes.

One of the key challenges in realizing a practical quantum internet is finding a reliable way to transmit quantum information over long distances. Quantum repeaters play an important role by distributing entanglement across long-distance quantum links [13]. The generated entanglement serves as a resource for performing various tasks. Different strategies may be required for realizing the global quantum network, depending on the distance between nodes. For beyond a few hundred kilometers, direct fiber transmission essentially loose its viability. For distances less than $2,000\,\text{km}$, fiber-optic quantum repeaters may be an ideal option [1]. Satellite-based quantum communication using low-Earth-orbit (LEO) satellite links offers an optimal choice for intercontinental connections (a few thousand kilometers). There have been various experimental demonstrations by the Micius satellite including satellite-to-ground QKD [175], entangled photon pairs distribution over 1200 kilometers [176], and ground-to-satellite quantum teleportation [177]. Experimental demonstrations of QKD over even longer distances have also been achieved (see section 2.4.1). For the greatest distances, deploying geostationary satellites that remain fixed relative to the Earth's surface, thereby ensuring continuous connectivity could be an option, although this requires more expensive, specially designed satellites that can withstand the increased radiation at those altitudes [178]. As a result, quantum repeaters employing LEO satellite links was proposed to enable broader coverage [178]. Moreover, incorporating quantum memories on satellites could mitigate channel loss and synchronize entanglement distribution [179].

Thanks to significant research advancements across the various building blocks, the realization of a scalable quantum internet is becoming an attainable goal.

Chapter 3

Physical platforms

In this chapter, I will discuss a range of physical platforms employed for the implementation of quantum network elements, with a focus on those utilized in the projects presented in this thesis [180, 181].

3.1 Rare-earth ion doped crystals

Rare-earth-ion-doped crystals (REICs), initially explored for their spectroscopic properties and potential in laser physics, are among the most attractive platforms for implementing quantum information processing technologies because they offer a controlled environment with relatively isolated ensembles of a single atomic species. In particular, their resilient to environmental effects make them ideal for quantum storage. Rare-earth elements are atoms from the sixth row of the periodic table, including scandium, yttrium and fifteen metallic elements known as the lanthanides. Their 4f–4f optical transitions remain largely isolated from the crystal host environment, leading to narrow homogeneous linewidths and long coherence times. This is caused by the partial shielding of the 4f shell electrons by the filled 5s, 5p, and 6s shells that possess larger radial distributions [182]. In REICs, rare-earth trivalent ions—formed by the loss of three outer electrons (the 5d and two 6s electrons)—typically occupy host lattice sites by substituting host cations. (The electron

configuration of these ions in their trivalent state is [Xe] $4f^n$, where n ranges from 0 to 14, depending on the ion. The most studied rare-earth ions include Eu^{3+}, Er^{3+}, Pr^{3+}, Nd^{3+}, Yb^{3+}, and Tm^{3+}.

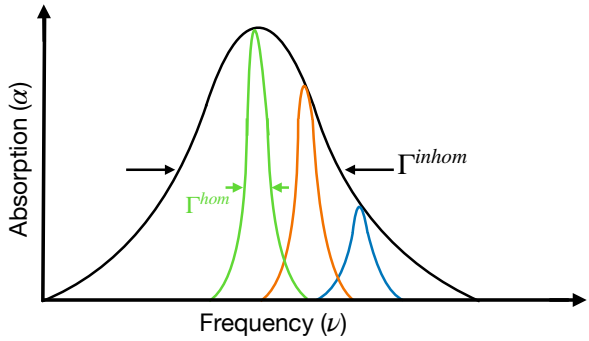

Figure 3.1: The figure shows homogeneous vs inhomogeneous broadening in the optical transition of Rare-earth-ion-doped crystals (REICs).

The optical transitions of REICs features a combination of homogeneous and inhomogeneous broadening as shown in figure 3.1. Homogeneous broadening arises from dynamic processes that perturb the ion's transition frequency or phase and typically affects all ions in the crystal lattice equally. It is fundamentally limited by the excited-state lifetime T_1, such that $\Gamma^{\text{hom}} \geq 1/(2\pi T_1)$, and is directly related to the coherence time T_2 (includes both population decay and dephasing effects) through $\Gamma^{\text{hom}} = 1/(\pi T_2)$. In practice, T_2 is often much shorter than $2T_1$ due to dephasing processes caused by interactions with the host lattice and other dopant ions, implying that $T_2 \leq 2T_1$. At cryogenic temperatures (below 10 K), homogeneous linewidths become extremely narrow—typically ranging from less than 1 kHz to 1 MHz. At these low temperatures, shielding by the $5s$ and $5p$ electrons results in the dominant limitation to the homogeneous linewidth arising from magnetic interactions with nearby rare-earth dopants or magnetically active constituents in the host lattice. Therefore, to minimize these effects and achieve long coherence times, crystal hosts with low concentrations of nuclear spins and rare-earth dopants are desirable [183]. One of the narrowest homogeneous linewidths reported at 50 Hz, has been observed for erbium ions doped into yttrium orthosilicate (YSO) crystals [184], limited by an excited-state lifetime of around

10 ms.

Doped into crystal hosts, rare-earth ions experience static variations in their local environments, such as strain, electric and magnetic fields, and disorder from the crystal growth process, which cause each ion to experience a slightly different local field. As a result, the resonant frequencies of these ions exhibit small Stark and Zeeman shifts, leading to inhomogeneous broadening, Γ^{inh}, in the absorption spectra. The inhomogeneous broadening can vary greatly depending on the crystal host. Typically, inhomogeneous broadening span from several hundred megahertz up to tens of gigahertz [185]. However, there have also been reports of more extreme cases, with linewidths as narrow as 10 MHz [186] and as broad as 250 GHz [184]. For the quantum memory applications, a large inhomogeneous broadening is desirable, as it enables a broad working bandwidth that can be precisely engineered using spectral hole burning techniques, while a narrow homogeneous broadening is preferred because it results in longer optical coherence times. REICs are often implemented as ensemble-based quantum memories, particularly in photon-echo-based protocols, offering extended coherence lifetimes, broad bandwidths, and high multimode capacity (see chapter 4.1). In protocols such as AFC, a larger inhomogeneous broadening enhances the multimode capacity, since the number of achievable peaks depends on the medium's homogeneous and inhomogeneous linewidths without requiring an increase in the sample's atomic density. These unique electronic and spectroscopic properties make REICs versatile platforms for solid-state quantum memories in future quantum networks.

3.1.1 Thulium-doped Yttrium Aluminum Garnet (Tm:YAG) crystal

Thulium-doped $Y_3Al_5O_{12}$ (Tm:YAG) with Tm^{3+} ions substituting Y^{3+} sites in the YAG lattice is a rare-earth-ion-doped crystal that has emerged as an attractive platform for quantum memory and communication applications. The optical transition of Tm^{3+} in YAG at around 793 nm (between the $^3H_6$ ground manifold and the $^3H_4$ excited manifold) can be con-

veniently addressed using commercially available diode lasers, making it a popular choice in quantum technology [185]. Its near-infrared wavelength can also be efficiently converted to the telecommunication C-band which makes Tm:YAG compatible with existing fiber-optic networks. Besides, the only stable isotope of thulium, ^{169}Tm, has a nuclear spin of $I = 1/2$, resulting in a simple hyperfine structure that has no hyperfine splitting in the crystal field levels at zero magnetic field. When an external magnetic field is applied, both the ground and excited states associated with the 793 nm transition are split into a pair of spin states. Applying a small splitting between spin states leads to a low probability of spin-flip transitions, which facilitates optical pumping and creates high-resolution spectral features in the system. As a result, it enables the implementation of Λ-type optical memories under an applied magnetic field [185, 119]. The lack of additional hyperfine levels precludes memory protocols relying on population transfer to the spin states, making thulium ions a suitable candidate only for two-level AFC memories with predetermined storage time.

Tm:YAG features a large inhomogeneous broadening of approximately 20 GHz and a narrow homogeneous linewidth of around 10 kHz [182] at cryogenic temperatures (around 1.5–4 K) thanks to weak electron-phonon coupling. The relatively long optical excited-state lifetime of approximately $T_1 = 800\,\mu$s, combined with a coherence time of at least $T_2 = 30\,\mu$s [182, 187], provides ample time for optical storage and retrieval. There have been various experimental quantum memory demonstrations using Tm:YAG crystals, including [119, 187]. The combination of broad inhomogeneous linewidth, long optical coherence times, and a simple hyperfine structure makes Tm:YAG a promising choice for implementing broadband, multimode, and long-lived quantum memories for quantum networks.

3.2 Defect centers in silicon

Silicon-based photonic platforms benefit from decades of technological maturity which includes best-in-class integrated single-photon detectors, a broad range of quantum optics tools,

and compatibility with the worldwide integrated photonics industry, widely used in data-center interconnects, telecommunication networks, biosensing, Light detection and ranging (LiDAR), and emerging quantum photonic technologies, all making silicon an attractive platform for scalable quantum information processing. While hybrid integration with other architectures has enabled interfacing of photon–spin systems with silicon photonics, silicon host itself offers remarkably long spin coherence times, especially in isotopically purified ^{28}Si. The discovery of individually addressable photon–spin centers in silicon could remove the need to advance photonics infrastructure in less mature material platforms.

Among the defects that emit in the telecommunication bands, radiation damage centers such as the G, C, and W centers are prominent due to their bright luminescence and narrow zero-phonon linewidths. These centers are formed by irradiating silicon with high-energy particles (e.g., electrons, neutrons), displacing atoms and creating vacancies. Mobile interstitial silicon atoms may subsequently swap with substitutional impurities such as carbon, forming various defect centers. Annealing after the irradiation procedure increases atomic mobility in the lattice, thereby affecting the formation probability of specific centers [188]. The G center, for example, has earned considerable attention due to its emission at 1280 nm [189] and demonstrations of its integration with silicon photonic structures. The W and C centers emit at 1217 nm [190] and 1571 nm [191], respectively.

Ensembles of these centers in isotopically purified ^{28}Si have exhibited narrow optical linewidths (up to two orders of magnitude narrower than in natural silicon). Despite their optical strengths and ease of fabrication, the G and W centers have been found to lack unpaired electron spins, limiting their suitability for use as spin qubits. However, the C center has a spin-dependent excited state, which may be used for optical readout of nearby ^{13}C nuclear spin qubits, although this remains an open research direction [191, 188]. These limitations have motivated the exploration of other defects, such as the T, M, and I centers, which are predicted to host unpaired electron spins [192]. Among these, the T center has recently emerged as a particularly attractive candidate for integration into silicon photonics,

as discussed in more detail below.

3.2.1 T center in silicon

T centers in silicon have recently emerged as a promising platform for quantum technologies. It combines long electron and nuclear spin coherence times with spin-selective bound exciton excited state optical transitions in the telecommunication O-band well aligned with existing fiber-optic infrastructure. They can be integrated into CMOS-compatible silicon-on-insulator (SOI) photonic chips making them particularly attractive for scalable quantum networks and distributed quantum computing, offering both technical and commercial advantages [193]. Isotopically purified silicon (^{28}Si) enhances the spin-photon interface by eliminating ^{29}Si nuclear spins, which improves spin coherence and reduces the inhomogeneous broadening of optical transitions [91].

The T center is composed of two carbon atoms (directly bonded) and a hydrogen atom (bounded to one carbon) substituting for a silicon atom in the lattice, leaving an unpaired electron in a dangling bond which is essential for applications in quantum technology [194, 91] (see figure 5.1). The excited state of the T center is formed through a defect-bound exciton, where a hole binds to the localized defect state occupied by the electron, leading to spin-selective optical transitions. Due to the defect's reduced symmetry, the hole states split into two spin doublets called TX_0 and TX_1. When a static magnetic field is applied, the TX_0 zero-phonon line splits into hole spins $|\downarrow_h\rangle$ and $|\uparrow_h\rangle$ (four spin-dependent transitions). Due to the anisotropy of the unpaired hole spin in the excited state, twelve distinct orientational subsets can be individually addressed, each with its own g_H (hole g factor) determining the energy level splittings. Each T center is associated with one of these subsets, resulting in up to forty-eight observable optical transitions [91, 195] (see figure 5.1). T centers can be formed in silicon grown by various methods, with state-of-the-art fabrication relying on ion implantation of carbon and hydrogen followed by a heat treatment between 350°C and 600°C. The annealing step activates the defects, while excess hydrogen in the silicon can

passivate them, effectively deactivating their optical emission [91, 196].

Although T centers in silicon have been known for several decades [194, 192, 197, 198, 199, 200], their potential as a spin-photon interface for quantum technologies was recently explored [91]. That study focused on ensembles of T centers in isotopically purified ^{28}Si and measured key properties, including long electron and nuclear spin coherence times of 2.1 ms and 1.1 s, respectively, as well as spin-selective optical emission from the TX_0 transition at 1326 nm, with a lifetime of approximately 940 ns. The Debye-Waller factor, which quantifies the fraction of emission into the zero-phonon line, was measured to be 0.23 [91]. Although the exact value of the radiative efficiency η_r remains uncertain, Ref. [92] established a lower bound of $\eta_r \geq 0.23$ for an individual T center, indicating that at least this fraction of emission proceeds via radiative decay. T centers have also been fabricated and investigated in commercial materials beyond bulk silicon, including the 220 nm device layer of silicon-on-insulator wafers and integrated silicon photonic waveguides [196, 195, 201] (see chapter 5 for more details). To boost fluorescence emission, Purcell enhancement of individual T centers in low-loss silicon photonic crystal cavities has been demonstrated [93, 92, 202]. Recent experimental progress further highlights the promise of T centers in advancing quantum network. Ensembles of T centers have been studied as potential quantum memories and transducers by investigating their spin properties, measuring optical depths, and analyzing achievable efficiencies [150]. Moreover, Ref. [93] reported the generation of entanglement between the electron spins of two individual T centers using the Barrett-Kok photon interference protocol, demonstrating their potential as distributed quantum network nodes. At the single T center level, a local CNOT gate was implemented by exploiting the electron and nuclear spins as control and target qubits, respectively, using Rabi oscillations on the relevant microwave transition.

3.3 Other physical platforms

3.3.1 Atomic Gases

One of the most commonly used platforms for quantum memory applications is ensembles of neutral atoms in the gaseous phase, typically composed of atoms such as rubidium (Rb), cesium (Cs), strontium (Sr), and ytterbium (Yb). Atomic gases are broadly categorized into hot vapors and cold atoms. Cold atoms are laser-cooled to sub-kelvin temperatures and are confined in optical traps or lattices, where their low thermal motion allows precise control of quantum states and interactions. In contrast, hot atomic vapors consist of room-temperature ensembles of the same neutral atoms that are confined in glass vapor cells. Various ensemble-based quantum memory protocols such as EIT [130], ATS [147, 148], off-resonant Raman-based schemes, and GEM [145, 203] have been experimentally demonstrated in these systems with a maximum achieved storage efficiency of up to 92% using the EIT protocol [130], and a record storage time of 16 s in cold atoms [204]. Although hot atomic vapors are of interest for practical applications due to their potential for room-temperature operation, the observed quantum storage lifetimes remain significantly shorter than those achieved with cold atoms [55]. In addition, noise arising from spontaneous four-wave mixing processes poses a significant challenge for hot vapor memories, which can generate spurious photons and degrading the fidelity, particularly in EIT and Raman-based implementations [205, 17].

3.3.2 Color centers in diamond

Both nitrogen-vacancy (NV) centers and silicon-vacancy (SiV) centers are color centers in diamond that have attracted significant interest. An NV center is formed when a nitrogen atom substitutes for a carbon atom in the lattice, adjacent to a missing carbon atom (a vacancy). On the other hand, the SiV center forms when two neighboring carbon atoms are replaced by a single silicon atom, occupying a position between the two vacant sites [16].

Coupling to nearby nuclear spins with long coherence times provides a robust approach for long time quantum state storage. In both NV and SiV centers, nuclear spins such as ^{13}C nuclei located near a ^{14}N impurity in NV centers [206], and ^{29}Si [207] or nearby ^{13}C nuclei [208] in SiV centers, have exhibited coherence times on the order of several seconds.

Two photon interference-based entanglement generation, in particular the Barrett–Kok scheme [209], has been demonstrated between NV centers [79, 81], and heralded entanglement between two quantum network nodes separated by 10 km and connected via 25 km of deployed optical fiber has been realized [51]. In addition, multi-node networks with NV centers have been demonstrated [210]. Also, Ref. [52, 211] demonstrated heralded entanglement between two independently operated SiV nodes separated by 6 m, employing a 40 km low-loss fiber spool loop and a 35 km deployed fiber link in an urban environment. These experiments highlight the potential of SiV and NV centers for long-distance quantum networks.

Chapter 4

Towards a realistic model for cavity-enhanced atomic frequency comb quantum memories

4.1 Preface

Cavity-enhanced atomic frequency comb (AFC) quantum memory is promising for long-distance quantum communication. Here, we develop a theoretical model for cavity-enhanced AFC quantum memory that accounts for dispersion effects, and we demonstrate that the model closely matches our experimental results.

This work was carried out in collaboration with a few co-authors. My primary contributions to to this work include developing the theoretical model, performing data analysis on the experimental results, and carrying out numerical calculations and coding. I also wrote the initial draft of the manuscript and subsequently implemented revisions based on feedback from the other co-authors.

Towards a Realistic Model for Cavity-Enhanced Atomic Frequency Comb Quantum Memories

Quantum Sci. Technol. 9, 035049 (2024)

Shahrzad Taherizadegan[1], Jacob H. Davidson[2], Sourabh Kumar[1], Daniel Oblak[1], and Christoph Simon[1]

[1]*Department of Physics & Astronomy, Institute for Quantum Science and Technology, University of Calgary, 2500 University Drive NW, Calgary, Alberta T2N 1N4, Canada*

[2]*QuTech and Kavli Institute of Nanoscience, Delft University of Technology, 2600 GA Delft, The Netherlands*

Abstract

Atomic frequency comb (AFC) quantum memory is a favorable protocol in long distance quantum communication. Putting the AFC inside an asymmetric optical cavity enhances the storage efficiency but makes the measurement of the comb properties challenging. We develop a theoretical model for cavity-enhanced AFC quantum memory that includes the effects of dispersion, and show a close alignment of the model with our own experimental results. Providing semi-quantitative agreement for estimating the efficiency and a good description of how the efficiency changes as a function of detuning, it also captures certain qualitative features of the experimental reflectivity. For comparison, we show that a theoretical model

without dispersion fails dramatically to predict the correct efficiencies. Our model is a step forward to accurately estimating the created comb properties, such as the optical depth inside the cavity, and so being able to make precise predictions of the performance of the prepared cavity-enhanced AFC quantum memory.

4.2 Introduction

Optical quantum memory with the ability to store and recall on-demand quantum states of light with high efficiency and fidelity [212, 213, 214] is one of the essential elements for long-distance quantum communication based on quantum repeaters [14, 24]. It also has several applications in linear-optical quantum computation, single-photon detection, quantum metrology, and tests of the foundations of quantum physics [215].

AFC quantum memory [18, 101] is a promising candidate in quantum repeater applications because of the capability to simultaneously store and read out multiple temporal and spectral modes that could enhance the performance of the quantum repeater via faster entanglement generation [97, 216, 48, 217, 218, 219, 109]. Also, as opposed to other quantum memory protocols, with the AFC technique, the number of temporal modes stored in a sample is independent of the optical depth of the storage medium [18].

To implement AFC quantum memory, rare-earth-ion doped crystals are particularly suitable due to the long coherence times of their optical 4f-4f transitions at cryogenic temperature [185, 220]. Long optical storage time has been demonstrated in rare-earth ion-doped crystal-based AFC quantum memory by using dynamical decoupling techniques to increase the spin coherence time [221, 104, 222].

The efficiency of the AFC quantum memory was improved by enhancing the preparation procedure of the AFC. These include optimization of the comb shape in Tm:YAG crystal [223] where some improvement in the efficiency has been demonstrated compared to the initial preparation procedure of the AFC [187, 101], and creation of high resolution (large

finesse) AFCs by optimizing the pulse sequence which has been demonstrated in Er:YSO using hyperfine levels [224] leading to improvement in the AFC quantum memory efficiency.

To achieve high efficiency in quantum memories, a large optical depth in the storage material is typically needed. However, in practice, simultaneously achieving high optical depth and long coherence times is difficult [225]. This trade-off is exemplified by the observation that the coherence time is usually inversely dependent on the doping concentration. So, to have high coherence times, it is preferable to work with lower optical depth (OD) rare-earth doped crystals. To overcome this limitation, it was proposed to incorporate the storage medium in an asymmetric optical cavity. By applying the impedance matching condition, unit efficiency can, in principle, be obtained with an effective optical depth of only one [19, 226]. In this situation, the memory efficiency is only limited by intrinsic atomic dephasing.

So far, several experiments have been carried out based on the impedance matching proposal [19, 226] using the AFC technique [115, 116, 117, 118, 119, 120]. To date, the best efficiencies obtained are 62% [120] for the storage time of $2\,\mu s$, 56% [115] for the storage time of $1.1\,\mu s$ and 53% [116] for the storage time of $2\,\mu s$. Based on the experimental results, between 12-20 fold enhancement in the storage efficiency has been obtained by putting the AFC memory in an impedance-matched optical cavity compared to the no cavity case. However, it has been experimentally difficult to measure the AFC properties, e.g., optical depth within the impedance-matched cavity [115, 118, 119] because it is no longer straightforward to determine it from the measured frequency-dependent transmission using Beers law, as is the case for a crystal without a cavity. The fact that no detailed general theoretical model for cavity-enhanced AFC quantum memory exists, makes it difficult to compare experiments to theory, and hence also to infer the system parameters from experiments. The original proposal [19, 226] assumed a memory bandwidth significantly smaller than the cavity bandwidth to satisfy the resonance condition, and so did not discuss the combs that are created at frequencies detuned from the cavity resonance. Also, the background absorption due to

imperfect optical pumping used to create the comb shape was ignored. Although, authors in Ref. [123, 124] have investigated the role of dispersion in AFC as a protocol closely associated to the slow-light-based storage protocols, so far there has not been a theoretical model for cavity-enhanced AFC quantum memory that includes the dispersion originating from the absorption engineering of ions to create the comb inside the cavity.

Here we develop a more general model that addresses all of these points. We extend the impedance-matched model beyond the resonance condition by including the round-trip phase shifts of light as travelling inside the cavity in the initial proposal [19] making it valid for any AFC bandwidth with a background absorption, and created at any detuning with respect to the cavity resonance. We show that, including dispersion, our developed model closely aligns with our own experimental results, and in particular enables prediction of the experimental memory efficiency at any detuning with respect to the cavity resonance. The paper is organized as follows: In sections 4.3 and 4.4 the theoretical model and the experiment performed are discussed. In section 4.5 the method to predict the cavity-enhanced AFC quantum memory reflectivity and efficiency is explained. Furthermore, we show results from the theory and compare them to the experimental data. In section 5.6 we elaborate on a comparison to a theoretical model without dispersion, and the conclusion and outlook are given in section 5.7.

4.3 Theoretical model for cavity-enhanced atomic frequency comb quantum memory

An AFC quantum memory consists of an ensemble of inhomogeneously broadened atoms engineered as periodically comb-like peaks in frequency domain (see figure 4.1), which is realized through frequency-selective optical pumping of atoms from the ground state to a metastable state, e.g., a hyperfine state. A resonant input pulse with the bandwidth that matches the comb bandwidth is collectively absorbed. After absorption of the light, the

collective excitation initially starts dephasing; however, after a time $t = 1/\Delta$, (Δ is the spectral distance between the peaks in Hz), due to the periodic structure of the comb, the excitation will be in phase again which leads to the echo pulse [18].

We consider an AFC quantum memory with optical depth contrast d_c and a background absorption optical depth d_0 inside a general asymmetric cavity with mirror reflectivities R_1 and R_2 where $R_1 < R_2 \approx 1$ (see figure 4.1) and apply the "sum over all round-trips" approach of a Fabry-Perot cavity. We include absorption factors both for the frequency comb and the background due to additional background absorption to obtain the reflected intensity from the cavity. Furthermore, to extend the impedance-matched proposal for off-resonant combs with an arbitrary bandwidth, we include the phases associated with each path in the sum over all round trips (compared to the on resonance equation (11) in Ref. [19]). The reflected amplitude ($E_{\text{out}}/E_{\text{in}}$) from the cavity [227, 228] can be written as

$$\frac{E_{\text{out}}}{E_{\text{in}}} = \frac{-\sqrt{R_1} + \sqrt{R_2}e^{-d(\nu)}e^{-i\Phi(\nu)}}{1 - \sqrt{R_1 R_2}e^{-d(\nu)}e^{-i\Phi(\nu)}} \quad , \tag{4.1}$$

where L is the length of the crystal, $d(\nu) = \alpha(\nu)\, L$ is the optical depth, and $\alpha(\nu)$ is the frequency-dependent absorption coefficient. In addition, the total round-trip phase is $\Phi = 2KL$, where $K = 2\pi\frac{n(\nu)}{\lambda}$ is the wavenumber, and $n(\nu)$ is the real refractive index of the matter inside the cavity. $\Phi(\nu)$ can be written as

$$\Phi(\nu) = 4\pi\frac{n(\nu)\,\nu L}{c} \quad , \tag{4.2}$$

where c is the speed of light in the vacuum.

Equation (4.1) for the reflected amplitude can be interpreted as the response function of the cavity. We will refer to both terms interchangeably. Since E_{out} contains terms which depend on the optical depth and the phases associated with each path in the sum over all round-trips, the reflectivity of the cavity will become frequency dependent over the comb bandwidth. Equation (4.1) is a general version of equation (11) in Ref. [19] and can be

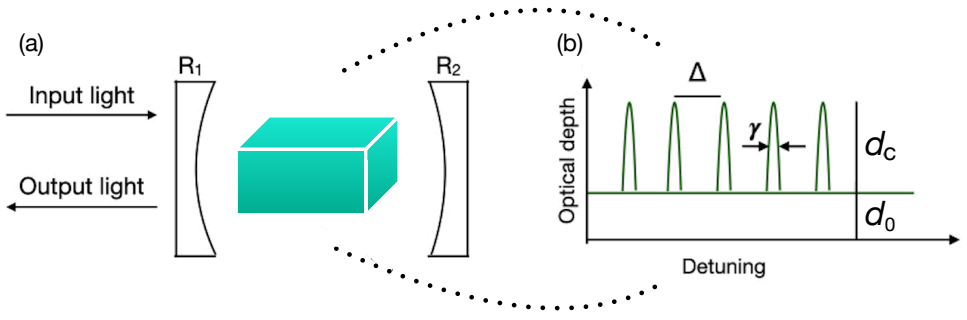

Figure 4.1: **(a)** Crystal inside a general asymmetric cavity with mirror reflectivities R_1 and R_2 where $R_1 < R_2 \approx 1$. **(b)** The natural inhomogeneously broadened absorption profile of the medium (Tm:YAG in this paper) is shaped into a comb structure where the peaks are separated by Δ and have a width (FWHM) of γ as shown on the right. The finesse of the comb is defined as $\mathrm{F} = \frac{\Delta}{\gamma}$. Note FWHM peak width γ is related to the peak width $\tilde{\gamma}$ through $\gamma = \sqrt{8\ln 2}\,\tilde{\gamma}$. Due to the comb structure, there will be a coherent re-emission after a time $\frac{1}{\Delta}$.

applied to both on-resonance and off-resonance conditions. In section 4.5, we use equation (4.1) to simulate the reflectivity of the cavity and compare it with the experimental data.

We assume an AFC with an engineered optical depth $d(\nu)$ of a series of Gaussian peaks with identical amplitudes (d_c), spacing (Δ), width ($\tilde{\gamma}$), and a constant d_0 which is the optical depth associated with the background absorption. The AFC optical depth $d(\nu)$ can be written as

$$d(\nu) = \sum_{k=1}^{9} d_c\, e^{-\frac{(\nu - b_k)^2}{2\tilde{\gamma}^2}} + d_0 \quad , \tag{4.3}$$

where the number 9 in the summation is the number of created teeth in the experiment, b_k is the center of each Gaussian function (each AFC tooth) and $b_k - b_{k-1} = \Delta$ (see figure 4.1). The optical depth of the crystal defines the initial $\alpha(\nu)$, and optical pumping to define the comb reshapes the natural absorption profile. The resulting profile can be described using d_0 for residual unaffected absorption, and $d(\nu)$ for the total absorption corresponding to the newly shaped comb features.

By including the dispersion originating from the atomic absorption in the model there is a frequency-dependent refractive index $n(\nu)$ in the phase Φ. The complex refractive index $\tilde{n}(\nu)$ can be written as $\tilde{n}(\nu) = n(\nu) + ik(\nu)$. The real part of the complex refractive index

$n(\nu)$ is responsible for the change in the phase of light (see equation (4.2)). The imaginary part of the complex refractive index $k(\nu)$ is related to the absorption coefficient as,

$$k(\nu) = \frac{\alpha(\nu)\, c}{4\pi\, \nu} \quad . \tag{4.4}$$

The real and imaginary parts of the complex refractive index $\tilde{n}(\nu)$ are connected through the Kramers-Kronig relations, through the real $\chi_r(\nu)$ and imaginary $\chi_i(\nu)$ parts of the susceptibility of a medium [125, 126, 229, 127, 230]

$$\chi_r(\nu) = \frac{2}{\pi}\mathcal{P}\int_0^\infty \frac{\nu'\chi_i(\nu')}{\nu'^2 - \nu^2} d\nu' \quad ,$$

$$\chi_i(\nu) = \frac{2}{\pi}\mathcal{P}\int_0^\infty \frac{\nu\chi_r(\nu')}{\nu^2 - \nu'^2} d\nu' \tag{4.5}$$

where $\mathcal{P}$ symbolizes the Cauchy principal value. Note that in these equations ν is the absolute frequency, whereas we show the detuning in most of the rest of the paper. Thus, a frequency-dependent absorption coefficient results in a frequency-dependent $k(\nu)$ and it affects the real refractive index $n(\nu)$. Using the Kramers-Kronig relations (equation (5)) we can write the the real part of the complex refractive index $n(\nu)$ as

$$n(\nu) = n + \frac{2}{\pi}\mathcal{P}\int_0^\infty \frac{\nu' k(\nu')}{\nu'^2 - \nu^2} d\nu' \quad , \tag{4.6}$$

n is the constant real refractive index of the host crystal (YAG in this paper) [231, 232]. Putting the obtained $n(\nu)$ for the comb in equation (4.2), the change in phase of light Φ is calculated and one can write the equation for Φ as

$$\Phi(\nu) = 4\pi\frac{\nu L}{c}\left(n + \frac{2}{\pi}\mathcal{P}\int_0^\infty \frac{\nu' k(\nu')}{\nu'^2 - \nu^2} d\nu'\right) \tag{4.7}$$

Note that to calculate the real refractive index $n(\nu)$ at each frequency the absorption coefficient must be defined over the entire frequency range. Figure 4.2 **a** shows an example of the

employed optical depth for a comb created close to the cavity resonance. Employing such an absorption coefficient allows us to calculate the real refractive index $n(\nu)$ over the comb. Figure 4.2 **b** shows the calculated real refractive index $n(\nu)$ for the comb shown in figure 4.2 **a**. Using equation (4.7) for Φ, one can calculate the reflectivity of the cavity-enhanced AFC quantum memory as a function of frequency which will be done in section 4.5.

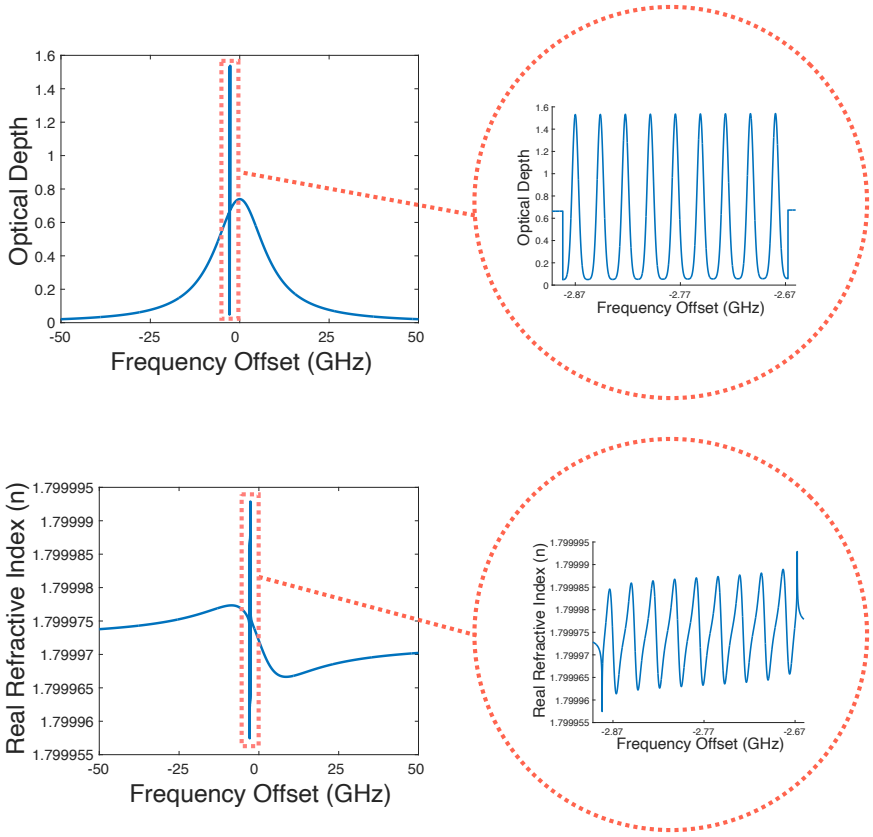

Figure 4.2: **(a)** The natural inhomogeneously broadened optical depth of Tm:YAG crystal with the comb-shape engineered optical depth for the comb at -2.7720 GHz detuning with respect to the center of the inhomogeneous broadening embedded into that. (**Inset**) The created comb-shaped optical depth over the comb bandwidth. **(b)** The calculated real refractive index $n(\nu)$ over the entire frequency range for the optical depth shown in (a). (**Inset**) $n(\nu)$ over the comb width.

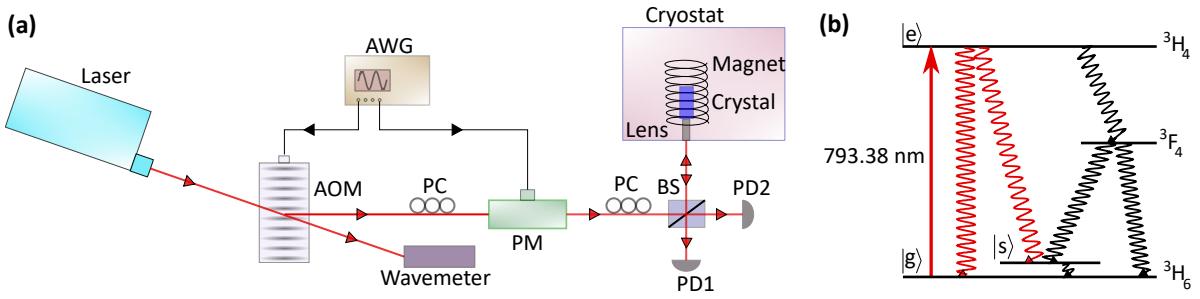

Figure 4.3: **(a)** Schematic of the experimental setup. A tunable external cavity diode laser serves as the light source. The first order of the acousto-optic modulator (AOM) goes through a polarization controller (PC) before passing an electro-optic phase modulator (PM). An arbitrary waveform generator (AWG) sends electrical signals to drive the AOM and the PM and control the experimental sequence. The 50/50 beamsplitter ensures that the same optical fiber transmits light to the crystal and collects the reflected light. The photodetector PD1 detects the back-reflected light from the crystal cavity whereas detector PD2 monitors the input laser light intensity. The sample is kept inside an adiabatic demagnetization refrigerator (ADR) and another superconducting magnet placed inside the cryostat applies a DC magnetic field to the crystal sample. **(b)** Energy level diagram of Tm^{3+} ion. For optical pumping, the laser is tuned to the $|g\rangle \rightarrow |e\rangle$ transition. Under the application of an external magnetic field, the ground state splits into Zeeman levels $|g\rangle$ and $|s\rangle$. The latter serves as the auxiliary level for the formation of the atomic frequency comb (AFC). The echo after the storage time is emitted at the $|g\rangle \rightarrow |e\rangle$ transition frequency.

4.4 Experiment

We have performed our experiments in a 0.1% thulium-doped $Y_3Al_5O_{12}$ (Tm:YAG) crystal cavity, the same as used in Ref. [119]. The optical transition wavelength of Tm^{3+} is well suited for free-space quantum communication, making it attractive for ground-to-satellite communication, for example, for Canada's QEYSSat satellite mission [233, 234, 235, 236]. Furthermore, its wavelength is compatible with quantum memories based on rubidium gas, allowing the possibility of designing hybrid platforms [64, 147]. Tm:YAG has wide inhomogeneous broadening (∼20 GHz) and narrow homogeneous linewidth (∼10 KHz) [182], in principle, permitting broadband, multimode, and long-lived quantum memories.

Our crystal is approximately 4 mm long and the AFCs are generated at a cryogenic temperature of 1.5 K. The two ends of the crystal surface are reflection coated with approximate reflectivities $R_1 = 40\%$ on the front end and $R_2 = 99\%$ on the back end [119] to satisfy the

impedance matching condition. As a result, the created asymmetric optical cavity has a finesse close to 7 and free spectral range close to 20 GHz.

Figure 4.3 **a** shows the experimental setup. Light near 793 nm from an external cavity diode laser (ECDL) passes through an acousto-optic modulator (AOM) driven at 400 MHz. While the zeroth order of the AOM is monitored on a wavemeter to measure the wavelength of the laser, the first diffracted order is directed to the crystal in the cryostat after passing through a phase modulator (PM) and a 50/50 beamsplitter. The energy level structure of Tm^{3+} ions is shown in figure 4.3 **b**. Under the application of an external magnetic field, the ground state $^3H_6$ splits into the Zeeman levels $|g\rangle$ and $|s\rangle$. The phase modulator is used to carve out the combs by selectively pumping ions in the frequency domain from the ground state $|g\rangle$ to the spin state $|s\rangle$ [119], mediated by the excited state $|e\rangle$. The 50/50 beamsplitter is employed to be able to send and receive photons by back-reflection from the cavity using the same optical fiber. The optical fiber is terminated in a ferrule, which is placed in front of a gradient index (GRIN) lens. Both the ferrule and lens are inserted in a tight-fitting 50 mm-long capillary, which is fixed at one end to the crystal mount and at the other to a xyz nano-positioning stage. In this way, movement of the nanopositioner will change the angle of the capillary, and, thus, the enclosed fibre and GRIN lens, to the crystal surface allowing the input mode to be aligned to the cavity mode.

AFC combs are created at varying frequencies across the cavity spectrum by tuning the ECDL frequency. For measurements of the cavity reflection spectrum, the ECDL frequency can also be continuously swept across nearly 50 GHz. The strength of the external magnetic field controls the Zeeman splitting between the spin levels $|g\rangle$ and $|s\rangle$. We choose a magnetic field value close to 500 Gauss such that during the optical pumping in the AFC preparation, the atoms from the AFC troughs are almost all moved to the AFC peaks, increasing their optical depth nearly by a factor of two [119]. This efficient AFC preparation ensures that almost all the atoms participate in the absorption and re-emission process. An arbitrary waveform generator (AWG) drives the AOM and the PM to create the experimental sequence

for optical pumping and input pulse generation. After 50 ms optical pumping and 5 ms wait time, we send in narrow-band input pulses generated by the AOM. The back-reflected light, after passing through the beamsplitter, is collected on one of the photodetectors (PD1 in figure 4.3 **a**). We tune the laser to different wavelengths and record the AFC scans at each wavelength. The scans are obtained with the help of a phase modulator, which generates a linear chirp spanning the whole AFC width. The frequency spanned is 200 MHz in 100 μs. The photodetector PD1 detects the chirped light after interacting with the AFC profiles and the AFC scans are obtained on an oscilloscope connected to PD1. We repeat the experimental sequence 100 times with a 200 ms interval between each repetition to reduce the experimental noise and generate a steady AFC. We take the average of these 100 scans on the oscilloscope to obtain the effective AFC trace. After the AFC trace is collected at a particular wavelength, we send an input pulse centered at that wavelength. We observe the unabsorbed part of the pulse and the echoes emitted on the oscilloscope connected to PD1. Similar to the AFC scans, we repeat the experimental sequence 100 times and take the average to obtain the effective traces for the pulses and the echoes. To obtain the input electric field (E_{in}) in Equation (4.1), we go to an off-resonant frequency, greater than 200 GHz away from the center of the inhomogeneous broadening. Since almost no atoms interact with the incident light at this wavelength, the AFC trace is close to a flat line. Also, virtually no part of the incident pulse is absorbed at this wavelength and no echoes are emitted. The unabsorbed part of the incident pulse is now taken as the input pulse for calculating the memory efficiencies. We monitor the fluctuations in the input power of the laser as we tune its wavelength by connecting the free port of the beamsplitter to another photodetector (PD2) as shown in figure 4.3 **a**. We calculate the experimental efficiencies by dividing the area of the first echo at each wavelength by the area of the input pulse. The maximum experimental efficiency is obtained for the comb close to the cavity resonance frequency and at the detuning of -2.7720 GHz from the resonance frequency of the atoms (all the detunings in the present manuscript are with respect to the center frequency of the inhomogeneously

broadened atomic transition, unless otherwise mentioned).

Using the theory discussed in section 4.3 and this experimental setup we are able to extract some relevant features of our memories and verify the performance of our new model in the following section.

4.5 Results and Discussion

In this section, we show and analyze the experimental results. First, equation (4.1) is fitted with the experimental data for the reflectivity of the crystal cavity with no comb carved into it and the values of the crystal cavity properties are obtained as the fitting parameters in section 4.5.1. Note that equation (4.1) is for the reflected amplitude and not the reflected power ($|\text{reflected amplitude}|^2 = \text{reflected power}$). Next, the crystal cavity with a spectral-shaped AFC is considered. By fitting the model to the measurement results for the reflectivity and using the obtained fitting parameters for the crystal cavity properties from the previous step, the shape and optical depth of the created combs are extracted as shown in section 4.5.2. The fitting scripts are all coded in Matlab [237], and the curve fitting and optimization toolboxes are applied. Finally, the obtained comb properties from the fitting are used to predict the efficiencies of the created cavity AFC quantum memories at various frequency offsets across the cavity profile in section 4.5.3, and the predicted memory efficiencies are compared to the experimental results.

4.5.1 Cavity reflectivity without comb

The reflected power at different frequencies for the crystal cavity with no AFC carved into it can be obtained using equation (4.1). The values of the crystal cavity properties are obtained as the fitting parameters from fitting equation (4.1) in the model with the experimental normalized reflected power for the Tm:YAG crystal cavity with no comb engineered into it as measured in [119]. The real refractive index $n(\nu)$ in equation (4.2) is frequency dependent

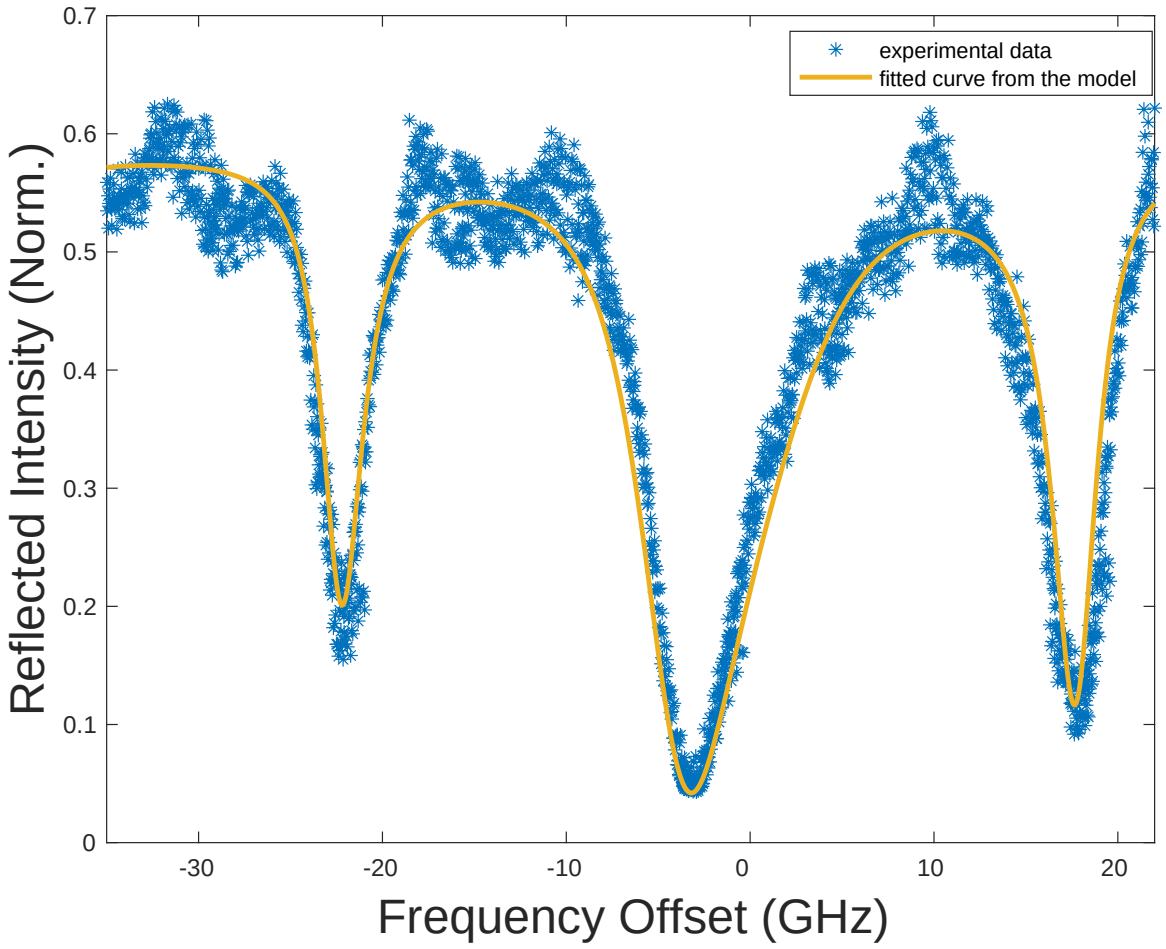

Figure 4.4: Experimental cavity reflectivity and the fitted curve from the model.

Table 4.1: Obtained parameters for crystal cavity properties from cavity reflectivity without comb (see figure 4.4).

Crystal Cavity Properties		
Peak absorption coefficient	α_{peak} (cm^{-1})	1.70
Front mirror reflection	$r_1 = \sqrt{R_1}$	0.6927
Back mirror reflection	$r_2 = \sqrt{R_2}$	0.9999
Constant refractive index	n	1.799972
Cavity/crystal length	L (cm)	0.4350
Beam-splitter ratio	s	1.7142

and can be obtained using equation (6) (section 4.3). The inhomogeneously broadened absorption spectrum of Tm in YAG is a Lorentzian function centered at $\nu_0 = 377,868\,\text{GHz}$, with a FWHM of $\Gamma_{\text{in}} = 17\,\text{GHz}$ [238]. Figure 4.4 shows the data for the reflectivity of the cavity at different frequencies and the fitted curve to the data. We see three cavity resonances in the figure. Near impedance-matching occurs at the frequency offset of $-3.19\,\text{GHz}$. It should be noted that the impedance-matched point is close to the perfect impedance-matching: theoretically 100% of the input light should be absorbed at the impedance-matched frequency (zero reflection); however, the experimental value got close to 95% absorption. The obtained impedance-matched frequency for the fitted curve is in good agreement with the experimental value of $-3.4 \pm 0.5\,\text{GHz}$ where the uncertainty in the measured value comes from our optical wavemeter smallest significant digit. The maximum value of the Lorentzian function of the absorption spectrum is also set as a fitting parameter. This takes into account possible variations in crystal growth and sections of the boule from which our sample was cut. Although the experimental cavity reflection data (figure 4.4) is measured through a 50/50 beamsplitter, the measured maximum reflectivity value of slightly more than 0.5 in figure 4.4 implies the employed beamsplitter was not exactly a 50/50 one. To account for that there is a factor of s as a fitting parameter so that (reflected power / s) is fitted to the experiment, with $s = 2$ corresponding to an ideal 50/50 beamsplitter. The obtained values for the crystal cavity parameters are shown in table 4.1. Also, the obtained peak absorption coefficient ($\alpha_{\text{peak}} = 1.70\ \text{cm}^{-1}$) is in good agreement with the measured value of between $1.9\,\text{cm}^{-1}$ to $2.3\,\text{cm}^{-1}$ [182, 238].

In the next step the obtained fitting parameters for the crystal cavity properties are used to analyze the experimental reflectivity of the cavity-enhanced AFC quantum memory.

4.5.2 Cavity reflectivity with comb

In this section the experimental data for the reflected power of the cavity-enhanced AFC quantum memories created at different detunings are analyzed to extract the combs' features.

Table 4.2: Obtained comb parameters for cavity-enhanced AFC quantum memories created at different detunings across the cavity profile (see figure 4.5).

Comb Properties	Comb **a**	Comb **b**	Comb **c**
d_c	1.5260	1.4867	1.4261
Δ (MHz)	23.4598	23.8160	24.3382
$\tilde{\gamma}$ (MHz)	3.6063	2.9755	3.4462
d_0	0.2008	0.0526	0.0254

As stated in the section 4.3 it is assumed the AFC is a series of Gaussian functions with the same amplitude (d_c), spacing (Δ), width ($\tilde{\gamma}$), and with a constant background absorption d_0 (see equation (4.3)). We use equation (4.7) to calculate the phase Φ. Then equation (4.1) is fitted to the experimental data for the reflected power of each of the memories at different wavelengths and the comb parameters d_c, Δ, $\tilde{\gamma}$, and d_0 are extracted as the fitting parameters. The fitted curves to the experimental reflected power using the model equations are shown in figure 4.5 and the extracted fitting parameters are shown in table 4.2 for three AFCs created at three critical regions across the cavity features (see figure 4.5 **d**). The first one is the AFC created far from the cavity resonance at the detuning of 2.2765 GHz with respect to the resonance frequency of the atoms (see figure 4.5 **a**). The second one is close to the impedance-matched frequency at the detuning of -2.7720 GHz (see figure 4.5 **b**). The third comb is in an intermediate regime, and on the other side of the cavity resonance at the detuning of -3.8675 GHz (see figure 4.5 **c**).

Figures **a**, and **c** in 4.5 show there is an asymmetry (skewness) at the bottom of the experimental data for the reflectivity of the combs created at 2.2765 GHz and -3.8675 GHz, which is captured in the fitted curves obtained from the model. In figure 4.5 for the shown combs, the skewness at the bottom of the reflected power data changes direction as one moves from one side to the other side of the cavity resonance, which is also true for all the other combs that are not shown, and is captured by the model. Also, for the comb created at -3.8675 GHz detuning (see figure 4.5 **c**) there is an skewness around its lowest point at

the bottom of the experimental data for all of the teeth in the comb captured to some extent in the model (for most of the teeth in the comb). Moreover, note the shapes at the top of the comb created close to the impedance-matched point at $-2.7720\,\mathrm{GHz}$ frequency offset, and the fact that the maximum of the experimental reflectivity is lower as compared to the other two combs. As one can see in figure 4.5 **b**, relatively similar features are obtained by the model.

Discussing the obtained fitting parameters for the comb properties in the model, the spacing (Δ) between the teeth, which is related to the storage time of the AFC quantum memory, is very similar amongst the created AFCs as expected, and approximately the same as the model. Considering the storage time of 42 ns for the memories, one can obtain $\Delta = 23.81\,\mathrm{MHz}$, which is in good agreement with the extracted Δ values in table 4.2. Thus, the challenges to understand the comb features are mainly focused on achieving the true values for the atomic absorption depth and the width of the related combs. The obtained value of $\tilde{\gamma}$ in the model for each comb shown in figure 4.5 does not change a lot within different combs resulting in nearly the same values for the finesse of different combs as expected from the experiment. Considering the pumping procedure (section 4.4) and the inhomogeneous broadening in the absorption spectrum of Tm:YAG crystal, we expect somewhat lower d_c values compared to the ones obtained from the model. This leads to a difference between the theoretical and experimental efficiency which is discussed in the next section.

4.5.3 Memory Efficiency

We now calculate the efficiencies of the created cavity-enhanced AFC quantum memories numerically taking the following steps. First, we take the Fourier transform (FT) of the input pulse sent for storage to the memory. Then by multiplying the input pulse in the frequency domain by the response function of the cavity (which contains the phase information), the output from the cavity AFC quantum memory is obtained in the frequency domain. Finally, the numerical inverse Fourier transform (FT) results in the output in the time domain.

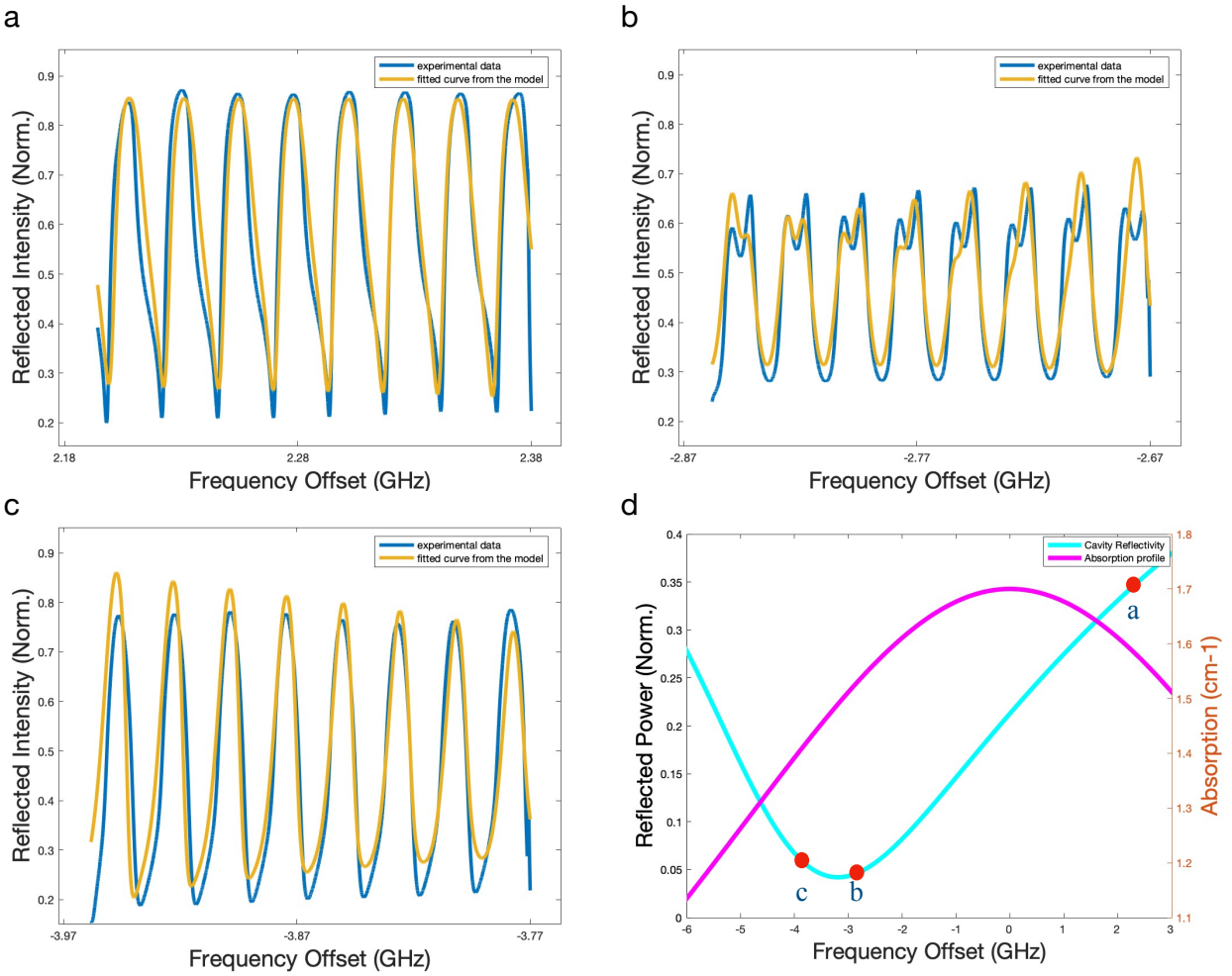

Figure 4.5: Experimental cavity-enhanced AFC quantum memory reflectivity and the fitted curves for three combs created at three critical regions across the cavity features. (**a**) shows a comb far from the impedance-matched frequency (at the detuning of 2.2765 GHz). (**b**) shows a comb close to the impedance-matched frequency (at the detuning of −2.7720 GHz). (**c**) shows a comb in an intermediate regime (at the detuning of −3.8675 GHz). (**d**) The inhomogeneously broadened absorption spectrum of (Tm:YAG) crystal and the reflectivity of the (Tm:YAG) crystal cavity over a smaller range (the range of the created combs). The locations of the above combs are labeled **a**, **b**, and **c** corresponding to the combs in subfigures **a**, **b**, and **c**.

Calculating the square of the absolute value of the output to obtain the output intensity and then plotting the output intensity with respect to time one can obtain the cavity-enhanced AFC quantum memory efficiency by calculating the area under the first echo, i.e., the pulse that occurs after the storage time of the memory, and dividing it by the integrated input intensity. The obtained value is the calculated numerical efficiency of the cavity-enhanced AFC quantum memory. The numerical calculation is performed by coding in Matlab and using the Fast Fourier transform (FFT) algorithm.

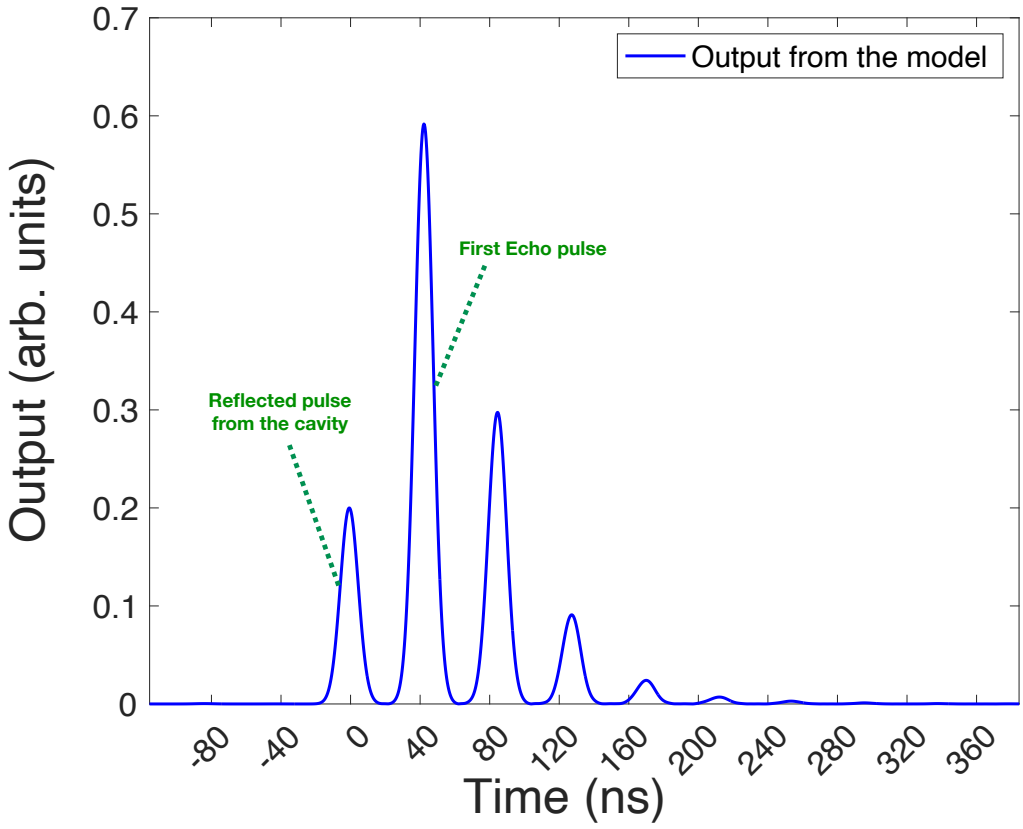

Figure 4.6: The output pulses obtained theoretically for a comb close to the impedance-matched frequency. Memory storage time of 42 ns is visible which is the difference between the occurrence time of the reflected part of the input pulse (not being absorbed and stored) and the first recalled (echo) pulse.

Figure 4.6 shows the obtained output pulses with respect to time from the model for a cavity-enhanced AFC quantum memory created near the impedance-matched frequency. In the obtained output we see several pulses where the first one is part of the input pulse

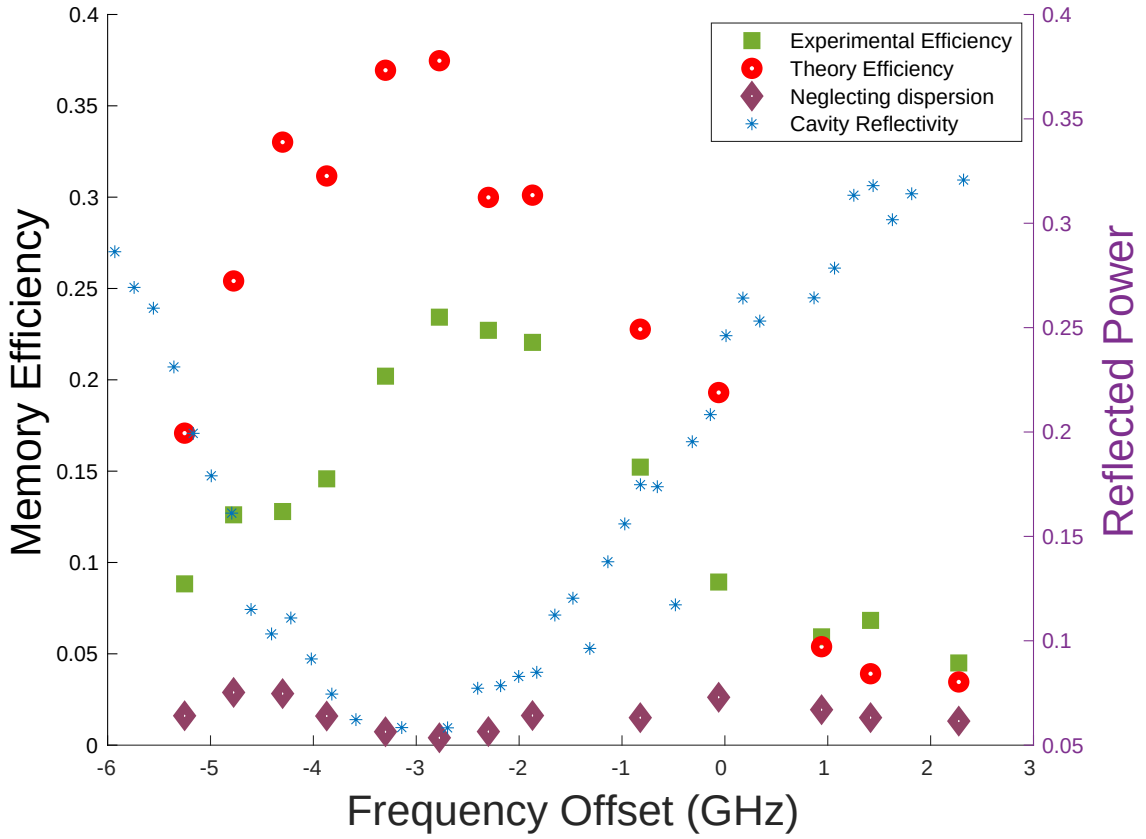

Figure 4.7: The figure shows the measured experimental efficiency of the created combs, the theoretical efficiency from the model including dispersion, the efficiency obtained when neglecting dispersion, and the cavity reflectivity.

reflected from the cavity, and the other remaining pulses are the echo pulses in a decreasing order.

The calculated efficiencies for all the combs created at different detunings across the cavity features are shown in figure 4.7 along with the measured experimental memory efficiencies. Based on the experimental data the maximum echo emission (efficiency) occurs for the AFC created close to the impedance-matched frequency. The obtained efficiency trend in the model is the same as the experiment, with the maximum experimental efficiency for the comb created near the impedance-matched frequency.

The model still does not capture all features of the experimental reflectivity. For example, there is an asymmetry over the comb bandwidth in the fitted curve in figure 4.5 **c**, which is not exactly the same as the experiment. Also, for the comb created close to the impedance-

matched point (figure 4.5 **b**) we do not perfectly capture the features at the top of the experimental curve. Indeed, for different combs, these features appear differently. This leads to an inaccurate estimation of the combs' features and likely to an overestimation of the calculated memory efficiencies. These facts suggest that although the skewness in the data may not seem that important at first look, it is important for being able to predict the combs' features precisely, and, so, to predict efficiencies close to the experimental values.

4.6 Comparison to a theoretical model without dispersion

It is worth investigating the effect of neglecting dispersion due to the atomic absorption, leading to a constant real refractive index n in equation (2) for the YAG crystal [231, 232]. One can do the process of fitting equation (4.1) to the experimental data for the cavity reflectivity without and with comb the same as 4.5.1 and 4.5.2 and extract the comb parameters as the fitting parameters. Doing so the skewness at the bottom of the experimental reflected power data for the combs created far from the impedance-matched frequency (figure 4.5 **a**), and in an intermediate regime (figure 4.5 **c**), and also the shapes at the top of the comb created close to the impedance-matched point (figure 4.5 **b**) are not captured in the fitted curves.

Talking about the obtained fitting parameters, although for each comb the obtained values of Δ, and d_0 remain relatively the same as before and there is a small change in the obtained value of $\tilde{\gamma}$, considering the pumping procedure (section 4.4) there is a noticeable misestimation in the obtained d_c values of the created combs. Our model lets us obtain more reasonable d_c values for the created combs.

Employing the same steps as 4.5.3, we can calculate the efficiencies of the created AFCs at different detunings across the cavity profile. Figure 4.7 shows that the calculated efficiency for all the created combs is lower than the experimental results. Far from the cavity

resonance there is only slight disagreement between the theoretical and experimental efficiencies, but as one gets closer to the cavity resonance the disagreement becomes much more prominent. This suggests that dispersion becomes more important for the combs created closer to the impedance-matched frequency (cavity resonance).

Note that the underestimation of the efficiency in the absence of dispersion is not purely due to the misestimation of d_c. Using the refractive index (n) as a fitting parameter, it is possible to obtain reasonable values for d_c even in the absence of dispersion, but the predicted efficiencies are still much too low. The underestimation of the efficiency is also due to the violation of causality in the absence of dispersion, which leads to an unphysical echo occurring before the input pulse associated with a reduction of the physical echos.

4.7 Conclusion and outlook

In summary, we have developed a model for cavity-enhanced AFC quantum memory, which helps to address the challenges of the measurement of comb properties inside the cavity. Employing the experimental cavity reflectivity, our model allows us to estimate the comb properties and the efficiency of the cavity-enhanced AFC quantum memory with a background absorption and arbitrary bandwidth created at any frequency offset with respect to the cavity resonance. Using the model, one obtains realistic values for the optical depth, as well as the correct trend for the efficiencies (they are maximum near resonance). Furthermore, the predicted values are in semi-quantitative agreement with the experimental ones. For comparison, we have also shown that a model without including dispersion completely fails to predict the memory efficiencies. Our results confirm the important role of dispersion effects in successfully modeling cavity-enhanced AFC quantum memories.

The model still does not capture all the features, which may be related to the fact that predicted efficiencies are somewhat higher than those achieved in experiments. This discrepancy is likely related to a number of points. First, the shape of the individual created teeth is

not a perfect match to that of the model; they are closer to a rectangular shape rather than the assumed Gaussian shape. Second, residual reflectivity from the lenses causes some additional modulation on the transmitted intensity - due to a cavity being formed between the lens and the crystal - which affects the obtained parameters for the cavity. Third, averaging the experimental runs for each output trace can influence the experimental efficiency if some of the contributing runs featured lower efficiencies, e.g. from occasional laser instability.

Going forward, to upgrade AFC memory from predetermined storage time to on-demand readout, one can transfer the coherent excitation to a long-lived ground state spin coherence using optical control pulses which produce noise in the system [18, 102, 239, 240, 241, 216]. Employing the Stark effect it is possible to have an on-demand AFC quantum memory without the need for applying optical pulses and as a result being noise free [242].

Recently, a chip-integrated AFC quantum memory has been demonstrated using a thin-film lithium niobate waveguide doped with thulium (Tm^{3+}) rare-earth ions. Thin-film lithium niobate offers a more compact device structure compared to bulk material and is compatible with wafer-scale fabrication [243]. It would be interesting to adapt our theoretical model to a cavity with a waveguide crystal instead of a bulk crystal. Considering the new fabrication techniques for the waveguides and photonic materials being available [244], compared to the older, lossy diffusion waveguides [245], an integrated cavity platform should be feasible experimentally. Advancement in nanofabricated rare-earth ion doped crystals platforms may enable arbitrary-scale arrays of quantum memories for multiplexed quantum repeaters [121].

This work is focused on the impedance-matched weak coupling regime. There are some works more focused on the strong coupling regime [246, 247] which have the potential advantage of faster and more efficient memory preparation by Purcell enhancing the spontaneous decay rate [121]. One potential future direction is to investigate the effect of going into strong light-matter coupling regime on the memory storage and retrieval process, where new phenomena may arise [248].

In sum, we anticipate that this work can further inform the next generation of cavity-enhanced quantum memories leading to more rapid progress towards their application in quantum networks.

Acknowledgments

We wish to thank Roohollah Ghobadi, and Erhan Saglamyurek for useful discussions. This work was supported by the Alberta Major Innovation Fund (MIF), the High-Throughput Secure Networks (HTSN) Program of the National Research Council (NRC), Canada Foundation for Innovation (CFI), Alberta Innovates, and the Natural Sciences and Engineering Research Council (NSERC).

Chapter 5

Exploring the feasibility of probabilistic and deterministic quantum gates between T centers in silicon

5.1 Preface

T center defects in silicon offer an attractive platform for quantum technologies owing to their unique spin properties and compatibility with mature silicon technologies. Here, we investigate several gate protocols between individual T centers, with a particular focus on photon interference-based scheme with feedback that can achieve success probabilities above 50%. We present the first analytical calculations of its entanglement fidelity and efficiency, and comprehensively evaluate and compare the performance of all the schemes.

This work was carried out in collaboration with a few co-authors. My primary contributions to to this work include investigating various potential gate schemes between individual T centers in silicon, quantitatively analyzing and comparing the schemes, and evaluating them based on metrics such as fidelity, efficiency, and gate time. I also wrote the initial draft of the manuscript and incorporated revisions based on feedback from the other co-authors.

Exploring the feasibility of probabilistic and deterministic quantum gates between T centers in silicon

arXiv:2508.06474 (2025)

Shahrzad Taherizadegan[1], Faezeh Kimiaee Asadi[1], Jia-Wei Ji[1], Daniel Higginbottom[2], and Christoph Simon[1]

[1]*Department of Physics & Astronomy, Institute for Quantum Science and Technology, University of Calgary, 2500 University Drive NW, Calgary, Alberta T2N 1N4, Canada*

[2]*Department of Physics, Simon Fraser University, Burnaby, BC V5A 1S6, Canada*

Abstract

T center defects in silicon provide an attractive platform for quantum technologies due to their unique spin properties and compatibility with mature silicon technologies. We investigate several gate protocols between single T centers, including two probabilistic photon interference-based schemes, a near-deterministic photon scattering gate, and a deterministic magnetic dipole-based scheme. In particular, we study a photon interference-based scheme with feedback which can achieve success probabilities above 50%, and use the photon-count decomposition method to perform the first analytical calculations of its entanglement fidelity and efficiency while accounting for imperfections. We also calculate the fidelity and efficiency of the other schemes. Finally, we compare the performance of all the schemes, considering

current and near-future experimental capabilities. In particular, we find that the photon interference-based scheme with feedback has the potential to achieve competitive efficiency and fidelity, making it interesting to explore experimentally.

5.2 Introduction

Quantum gates and entanglement generation schemes are foundational to realize future quantum technologies. They are essential for processing quantum information in quantum computers [21, 23, 22] and for the generation, storage, and swapping of entanglement for long-distance quantum communication through quantum repeaters [15, 24], paving the way for building the future global quantum internet [1, 10, 11].

Solid-state systems have attracted considerable attention as a platform for future quantum networks elements, including quantum memories [249, 210, 211, 17, 180]. Quantum gates and entanglement generation schemes have been proposed and implemented in various solid-state systems, such as rare-earth ions doped in crystals [250, 251, 252], nitrogen-vacancy (NV) centers [253], and silicon-vacancy (SiV) centers in diamond [254, 255].

The family of silicon defects have been investigated for decades starting even before the development of quantum technology [194, 192, 197, 198, 199, 200]. These defects, which exhibit sharp spectral features, are produced by irradiation or heat treatment, and are therefore often referred to as radiation damage centers. The T center in silicon has recently drawn significant attention in the context of quantum technology due to its unique features [193]. Silicon is an attractive host due to its compatibility with the current established electronics and photonics platforms. The T center in silicon offers long lived electron and nuclear spins, and, importantly, spin-selective bound exciton excited state optical transitions at 1326 nm wavelength in the telecommunication O-band [91] making it an ideal matter-photon interface. The T center in isotopically purified ^{28}Si offers enhanced electron and nuclear spin lifetimes and reduced inhomogeneous broadening of optical transitions.

T centers have also been created and studied in commercial materials other than bulk silicon such as the 220 nm device layer of silicon-on-insulator wafers [196, 195] and integrated silicon photonic waveguides [201].

Besides, some of us have explored the potential of T center ensembles for implementing various quantum memory and transduction schemes by characterizing the T center spin ensemble, measuring optical depth, and discussing achievable efficiency [150].

Figure 5.1 **a** illustrates the atomic structure of the T center in silicon, as proposed by [256] and later confirmed through observations in [91] and a first-principles study in [257]. Figure 5.1 **b** depicts the level structure and relevant optical transitions of the T center. The characteristics of the ensemble of T centers in bulk silicon are shown in figure 5.1 **c**.

So far, Ref. [93] has shown the first demonstration of entanglement generation between the electron spins of two remote individual T centers using the photon interference-based scheme proposed by Barrett and Kok [209]. A CNOT gate in a single T center, with the control and target being the nuclear and electron spins (C_nNOT_e) was also demonstrated by Rabi oscillations driving the $MW_{\Downarrow}$ transition [93]. Assuming enhancements in the fabrication of integrated T centers and that the bulk T center properties represent the ultimate performance of integrated devices, Ref. [93] also evaluated the potential achievable efficiency and the maximum fidelity of performing the interference-based Barrett-Kok entanglement distribution protocol for future T center systems.

The gate scheme discussed in Ref. [93] is probabilistic, with a maximum theoretical success probability of 50%. Considering the limitations of current experimental capabilities, the practical success rate is lower, imposing even greater overheads for various applications. This raises interest in exploring alternative schemes that could either be deterministic or achieve higher success probabilities given current and near-future experimental potential. In particular, implementing feedback during the measurement based on photon counting following the photon interference-based scheme as proposed in [258] promises a higher success probability compared to the scheme discussed in Refs. [93, 209] and unit efficiency in the

a

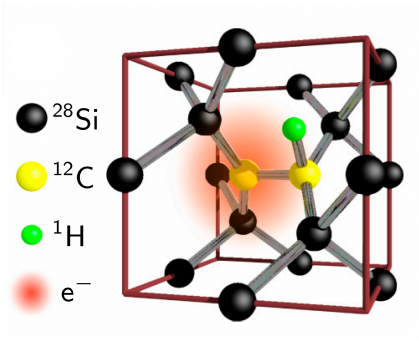

b

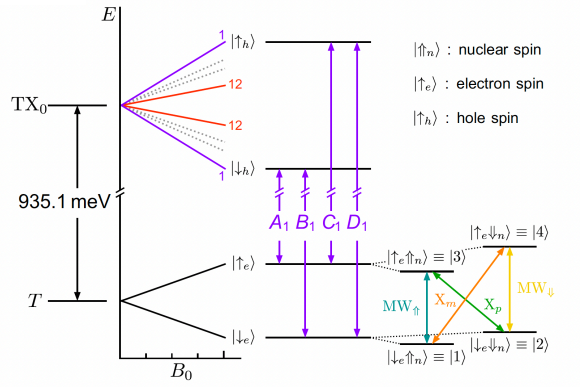

c

T_{1h}	$0.94\,\mu s$	T_{2h}	$0.46\,\mu s$
T_{1e}	beyond 16 s	T_{2e}	2.1 ms
T_{1n}	beyond 16 s	T_{2n}	1.1 s

Figure 5.1: **(a)** shows the atomic structure of the T center in silicon based on the proposal of Ref. [256]. Figure from Ref. [91]. **(b)** Energy level structure of T center and the optical transitions A_1, B_1, C_1, D_1 of the TX_0 bound exciton excited state. The anisotropy of the unpaired hole spin in the bound exciton state results in 12 independently addressable orientational subsets. Figure from [150]. **(c)** Optical excited state and ground state properties of T centers in bulk silicon [91, 150]. T_1 and T_2 represent the lifetimes and coherence times, respectively, while h, e, and n denote the hole spins, electron spins, and nuclear spins.

ideal case.

Here, we analyze this scheme and apply the photon-count decomposition method described in Ref. [259] to derive analytical expressions for its fidelity and efficiency, accounting for various imperfections, including optical decoherence, spin dephasing, photon loss, and

collection and detection inefficiencies. We use our results to evaluate the performance of this scheme and explore the feasibility of implementing other schemes for T centers. We quantitatively analyze these schemes based on previous works [259, 260, 261], which were originally developed for different systems. Finally, we compare their performance in light of current experimental advancements. Our findings suggest that the photon interference-based scheme with feedback offers a competitive combination of efficiency and fidelity, making it worth investigating experimentally.

We discuss implementing probabilistic protocols based on photon interference, both with and without feedback in section 5.3. Additionally, we examine a near-deterministic photon scattering-based gate in section 5.4 and a deterministic magnetic dipole-based gate in section 5.5. For each scheme, we estimate key characteristics, such as fidelity, efficiency, and gate time. In section 5.6, we compare the performance of the schemes. Finally, the conclusion and outlook are given in section 5.7.

5.3 Probabilistic photon interference-based gates

First, we discuss the photon interference-based (IB) scheme in subsection 5.3.1. Next, in subsection 5.3.2, we quantify the performance of the IB scheme with feedback (IBF). It is worth noting that these entanglement generation protocols can be transformed into a controlled-Z (CZ) gate by changing the measurement basis to a mutually unbiased basis [262].

5.3.1 Interference-based scheme

The interference-based (IB) entanglement generation scheme, introduced by Barrett and Kok, is widely used in quantum networks and distributed quantum computing [209]. It has been demonstrated experimentally for entanglement generation in several systems e.g., two trapped ytterbium ions in vacuum chambers separated by 1 m [263], ytterbium ions in

nanophotonic crystal cavities [264], and nitrogen–vacancy (NV) centers in diamond with a separation of 3 m [253]. Recently, this scheme has been demonstrated experimentally in T centers separated by 6 m [93].

Let us consider two three-level atoms with long-lived ground states $|\uparrow\rangle$, and $|\downarrow\rangle$ (the electron spins), and an excited state $|e\rangle$ (the hole spin) which decays to $|\downarrow\rangle$. This scheme is implemented by preparing the atoms in the superposition of their ground states, $(|\uparrow\rangle + |\downarrow\rangle)/\sqrt{2}$. Then, an optical π pulse is applied to each qubit, coherently driving the $|\downarrow\rangle \leftrightarrow |e\rangle$ transition. The resulting emissions from both systems are interfered on a beam splitter, and the system is left to wait until the detection time T_d to detect exactly one photon. Assuming the photons emitted by the two atoms are indistinguishable, the two atoms will be projected onto one of the maximally entangled Bell states. Due to photon loss, it is possible in reality to detect a single photon even when both atoms are in the state $|\downarrow\downarrow\rangle$. To remove such a possibility both qubits' spins are flipped and the process is repeated. The state $|\downarrow\downarrow\rangle$ is flipped to $|\uparrow\uparrow\rangle$ and will emit no photons. Detection of another photon in the second round heralds the entanglement generation [209, 253].

Thus, the entanglement time for the IB scheme is approximately $T_{IB} = 2\,T_d + \delta t$ where δt is the time to perform the spin flip. Since the final maximally entangled state can be one of two Bell states out of the four Bell components of the initial state, the maximum theoretical efficiency of the scheme is $\eta_{IB} = 0.5$. The efficiency of Bell state measurement can in principle be improved beyond 0.5 by employing methods such as the use of ancillary photons [44, 45]. The performance of the scheme employing ancillary photons has been quantified and compared to conventional Bell state measurements [265], and its feasibility has been experimentally demonstrated [46]. The efficiency can approach unity by utilizing increasingly complex ancillary states. However, this comes at the cost of elevated apparatus complexity, a higher likelihood of component errors, and the need for multi-photon detection, all of which restrict their practical application.

The efficiency and fidelity of the IB entanglement generation scheme can be calculated

employing the photon-count decomposition method [259] where the density operator solution of the master equation is decomposed into a set of conditional propagation superoperators dependent on the cumulative detector photon count.

While this gate scheme does not inherently require a cavity for operation, its fidelity rapidly decreases with increasing detection time in the absence of a cavity, and the efficiency becomes too low. We show that incorporating a cavity significantly enhances both the efficiency and fidelity. Each system can be placed in a separate optical cavity, with only the transition $|\downarrow\rangle \leftrightarrow |e\rangle$ coupled to the cavity mode.

When the gate time approaches or exceeds the spin coherence time, spin decoherence begins to affect the system. Since we use the electron spin in single T centers, the dominant spin decoherence comes from spin dephasing, the rate of which is four orders of magnitude larger than that of spin decay, as shown in figure 5.1 **c**. In this case, we can consider only the effect of spin dephasing to quantify the efficiency and fidelity. The efficiency of the IB scheme employing the cavity is given by

$$\eta_{\mathrm{IB}} = \frac{\eta'^2}{2}(1 - e^{-T_d\gamma'})^2 \tag{5.1}$$

where γ' is the Purcell enhanced optical decay rate, the term $e^{-T_d\gamma'}$ describes the probability of the T center remaining in its excited state after a time T_d, and η' is

$$\eta' = \eta_d\,\eta_c\,\frac{F_p\gamma_{zpl}}{\gamma'}. \tag{5.2}$$

In this expression, η_d and η_c represent the detection and collection efficiencies, respectively. The zero-phonon line (ZPL) emission rate is given by $\gamma_{zpl} = \gamma_r\eta_{zpl}$, where the ZPL efficiency (η_{zpl})—also known as the Debye-Waller factor—is the fraction of total emission occurring in the ZPL. For T centers, this value is $\eta_{zpl} = 0.23$ [91]. The radiative decay rate γ_r can be expressed as $\gamma_r = \eta_r\gamma$, where $\gamma = 1/T_{1h}$ is the optical decay rate between $|e\rangle$ and $|\uparrow\rangle$, and η_r is the radiative efficiency. While the exact value of η_r is not yet precisely known,

[92] established a lower bound of $\eta_r \geq 0.23$ for an individual T center, and, for all gate performance evaluations, we assume $\eta_r = 0.23$. The Purcell factor, F_p, describes the ZPL cavity enhancement. Due to the significant presence of phonon sidebands in T centers, the modified decay rate in a cavity with Purcell enhancement is given by $\gamma' = F_p\gamma_{zpl} + \gamma$. The term $\frac{F_p\gamma_{zpl}}{\gamma'}$ in the equation (5.2) is the photon emission efficiency from the cavity mode (η_{em}) in the bad cavity regime with $\gamma \ll \kappa$ [266, 252]. Recently, a value of $\gamma' = 2\pi \times 2.5\,\mathrm{MHz}$ was achieved experimentally by incorporating individual T centers into an optical cavity on a photonic chip [93], resulting in an emission efficiency of $\eta_{em} = 0.93$ for a cavity-coupled single T center.

The fidelity of the IB entanglement generation scheme within the cavity is calculated as

$$F_{\mathrm{IB}} = \frac{1}{2}\left(1 + \frac{(\tilde{C}_{\mathrm{IB}}(T_d))^2}{(1 - e^{-\gamma' T_d})^2}\right), \tag{5.3}$$

with

$$\tilde{C}_{\mathrm{IB}}(T_d) = \frac{\gamma'}{\Gamma' + \gamma_s^*} e^{-2\gamma_s^* \delta t}(1 - e^{-(\Gamma' + \gamma_s^*)T_d}). \tag{5.4}$$

$\Gamma' = \gamma' + 2\gamma^*$ represents the FWHM of the Purcell-enhanced emission line, where $\gamma^* = 1/T_{2h} - \gamma/2$ is the optical pure dephasing rate, and $\gamma_s^* = 1/T_{2e} - 1/2T_{1e}$ is the spin dephasing rate. δt is the time for the spin flip.

Since we consider a local gate, we assume no delay in detection in both rounds, meaning the time window between emission and detection is set to zero (see Section 5.3.2 for more details).

We evaluate the performance of the IB scheme in two main scenarios. Scenario 1 uses the currently demonstrated experimental values for the Purcell-enhanced optical decay rate $\gamma' = 2\pi \times 2.5\,\mathrm{MHz}$ and Purcell factor $F_p = 256.5$ [92, 93, 202] while scenario 2 considers the more optimistic values of $\gamma' = 2\pi \times 12.7\,\mathrm{MHz}$ [267] and $F_p = 1402.4$ that are thought to be attainable experimentally in the near future. Note the $\gamma' = 2\pi \times 12.7\,\mathrm{MHz}$ is based on the estimation of Purcell enhanced emission rate in T center device [267]. Given that a collection

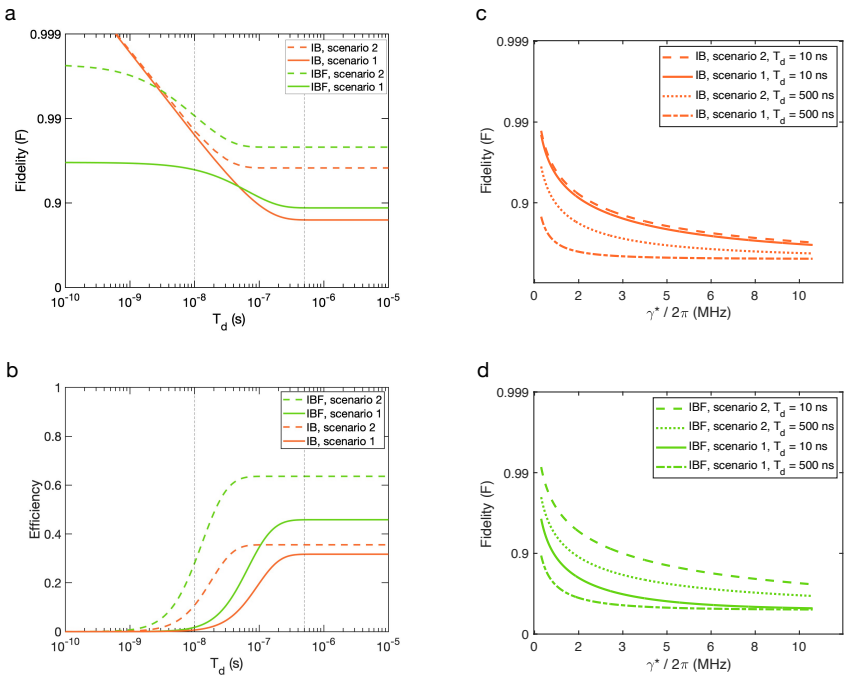

Figure 5.2: The figure compares the fidelity and efficiency of the IB and IBF schemes across different scenarios as a function of detection time T_d (**a** and **b**), and shows the fidelity of the schemes as a function of the optical dephasing rate γ^* (**c** and **d**). Each color corresponds to a certain scheme. Scenario 1 uses the currently demonstrated experimental values for the Purcell-enhanced optical decay rate $\gamma' = 2\pi \times 2.5\,\text{MHz}$, Purcell factor $F_p = 256.5$, and delay time $\delta t = 20.9\,\text{ns}$, whereas scenario 2 considers the more optimistic values of $\gamma' = 2\pi \times 12.7\,\text{MHz}$, $F_p = 1402.4$, and $\delta t = 1.4\,\text{ns}$. Optical dephasing is set to the bulk value in both cases [150]. In **(c)** and **(d)**, the γ^* extends from the optimal value achieved in bulk [150] to the value measured in device [93]. For both the IB and IBF schemes, the results are shown at two detection times, indicated by the vertical dashed lines in **(a)** and **(b)** (see the discussion in section 5.3).

efficiency of $\eta_c = 0.7$ has been achieved for a T center in a silicon nanobeam waveguide [268], we assume $\eta_c = 0.9$ for all gate performance evaluations within the cavity. The detection efficiency is assumed to be $\eta_d = 0.95$, which is achievable with current technology, as similar or higher values have been demonstrated for nearby wavelengths using superconducting nanowire single-photon detectors (SNSPDs) [269, 270, 271]. The fidelity and efficiency of the IB entanglement generation scheme employing a cavity for both scenarios are shown in figure 5.2 (**a** and **b**). As anticipated, achieving the optimistic values leads to notable enhancements in both fidelity and efficiency. These results will be discussed in more detail

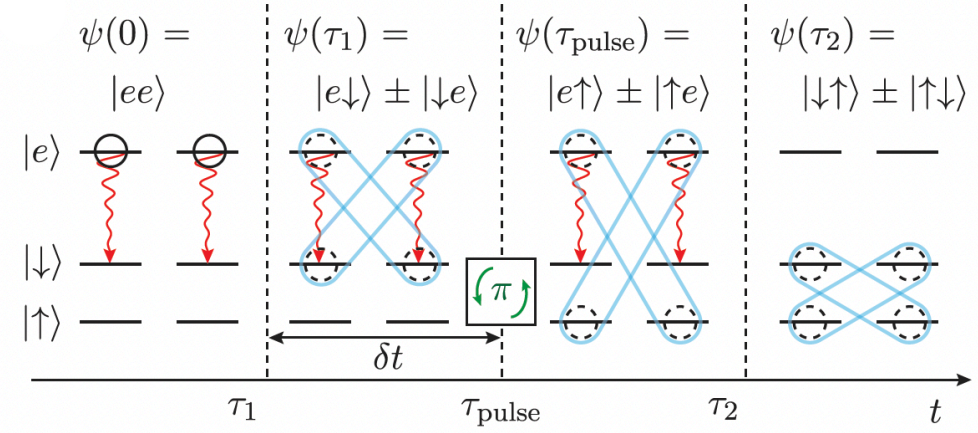

Figure 5.3: Schematic illustration of the implementation of the interference-based scheme with feedback (IBF). Figure from [258]. Permission to include the figure can be found in appendix A.

at the end of the next subsection.

Figure 5.2 **c** shows the fidelity of the IB scheme as a function of the optical dephasing rate, ranging from values characteristic of device-integrated T centers [201, 93] to those achieved in bulk ^{28}Si [150]. Both scenarios are included, along with two representative detection times chosen to highlight the trade-off between efficiency and fidelity (see the next subsection for further discussion).

5.3.2 Interference-based scheme with feedback

Here, we consider the interference-based scheme with feedback (IBF), which was originally proposed in [258] as a modified version of the IB scheme. We derive the general analytical efficiency and fidelity equations for this scheme and apply them to T centers to analyze the performance of the scheme. While the scheme is not deterministic in practice, it can achieve an efficiency greater than 0.5, depending on the system's capabilities.

Similar to the IB scheme, two atoms, each with three levels — one excited state $|e\rangle$ and two ground states $|\uparrow\rangle$ and $|\downarrow\rangle$ — are required. Both systems are initialized in their excited state $|e\rangle$ ($\psi_0 = |ee\rangle$). The excited state $|e\rangle$ decays into the state $|\downarrow\rangle$. The spontaneous emissions from both systems are merged at a beam splitter, erasing any information about

which photon originated from which atom. After detecting one photon at τ_1, the state of the system would be $\psi(\tau_1) = (|e\downarrow\rangle \pm |\downarrow e\rangle)/\sqrt{2}$. Then applying a π pulse between the ground states $|\downarrow\rangle$ and $|\uparrow\rangle$, which takes a time δt and is called feedback, results in the state $\psi(\tau_{pulse}) = (|e\uparrow\rangle \pm |\uparrow e\rangle)/\sqrt{2}$ for the system. Detection of the second photon at τ_2 projects the state of the system into the maximally entangled Bell state $\psi(\tau_2) = (|\downarrow\uparrow\rangle \pm |\uparrow\downarrow\rangle)/\sqrt{2}$ (see figure 5.3). Ideally, this scheme can achieve unit efficiency; however, it is constrained by the non-zero time required to perform the feedback and the possibility of the atom decaying before the π-pulse is applied.

As in 5.3.1, embedding individual T centers in the cavity enhances the efficiency and fidelity of the IB scheme. Therefore, we employ the cavity in the IBF scheme, and the cavity is coupled to the transition from $|e\rangle$ to $|\downarrow\rangle$.

Applying the photon-count decomposition method described in [259], one can quantify the entanglement generation efficiency and fidelity of the IBF scheme. Similar to the IB scheme, there are four possible photon counts: $\mathbf{n} = \{\mathbf{n}_l, \mathbf{n}_e\} = \{(1,0),(1,0)\}$, $\{(1,0),(0,1)\}$, $\{(0,1),(1,0)\}$, and $\{(0,1),(0,1)\}$ where $\mathbf{n}_l$ and $\mathbf{n}_e$ stand for the photon count in the early and late detection time window, and each can take two possible outcomes $(1,0),(0,1)$ which correspond to the click in the left detector and the right detector. Thus, the entanglement generation efficiency and fidelity are defined in the following way

$$\eta_{\text{gen}} = \text{Tr}[\hat{\rho}(t_f)] = \sum_{\mathbf{n}} \text{Tr}[\hat{\rho}_{\mathbf{n}}(t_f)] \tag{5.5}$$

$$F_{\text{gen}} = \frac{1}{4}\sum_{\mathbf{n}} \frac{\langle\psi_{\pm}|\,\hat{\rho}_{\mathbf{n}}(t_f)\,|\psi_{\pm}\rangle}{\text{Tr}[\hat{\rho}_{\mathbf{n}}(t_f)]}, \tag{5.6}$$

where we use $|\psi_+\rangle$, when $\mathbf{n} = \{(1,0),(1,0)\},\{(0,1),(0,1)\}$, otherwise we use $|\psi_-\rangle$. The unnormalized conditional state $\hat{\rho}_{\mathbf{n}}(t_f)$ corresponds to the state conditioned on the measurement

outcome at the final protocol time t_f, which is given by

$$\hat{\rho}_{\mathbf{n_e}}(T_d) = \int_0^{T_d} e^{L_c \delta t_d} \mathcal{S}_{\mathbf{n_e}} e^{L_c t_1} \rho_0 \, dt_1, \tag{5.7}$$

$$\hat{\rho}_m = e^{L_c \delta t} \mathcal{X} \hat{\rho}_{\mathbf{n_e}}(T_d), \tag{5.8}$$

$$\hat{\rho}_{\mathbf{n}}(t_f) = \int_{T_d+\delta t}^{t_f} e^{L_c \delta t_d} \mathcal{S}_{\mathbf{n_l}} e^{L_c (t_2 - T_d - \delta t)} \hat{\rho}_m \, dt_2, \tag{5.9}$$

where $\hat{\rho}_{\mathbf{n_e}}(T_d)$ is the conditional state at detection time T_d, ρ_0 is the initial state, and L_c is the Liouville superoperator without containing the collapse operators [259]. $\delta t_d = T_d - t_1 = t_f - t_2$ is the time window between the collapse and detection. Since the gate is local, we set this time window to be zero, i.e., $\delta t_d = 0$. $\hat{\rho}_m$ is the state after the spin-flip with $\mathcal{X}$ representing the superoperator propagator that executes the spin-flip on both systems during δt. $t_f = T_{\mathrm{IBF}} = 2T_d + \delta t$ is the gate time for the IBF scheme. $\mathcal{S}_{\mathbf{n_e}}$ and $\mathcal{S}_{\mathbf{n_l}}$ stand for the collapse operators for the early and late time bin photons.

In the presence of spin dephasing, the efficiency of the IBF scheme is computed as follows

$$\eta_{\mathrm{IBF}} = \eta'^2 e^{-\gamma' \delta t} (1 - e^{-2\gamma' T_d})(1 - e^{-\gamma' T_d}). \tag{5.10}$$

Both the detection time T_d and delay time δt affect the efficiency in the IBF scheme as opposed to the IB scheme which is insensitive to the spin-flip time. In the optical limit $T_d \gg 1/\gamma'$, the efficiency becomes

$$\eta_{\mathrm{IBF}} = \eta'^2 e^{-\gamma' \delta t}. \tag{5.11}$$

The fidelity is given by the following expression

$$F_{\mathrm{IBF}} = \frac{1}{2} \left(1 + \frac{\tilde{C}_{\mathrm{IBF}}(T_d)}{1 - e^{-\gamma' T_d}} \right), \tag{5.12}$$

with

$$\tilde{C}_{\mathrm{IBF}}(T_d) = \frac{\gamma'}{\Gamma' + \gamma_s^*} e^{-\delta t(2\gamma^* + \gamma_s^*)}(1 - e^{-T_d(\Gamma' + \gamma_s^*)}). \tag{5.13}$$

In the absence of spin dephasing, the fidelity of the scheme can be calculated analytically considering the optical frequency difference between the two T centers, and phase errors (see Supplementary Material section 5.7.1).

To evaluate the scheme's performance in analogy with the IB scheme, we examine δt as the time required to perform a spin flip between the ground states, determined by the microwave Rabi frequency ($\delta t = \pi/\Omega$). In Scenario 1, we assume a delay time of $\delta t = 20.9\,\mathrm{ns}$, corresponding to an estimated microwave Rabi frequency of $\Omega = 2\pi \times 23.9\,\mathrm{MHz}$, which is about an order of magnitude larger than the $\Omega = 2\pi \times 2\,\mathrm{MHz}$ reported in [93]. In Scenario 2, we consider a more optimistic delay time of $\delta t = 1.4\,\mathrm{ns}$. Note that by applying the Raman transitions between the ground states [272], one can drive Rabi frequencies limited by the splitting between the ground states, $\Delta_{\uparrow\downarrow}$, with $\delta t = \pi/\Delta_{\uparrow\downarrow}$. Here, the electron spin states serve as the ground states, with $\Delta_{\uparrow\downarrow} = 2\pi \times 2.25\,\mathrm{GHz}$, leading to a delay time of $\delta t = \pi/\Delta_{\uparrow\downarrow} = 0.2\,\mathrm{ns}$.

The fidelity and efficiency of the IBF scheme are shown in figure 5.2 **a** (**b**). We can see that even with the current experimental values for η_d and η_c and the lower bound of η_r, it is possible to achieve efficiencies greater than those attainable by the IB scheme in the same scenario. The fidelity and efficiency can be strongly influenced by different combinations of δt and γ' values, with scenario 2 showing notable improvements in the scheme's performance.

Figure 5.2 **a** shows that for both photon interference-based schemes, in the presence of spin decoherence, the fidelity decreases rapidly until approximately $T_d = 100\,\mathrm{ns}$. It then remains constant and stabilizes for longer T_d. On the other hand, figure 5.2 **b** shows that the efficiency starts at zero and increases rapidly until approximately 500 ns, after which it approaches saturation in both schemes and scenarios. It reaches its maximum value in the so-called optical limit, where $T_d \gg 1/\gamma'$. Notably, the time at which the efficiency approaches its maximum and the fidelity reaches its plateau differs depending on the specific scenario

considered. Thus, there is a trade-off between efficiency and fidelity in photon interference-based schemes. Higher fidelities can be achieved at shorter detection times at the cost of lower efficiencies. Conversely, waiting until approximately 500 ns allows for maximum efficiency but results in lower fidelity. The prioritization of efficiency or fidelity depends on the ultimate goal of the application. In section 5.6, we will discuss the dependence of fidelity and efficiency on the cavity cooperativity at two different detection times.

Figure 5.2 **c** and **d** show the fidelity of the IB and IBF entanglement generation schemes as a function of the optical dephasing rate γ^* for both scenarios and at two representative detection times ($T_d = 10\,\text{ns}$ and $T_d = 500\,\text{ns}$) corresponding to the the efficiency–fidelity trade-off. In both schemes, the there is a uniform decrease in the fidelity with increasing γ^*, as expected due to the detrimental effect of optical dephasing on photon indistinguishability. For a fixed γ^*, shorter detection times yield higher fidelities, in agreement with the above explanations and highlighting the importance of temporal filtering for achieving high fidelities [273, 274]. Scenario 2 also outperforms scenario 1 across all schemes and detection times, with higher fidelities throughout the entire range of γ^*, consistent with the findings in figure 5.2 **a**. For the IB scheme, fidelity drops below 0.9 for $\gamma^* \gtrsim 2\pi \times 2.1\,\text{MHz}$ at short detection times, whereas for the IBF scheme in scenario 2, this limit occurs at a higher γ^* value, while in scenario 1, it occurs at a lower γ^* value. With continued advancements in host materials and fabrication techniques, the optical dephasing times of device-integrated T centers are expected to improve substantially, approaching those achieved in bulk ^{28}Si.

5.4 Near-deterministic photon scattering-based scheme

In this section, we investigate and analyze quantitatively the cavity-assisted photon scattering-based (SB) scheme for implementation in T centers based on the work done in [260, 275].

The cavity-assisted photon scattering-based (SB) scheme was originally proposed by Duan and Kimble [276]. Since then various modifications have been proposed based on

the main proposal for implementation of local [277] and non-local [278] phase-flip gates. Ref. [260] has studied the gate in both the bad-cavity regime and the strong-coupling regime, compared to previous works where only the strong-coupling regime is discussed.

The gate is implemented between two qubits located in a single-sided cavity by reflecting a single photon off the qubit-cavity system and detecting it. Detecting the photon after its reflection from the cavity heralds the gate operation. One needs a system with three levels: two ground states ($|\uparrow\rangle$, $|\downarrow\rangle$) and one excited state ($|e\rangle$). The transition $|\uparrow\rangle \leftrightarrow |e\rangle$ is resonant with the cavity mode. We denote the state of the single-photon pulse, which is resonant with the cavity mode, by $|p\rangle$. If both qubits are in the state $|\downarrow\rangle$, the photon enters the cavity, and reflects from inside the cavity with a global phase flip, resulting in a π-phase shift in the joint state of the qubit-photon system. However, if either or both qubits are in state $|\uparrow\rangle$, the cavity mode is modified due to the atom-cavity coupling. In this case, the photon does not enter the off-resonant cavity and instead reflects off the cavity's out-coupling mirror without any phase shift leading to a controlled-Z (CZ) gate.

The gate time is $T_{SB} = 8\pi\sqrt{2\ln 2}/\sigma_p$, which is twice the FWHM of the photon duration, where σ_p is the spectral standard deviation of the photon with a Gaussian intensity profile.

Incorporating the detection efficiency η_d, the efficiency of performing the gate is given by

$$\eta_{\mathrm{SB}} = \left(1 - \frac{5}{2C} - \frac{(\delta_{\epsilon_A} - \delta_{\epsilon_B})^2}{2\gamma^2 C}\right) \eta_d \tag{5.14}$$

where C is the cavity cooperativity, and $\delta_{\epsilon_A}(\delta_{\epsilon_B})$ denotes the detuning between the optical transition of system A (B) (corresponding to the T centers in our case) and the cavity mode. The term in the expression in parentheses represents the probability that the photon is scattered off the emitters inside the cavity [275], which, in the zero-detuning case, matches the empirical formula for the success probability limited by photon loss due to atomic spontaneous emission, as given in [276, 277]. The fidelity of the gate can be calculated by analyzing the interaction between a single photon and the cavity–qubit system using quantum Langevin

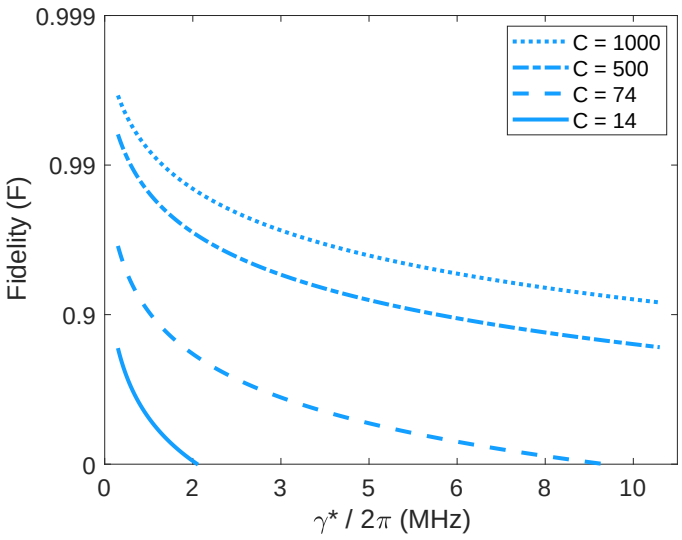

Figure 5.4: Fidelity of the SB scheme as a function of the optical dephasing rate (γ^*) for different values of cavity cooperativity (C). The σ_p value is optimized for each C to maximize the fidelity. Note that the cooperativity values $C = 14$ and $C = 74$ correspond to the two scenarios shown in figure 5.2.

equations, in combination with numerical methods [279, 260, 280]. The fidelity of performing the SB scheme is well approximated by [260, 275]

$$\begin{aligned} F_{\mathrm{SB}} = 1 - \left(\frac{11\gamma^*}{8\gamma C}\right) - \frac{11}{16C^2} - \Gamma T_{\mathrm{SB}} \\ - \frac{\left(-11 + 10\left(\frac{2g}{\kappa}\right)^2\right)\,\delta_p\left(\delta_{\epsilon_A} + \delta_{\epsilon_B}\right)}{4\gamma^2 C^2} \\ - \frac{41\delta_{\epsilon_A}^2 - 38\delta_{\epsilon_A}\delta_{\epsilon_B} + 41\delta_{\epsilon_B}^2}{16\gamma^2 C^2} \\ - \frac{\left(11 - 20\left(\frac{2g}{\kappa}\right)^2 + 12\left(\frac{2g}{\kappa}\right)^4\right)\left(\delta_p^2 + \sigma_p^2\right)}{4\gamma^2 C^2} \end{aligned} \tag{5.15}$$

where g represents the cavity coupling strength, κ is the decay rate of the cavity, δ_p is the mean cavity-photon detuning, and $\Gamma = 1/T_{2e}$ is the effective decoherence rate for the ground state (the electron spin states).

As expected, increasing the cooperativity C while keeping other parameters constant results in higher fidelities. In contrast, increasing δ_p, δ_{ϵ_A}, δ_{ϵ_B} (which can arise from spectral

diffusion in the system), or the ratio $\frac{\gamma^*}{\gamma}$ leads to a reduction in fidelity. Considering that $T_{SB} \propto 1/\sigma_p$, there is a trade-off between the errors arising from the fourth and seventh terms. By optimization of the fidelity with respect to σ_p one can see what value of the spectral standard deviation of the photon σ_p leads to the maximum fidelity for each cavity cooperativity C. The optimized σ_p is

$$\sigma_p = 2 \sqrt[3]{\frac{4\pi\sqrt{2\ln 2}\,\Gamma\gamma^2 C^2}{\left[11 - 20\left(\frac{2g}{\kappa}\right)^2 + 12\left(\frac{2g}{\kappa}\right)^4\right]}}. \tag{5.16}$$

Using the experimental values $g = 2\pi \times 42.4\,\mathrm{MHz}$ and $\kappa = 2\pi \times 5.22\,\mathrm{GHz}$ from [92], which yield a ratio of $g/\kappa = 0.008$, and assuming zero detuning between T centers and the cavity mode ($\delta_{\epsilon_A} = \delta_{\epsilon_B} = 0$), figure 5.4 illustrates the fidelity of the SB gate as a function of the γ^*, evaluated for various cavity cooperativity values (C). For each C, the value of σ_p is optimized to achieve the maximum fidelity. The considered γ^* values for T centers span from the values achieved in bulk [150] to those measured in device-integrated implementations [93]. As expected, increasing γ^* leads to a decrease in fidelity, highlighting the detrimental effect of optical dephasing on gate performance. Higher cooperativity values consistently result in higher fidelities across the considered range of γ^*. For example, with $C = 1000$, the fidelity remains above 0.99 even at moderate dephasing rates, whereas for $C = 14$, it drops sharply and becomes very low at the same γ^* values.

We explored two additional cavity-based schemes: the simple virtual photon exchange scheme and the Raman virtual photon exchange scheme, with details provided in the Supplementary Material (see sections 5.7.4 and 5.7.5). However, these schemes appear to be less promising for T centers in the near and medium term compared to the SB scheme.

5.5 Deterministic magnetic dipole-based scheme

By leveraging the magnetic dipolar interaction between two nearby T centers, a two-qubit quantum gate can be implemented. We adapt the approach from Ref. [250], originally proposed for rare-earth ions, to T centers based on the analysis in Ref. [261]. In this proposal, the "passive" qubits store quantum information, while the "active" qubits, which possess a magnetic moment, interact magnetically to perform a two-qubit phase gate [250]. We begin by initializing the T centers in the lowest hyperfine level of the ground state, then apply a $\pi/2$ microwave pulse to create a superposition of the states (passive qubits). The passive qubits are activated by applying two π pulses to each system, transferring them to the active qubits. An Ising-type spin-spin interaction between the active qubits naturally introduces a phase shift, based on their states, through the unitary time evolution operator $U_{Ising} = e^{i(\pi/4)\sigma_Z^1\sigma_Z^2}$ [281]. Subsequently, the active qubits are returned to the passive qubits by applying another set of π pulses. By applying the Ising-type interaction in combination with single-qubit gates, one can realize a CZ gate [261], a controlled-phase (CPhase) gate [281], or a CNOT gate [281, 282, 250, 261]. The total gate time for the magnetic dipole

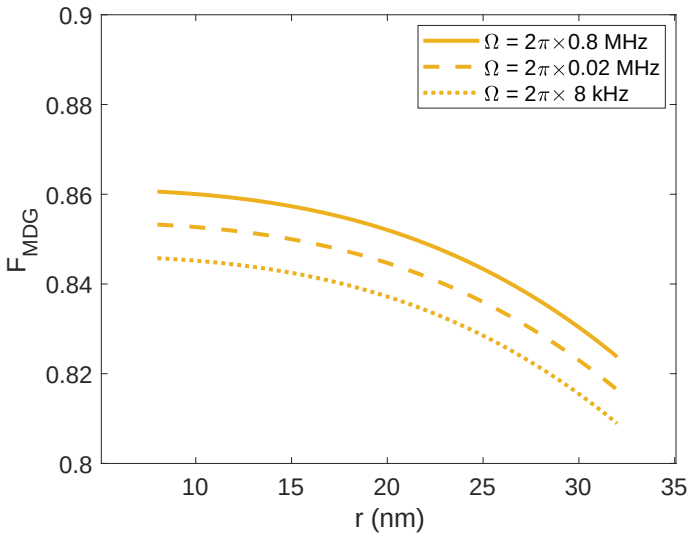

Figure 5.5: Fidelity of performing the magnetic dipole gate between ground states as a function of the distance (r) between two T centers, shown for different Rabi frequencies (Ω) affecting the infidelity from unwanted detuned transitions (see text for more detail).

gate is $T_{MD} = 2T_{act} + T_{int}$ where the first term $T_{act} = \pi/\Omega$ is the time to excite from passive to active qubits and bring them back to the passive qubits. Ω is the Rabi frequency for $|0\rangle_{passive}$ to $|0\rangle_{active}$ and $|1\rangle_{passive}$ to $|1\rangle_{active}$ transitions. The second term $T_{int} = \hbar\pi/4J_z$ is the time to perform the Ising interaction between two active qubits in the excited states, with the dipolar coupling strength $J_z = \frac{\mu_0(\mu_B g_z)^2}{8\pi r^3}$ [250, 261], where μ_0 is the permeability of free space, μ_B is the electron Bohr magneton, and g_z is the principal value of the g-tensor of the excited state (hole spin). Applying tools from time-dependent perturbation theory that includes solving the Schrödinger equation to determine the ideal gate evolution and calculating the lowest-order error expressions, the fidelity of the gate is [261]

$$F_{\mathrm{MD}} = 1 - t_{act}[\frac{7}{8}(\gamma_{1\uparrow} + \gamma_{1\downarrow}) + \frac{13}{16}(\gamma_2 + \gamma_3) + \frac{1}{2}(\gamma_4 + \gamma_5)] - t_{int}[\gamma_{1\uparrow} + \gamma_{1\downarrow} + \frac{3}{4}\gamma_3 + \frac{1}{2}\gamma_5] - a\frac{(J_x + J_y)^2}{J_z^2} \quad (5.17)$$

where $\gamma_{1\uparrow}(\gamma_{1\downarrow})$ is the decay rate for transition $|0\rangle_{active}$ to $|0\rangle_{passive}$ ($|1\rangle_{active}$ to $|1\rangle_{passive}$), γ_2 (γ_3) is the spin decay rate of the passive (active) qubits, γ_4 (γ_5) is the spin dephasing rate of the passive (active) qubits. There is a second order term in equation (5.17) with the coefficient $a = [32\,(2 - \sqrt{2}) - \pi^2]/64$ and $J_\alpha = \frac{\mu_0(\mu_B g_\alpha)^2}{16\pi r^3}$ ($\alpha = x, y$) being the transverse components of the Ising-based interaction [261]. Assuming $g_x = g_y \equiv g_\perp$ and $g_z \equiv g_\parallel$, we investigate two choices of passive and active qubits, evaluating the resulting gate time and fidelity.

Here, we present the results for performing the magnetic dipole gate in the ground state levels (MDG) of the T center. In figure 5.1 **b**, levels $|1\rangle$ and $|2\rangle$ are chosen as passive qubits, while levels $|1\rangle$ and $|4\rangle$ are the active qubits. Thus, level $|1\rangle$ is common to both the passive and active qubit definitions. To have a strong enough magnetic dipole interaction the two excited states should have different electron spins as the nuclear magneton μ_N is much smaller compared to the Bohr magneton μ_B.

The electron spin g_e tensor is treated as isotropic here, although experimental evidence

suggests a minor anisotropy at the 10^{-3} level [283]. Assuming $g_x = g_y = g_z = 2.01$ [283, 91], and a branching ratio of 90% for the $\mathrm{MW}_{\Downarrow}$ transition and 10% for the forbidden $\mathrm{X_m}$ transition, figure 5.5 shows the fidelity F_{MDG} of implementing the magnetic dipole gate between ground-state levels as a function of the distance r between two T centers and for different Rabi frequencies (Ω). The applied Rabi frequency Ω should be smaller than the splitting between the nuclear spins of the $|{\downarrow_e}\rangle$ to ensure the correct level is addressed. The authors in Ref. [250] quantified the infidelity arising from unwanted detuned transitions while performing π pulses as $(\frac{\pi}{2})^2 \exp[-\frac{\pi}{2}(\frac{\Delta_n}{\Omega})^2]$. For a splitting of $\Delta_n = 2\pi \times 2.1\,\mathrm{MHz}$ [188], choosing $\Delta_n/\Omega \approx 3$ results in an error of approximately 10^{-6} in the fidelity. The fidelity decreases with increasing the separation r due to the weakening of the magnetic dipolar coupling strength over distance. It is moderately sensitive to variations in Ω, with higher Rabi frequencies resulting in an improved gate performance. This highlights the importance of stronger driving fields in compensating for the reduced interaction strength at larger distances.

We investigated two additional deterministic dipole-based schemes: the electric dipole-based gate and the magnetic dipole-based gate in the excited state with the details provided in the Supplementary Material (see sections 5.7.2 and 5.7.3). However, these schemes seem to be less promising for T centers in the near and medium term.

Although performing the gate in the ground state is relatively slow compared to the excited state (see figure 5.9), the total gate time is still much less than the electron spin lifetime of 16 s and the decoherence time of 2.1 ms showing the feasibility of performing the magnetic dipole gate in the T center ground state.

5.6 Gate performance comparison

In this section, we compare the performance of the probabilistic photon-mediated schemes (IB, IBF), the near-deterministic photon scattering-based gate (SB), and the deterministic magnetic dipole-based gate in the ground states (MDG) analyzed here.

First, we evaluate the dependence of the efficiency and fidelity of the probabilistic photon-mediated schemes on the cavity cooperativity C (see figure 5.6 **a** (**b**)). $F_p = \frac{4g^2}{\kappa\gamma_{zpl}}$ [284] and $C = \frac{4g^2}{\kappa\gamma}$ [285, 252] result in $F_p = \frac{C}{\eta_r\,\eta_{zpl}}$, and γ' is given by $\gamma' = \gamma\,(1 + C)$.

Following the discussion in section 5.3, we evaluate the efficiency and fidelity of the IB and IBF schemes at two detection times: $T_d = 10\,\text{ns}$ and $T_d = 500\,\text{ns}$, which corresponds to the trade-off between efficiency and fidelity (see figure 5.2). While the efficiency improves with C for the IB and SB schemes, this is not the case for the IBF scheme, where $\eta_{IBF} = 0$ at sufficiently large C when γ' increases (see equation (5.10)). This occurs because the protocol fails if the second photon is detected before the feedback pulse is completed; thus, rapid decay is undesirable. In the medium term, we focus on the low-to-moderate C regime. For the same detection times (T_d), the IBF scheme outperforms the IB scheme in efficiency at low cooperativities ($C < 50$) across both scenarios. In the moderate cooperativity regime, the efficiency of IBF with $\delta t = 1.4\,\text{ns}$ exceeds that of the IB scheme. Note that it is still possible to achieve high efficiencies at large C if delay times shorter than $\delta t = 1.4\,\text{ns}$ can be realized, using techniques such as Raman transitions employed in [272] to achieve fast Rabi oscillations. In practice, implementing feedforward requires more than just the spin-flip operation time; it also involves processing photon detection events and triggering pulses [286]. The SB gate provides the best efficiency scaling with C compared to probabilistic schemes. However, at low and moderate C, the probabilistic IB and IBF schemes offer higher fidelities than the SB scheme. Among them, IBF ($\delta t = 1.4\,\text{ns}$) at $T_d = 10\,\text{ns}$ yields the highest fidelity.

Considering the impact of optical dephasing on the performance of the schemes, figure 5.7 shows a comparison of the fidelities of the IB, IBF, and SB schemes as a function of γ^* under scenario 2 parameters. As the γ^* increases, the fidelity of all schemes decreases that reflects the detrimental impact of optical dephasing. Among the schemes, IBF with a short detection time ($T_d = 10\,\text{ns}$) achieves the highest fidelity and exhibits the greatest robustness against optical dephasing. In contrast, the SB scheme shows the lowest fidelities across the entire range of γ^*. For both IB and IBF, increasing the detection time from 10 ns

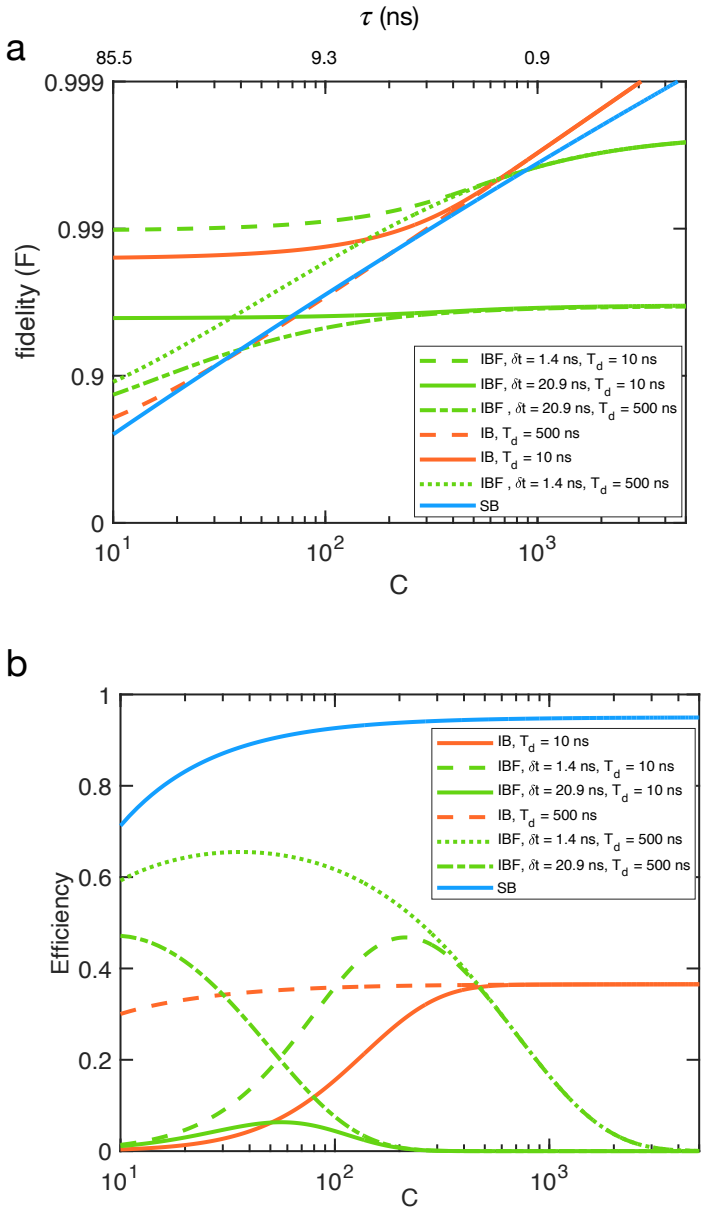

Figure 5.6: A comparison of the **(a)** fidelity and **(b)** efficiency of the probabilistic and near-deterministic photon-mediated gates (IB, IBF, and SB), with respect to the cavity cooperativity C. The enhanced emitter lifetimes (τ) corresponding to the values of C are labeled along the top axis of figure **(a)**. The fidelity of the SB scheme is calculated using the optimized value of σ_p for each C value. The delay time values δt correspond to the scenarios shown in figure 5.2, but with varying C (and therefore γ' and F_p). For the IB and IBF schemes, the results are shown at two detection times, as presented in figure 5.2.

to 500 ns leads to a notable reduction in fidelity, consistent with the results shown in figure 5.2, highlighting the importance of temporal filtering enabled by fast detection in mitigating

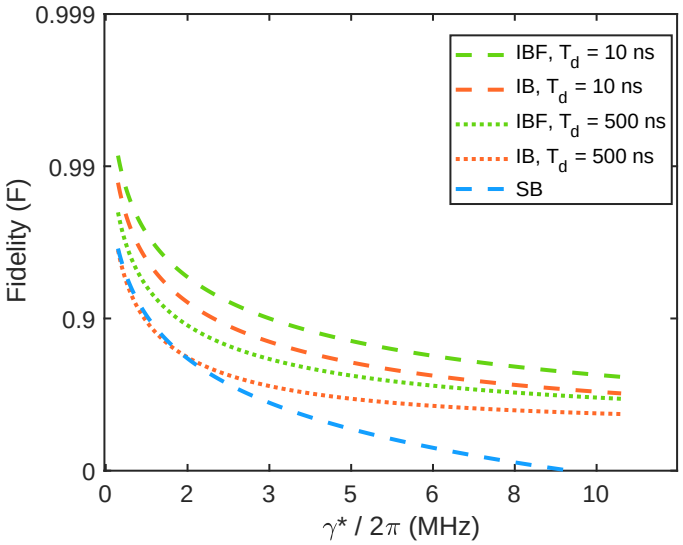

Figure 5.7: A comparison of the fidelity of probabilistic and near-deterministic photon-mediated gates (IB, IBF, and SB) as a function of the optical dephasing rate (γ^*). The γ^* range spans from the best achievable value, found in bulk, to the value observed in device. For all the mentioned schemes, scenario 2 is shown, which means that for the IB and IBF schemes, the parameters used are the enhanced optical decay rate $\gamma' = 2\pi \times 12.7\,\text{MHz}$, Purcell factor $F_p = 1402.4$, and delay time $\delta t = 1.4\,\text{ns}$ (see figure 5.2). For the SB scheme, the cooperativity value $C = 74$ is used, corresponding to the γ' value of the scenario 2. For the IB and IBF schemes, the results are shown at two detection times, as presented in figure 5.2.

optical dephasing effect [274].

Figure 5.8 **a** (**b**) shows the fidelity (efficiency) as a function of gate time T_{gate} for all the gates investigated in sections 5.3, 5.4, and 5.5. For the MDG scheme, fidelity and T_{gate} are expressed as functions of the distance (r) between two T centers (see figure 5.9 for corresponding plots). While MDG fidelity decreases with increasing gate time, SB fidelity initially rises before declining after reaching a maximum, reflecting a trade-off between the fourth and seventh terms in the fidelity equation (equation (5.15)). The fidelity of probabilistic photon-mediated gates follows the same trend as their dependence on detection time T_d, with a plateau at longer gate times (see section 5.3 for the relationship between T_{gate} and T_d, and figure 5.2 for a comparison). Excluding very short gate times, the IBF scheme consistently achieves higher fidelities than the IB scheme in each scenario.

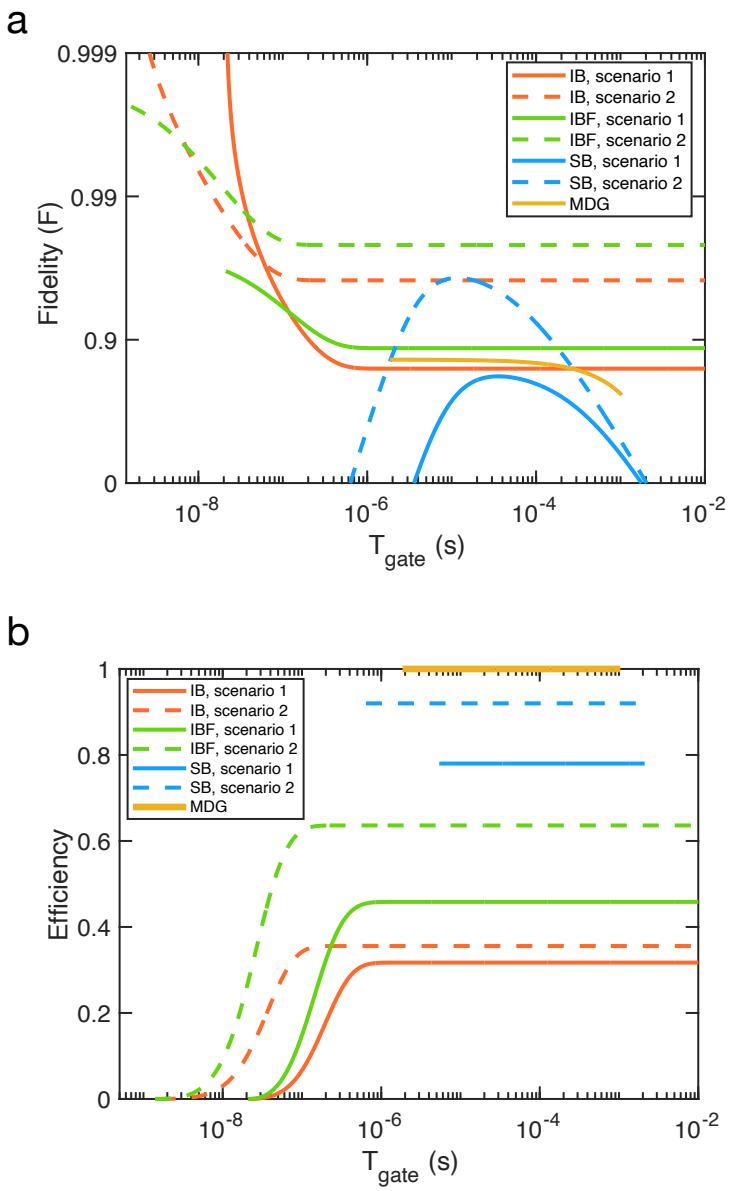

Figure 5.8: Figure shows **(a)** the fidelity (F), and **(b)** efficiency with respect to the gate time T_{gate} for all the gates in sections 5.3, 5.4, and 5.5. Each color corresponds to a certain gate. Scenario 1 uses the currently demonstrated experimental values of the enhanced optical decay rate $\gamma' = 2\pi \times 2.5\,\text{MHz}$, Purcell factor $F_p = 256.5$, and delay time $\delta t = 20.9\,\text{ns}$, whereas scenario 2 considers the more optimistic values of $\gamma' = 2\pi \times 12.7\,\text{MHz}$, $F_p = 1402.4$, and $\delta t = 1.4\,\text{ns}$ (see figure 5.2). For the SB scheme, the change in fidelity and efficiency with respect to T_{gate} is shown for two C values to facilitate better evaluation. These values correspond to the γ' values of the scenarios 1 and 2: $C = 14$ and $C = 74$. Optical dephasing is set to the bulk value in both scenarios [150]. For the MDG scheme, both the fidelity and the gate time T_{gate} are expressed as functions of the distance r, and $\Omega = 2\pi \times 0.8\,\text{MHz}$, which corresponds to the case shown in figure 5.5.

In terms of efficiency versus T_{gate}, the MDG scheme has the advantage of unit efficiency as a deterministic gate. For probabilistic photon-mediated gates, efficiency increases with gate time until it reaches a maximum and plateaus in the optical limit regime. Similar to fidelity, the IBF scheme achieves higher efficiency than the IB scheme in each scenario. As noted in section 5.3, interference-based schemes exhibit a trade-off: fidelity is higher at shorter times, whereas efficiency improves with longer times.

Our findings suggest that, given near and medium-term design and fabrication capabilities, the probabilistic interference-based schemes are the most promising for implementation in T centers. The near-deterministic SB scheme is also favorable at higher cooperativities C or when prioritizing efficiency over fidelity. The MDG scheme offers a high fidelity and deterministic operation, albeit with a slower gate time, if T centers can be positioned in close proximity, similar to other proximity-based gates.

5.7 Conclusion and outlook

In summary, we have investigated various gates between individual T centers in silicon, analyzing and comparing two probabilistic photon interference-based schemes (IB and IBF), a near-deterministic photon scattering-based (SB) scheme, and a deterministic magnetic dipole-based scheme in the ground state (MDG), given current and near-future experimental and technological advancements. The schemes were evaluated using various metrics, including fidelity, efficiency, and gate time, while importantly accounting for practical imperfections in the system and experimental setup.

To enable a meaningful comparison between schemes, we performed a detailed analysis of the photon interference-based scheme with feedback (IBF) and, for the first time, quantified its efficiency and fidelity. We derived new analytical expressions that account for real-world imperfections, including optical decoherence, spin dephasing, photon loss, and inefficiencies in photon collection and detection.

Considering the fabrication technologies for cavities and the creation of T centers in the near and medium term, we conclude that implementing probabilistic photon interference-based schemes is promising. In the near term, while the IB scheme has already been demonstrated [93], the IBF scheme appears particularly attractive, as it simultaneously achieves the highest efficiency and fidelity at low (as observed in current experiments [92, 202]) and moderate values of C, making it a strong candidate for experimental implementation. In the long term, we infer the feasibility of implementing the MDG and SB schemes between T centers.

Considering the requirements for feedforward implementation, cryogenic complementary metal-oxide-semiconductor (cryo-CMOS) technologies have the potential to achieve feedback delays below 10 ns—a threshold that currently represents the experimental limit. However, realizing such low-latency control remains challenging experimentally. The potential for higher efficiency with the IBF scheme further motivates the development of feedback systems capable of operating within this sub-10 ns regime.

The results in this paper assume that spectral diffusion (SD) can be controlled, though mitigating its impact remains challenging. Several works have addressed this issue [287, 288, 289], including time-filtering techniques [93] and resonance-check methods [273, 290], which have been shown to reduce linewidth by up to 35× in T center devices [273]. However, intrinsic spectral mismatch and almost lifetime-limited homogeneous linewidths constrain the achievable spectral alignment between T centers. Active tuning strategies, such as electric field tuning, have also been explored to mitigate these mismatches [283]. Moreover, SD in T centers has been observed to depend on excitation power, with entanglement pulses capable of inducing spectral shifts [273]. This suggests schemes less dependent on excitation lasers may be more resilient to SD. To account for these effects in modeling, a common approach is to average fidelity over a bivariate Gaussian distribution representing emission fluctuations [259, 274]. While this approach captures the effects of spectral diffusion statistically, it does not account for the excitation-power-dependent nature of the shifts. A more refined

approach for modeling can be to consider SD as a time-dependent function, relating fidelity to pulse sequence characteristics and excitation-induced frequency shifts.

It is worth noting that the efficiency presented here is based on an absolute time-bin filter, in which only photons detected within a fixed time window after excitation are considered. While this approach can be advantageous—since spectral diffusion has had minimal time to affect the emitter's frequency during early emission—it may underestimate the achievable efficiency compared to the more commonly used correlation filter [93]. In a correlation filter, photons are selected based on their relative detection times; that is, they are accepted if their arrival times differ by less than a specified time window. This method captures additional successful events, such as photons emitted at later times but still within the accepted temporal correlation, so increasing the overall success probability. Although correlation filtering might not be immediately compatible with the IBF scheme due to the feedforward control, it remains an open question whether a similar filtering strategy could be adapted to IBF, which is worth investigating experimentally. Nevertheless, in the short-lifetime regime—where photon indistinguishability is highest—the difference between these filtering methods becomes less significant, and absolute filtering may even be advantageous due to suppression of the effects of SD by favoring early emission events.

Given the promising outcomes of the probabilistic photon-mediated interference-based schemes for single T centers, one could also investigate the feasibility of other probabilistic interference-based schemes, such as single-photon detection and polarization-based schemes [15, 259, 48].

Since the analytical equations for efficiency and fidelity obtained here can be applied to other systems, and given that the IBF scheme achieves competitive fidelity and efficiency compared to the IB scheme in T centers, one can explore the implementation of this scheme and compare the performance of the schemes discussed here—and in the Supplementary Material—across other solid-state quantum systems. These include various color centers such as those found in diamond (e.g., NV and Si-V centers), as well as rare-earth-ion-doped

crystals. Inherent system properties, such as optical decay and decoherence rates, as well as technological considerations—including the feasibility of system creation, spatial localization of defects, and achievable cavity coupling—would be key factors in determining the most promising gates for each system.

Because the IBF scheme is sensitive to the feedback delay time δt, it is best suited for performing local gates, i.e., between modules in close physical proximity [258], rather than for communication over extended distances (specifically in T centers). However, depending on the physical system employed, the requirement for short feedback delay times can be relaxed, reducing the difficulty of implementing feedforward control. For example, $Er^{3+} : Y_2SiO_5$ is a promising solid-state platform with emission in the telecommunication band and a millisecond-scale excited-state lifetime (on the order of 10 ms) [291], allowing larger values of δt and enabling feedback between more distant nodes with looser constraints on feedforward control.

Other potential next steps could include investigating the feasibility of implementing quantum repeaters with single T centers, as has already been explored for rare-earth ions [292, 252] and NV centers [293, 294]. Additionally, the potential for distributed quantum computing (DQC) based on these various gates could be investigated [295, 8]. In particular, DQC has been explored using the IB scheme in recent work [93], discussed in roadmaps [193], and remains an active area of research.

Acknowledgments

We wish to thank Mahsa Karimi for useful discussions and acknowledge support from the NSERC Alliance Quantum Consortia Grants ARAQNE and QUINT, and the NRC CSTIP Challenge Program on High-Throughput Secure Networks (HTSN).

Supplementary material

5.7.1 SI: Interference-based scheme with feedback, including the effect of optical frequency mismatch and phase errors

If the gate time is significantly shorter than the spin coherence time, the effect of spin decoherence can be neglected and the fidelity of the scheme can be calculated analytically considering the optical frequency difference between the two T centers, and phase errors. The fidelity of the IBF scheme is given by

$$F_{\mathrm{IBF}} = \frac{1}{2}\left(1 + \frac{\Re(\tilde{C}(T_d))}{1 - e^{-\gamma' T_d}}\right), \tag{5.18}$$

where $\Re(\tilde{C}(T_d))$ is the real part of the concurrence $\tilde{C}(T_d)$ that is

$$\tilde{C}(T_d) = \frac{\gamma'}{\Gamma' + i\Delta} e^{-\delta t(2\gamma^* + i\Delta)}(1 - e^{-T_d(\Gamma' + i\Delta)}) e^{i(\varphi+\phi)}. \tag{5.19}$$

Here $\Gamma' = \gamma' + 2\gamma^*$ represents the FWHM of the Purcell-enhanced emission line, γ^* is the optical pure dephasing rate which is $\gamma^* = 1/T_{2h} - \gamma/2$, Δ is the optical frequency difference between the two T centers, $\varphi = \varphi_1 - \varphi_2$ is the relative initialization phase, and $\phi = \phi_1 - \phi_2$ is the relative propagation phase [259]. Infidelity arises from optical decay and dephasing rates, frequency mismatch between the two T centers, and phase errors, all of which affect photon indistinguishability, as captured by the concurrence $\tilde{C}(T_d)$. In the presence of spin dephasing, and assuming there is no spectral detuning $\Delta = 0$ and relative initial phases $\varphi = \phi = 0$ between the T centers, the fidelity of the scheme can be calculated analytically as shown in the main text.

5.7.2 SII: Electric dipole gate

Electric dipole (ED) based gates have been investigated in rare-earth-ion-doped crystals [251], and here we adapt this approach for the T center. The lack of site symmetry leads the color centers belonging to some crystallographic point groups to have a permanent electric dipole moment, which changes when a T center is excited from the ground state to the TX_0 excited state. The transition frequency of the nearby individual T center is affected by the modification in the environmental electric field which is the result of changing in the permanent electric dipole moment of the neighbouring T center excitation. Therefore, by optical excitation of the T center one can control the shift in the transition frequency of the neighbouring center and perform a controlled-NOT (CNOT) operation between nearby T centers. The required pulse sequences and how to perform the gate are detailed in [251]. The change in the transition frequency ($\Delta\nu$) of the nearby T center is estimated by [251, 292]

$$\Delta\nu = \frac{\Delta\mu_T \Delta\mu_T}{4\pi\epsilon\epsilon_0 h r^3} \left((\hat{\mu}_T \cdot \hat{\mu}_T) - 3(\hat{\mu}_T \cdot \hat{r})(\hat{\mu}_T \cdot \hat{r})\right) \tag{5.20}$$

where $\Delta\mu_T$ is the change in the permanent electric dipole moment of the T center with the measured value of $\Delta\mu_T = 49 \times 10^{-31}\,\mathrm{Cm}$ [283], r is the separation between the two T centers, h and ϵ_0 are the Planck constant and the vacuum permittivity, and ϵ is the dielectric constant. With the refractive index of $n = 3.45$ for silicon, one can calculate the dielectric constant $\epsilon = n^2$. Therefore, $\Delta\nu$ can be obtained for different T centers' separations. The shift in the transition frequency ($\Delta\nu$) should be more than a few homogeneous linewidth which is $\Gamma^{hom}/2\pi = 690\,\mathrm{kHz}$ for the T center [201]. One should note that here we consider only the y-component for the calculation of $\Delta\mu_T$ in equation (6) of [283]. However, if both components are considered, we obtain $\Delta\mu_T = 55 \times 10^{-31}\,\mathrm{Cm}$, corresponding to larger distances between the T centers for similar values of $\Delta\nu$ (see equation (5.20).

To perform the gate we need three levels (see figure 2 in [292]). For T center we can work with the two electron spin levels $|\uparrow_e\rangle$ and $|\downarrow_e\rangle$, and one of the hole spin levels $|\downarrow_h\rangle$ in

figure 5.1 **b**. In total, we apply five pulses with a Rabi frequency of Ω to perform the gate: two pulses on the T center acting as the control qubit (Ω_c) and three pulses on the T center acting as the target qubit (Ω_t) (see figure 2 in [292]). Consequently, the total gate time for the electric dipole gate is given by $T_{ED} = \frac{2\pi}{\Omega_c} + \frac{3\pi}{\Omega_t}$.

For a high-fidelity gate, it is essential to ensure that the frequency shift $\Delta\nu$ is sufficiently large to prevent the lasers from exciting the frequency-shifted T center (the target qubit) while the neighboring T center (the control qubit) is being excited. This requires the condition ${\Omega_t}^2 \ll \Delta\nu^2$. This leads to a very slow gate and a low fidelity because $\Delta\nu$ cannot be arbitrarily large (the distance between T centers cannot be arbitrarily small). To overcome this issue, one can perform an effective 2π pulse on the T center spin state when the nearby T center is excited as suggested in rare-earth-ion-doped crystals [292]. Then $\Omega_t = \Delta\nu/\sqrt{3}$ and $T_{ED} = \frac{2\pi}{\Omega_c} + \frac{3\pi\sqrt{3}}{\Delta\nu}$. Also, to ensure that only one of the electron spin levels is addressed by the applied pulses, Ω should be smaller than the frequency splitting between the electron spin levels. For example for a splitting of $\Delta_e = 2\pi \times 2.25\,\mathrm{GHz}$, a ratio of $\Delta_e/\Omega = 4$ corresponds to an error of 10^{-11} in the fidelity due to unwanted off-resonant excitations (see section 5.5). The fidelity of the electric dipole gate, determined by analytically solving the master equation for a nine-level system (with each T center modeled as a three-level system), is given by [292]

$$F_{\mathrm{ED}} = 1 - \frac{\mathrm{T_{ED}}}{80}(42\gamma + 25\gamma^* + 25\chi) - \frac{43\pi^2}{128}(\frac{\delta\nu}{\Delta\nu})^2 \tag{5.21}$$

where $\gamma = 1/T_{1h}$ is the optical decay rate, γ^* is the optical pure dephasing rate which is $\gamma^* = 1/T_{2h} - \gamma/2$ for the optical transition, $\chi = 1/T_{2e}$ is the electron spin decoherence rate, and $\delta\nu$ is a small error from the true value of $\Delta\nu$.

Figure 5.9 **a** (**b**) shows the fidelity F_{ED} (gate time T_{ED}) with respect to the distance r between the T centers using equations (5.20) and (5.21). Note T_{ED} should be less than the optical lifetime and dephasing time. For reasonable gate times and improved fidelity, $\Delta\nu$ must be increased, i.e., the separation between T centers must be decreased, which is

currently beyond the reach of existing technology. However, if T centers could be created close enough to achieve a sufficiently large $\Delta\nu$, performing this gate would become feasible.

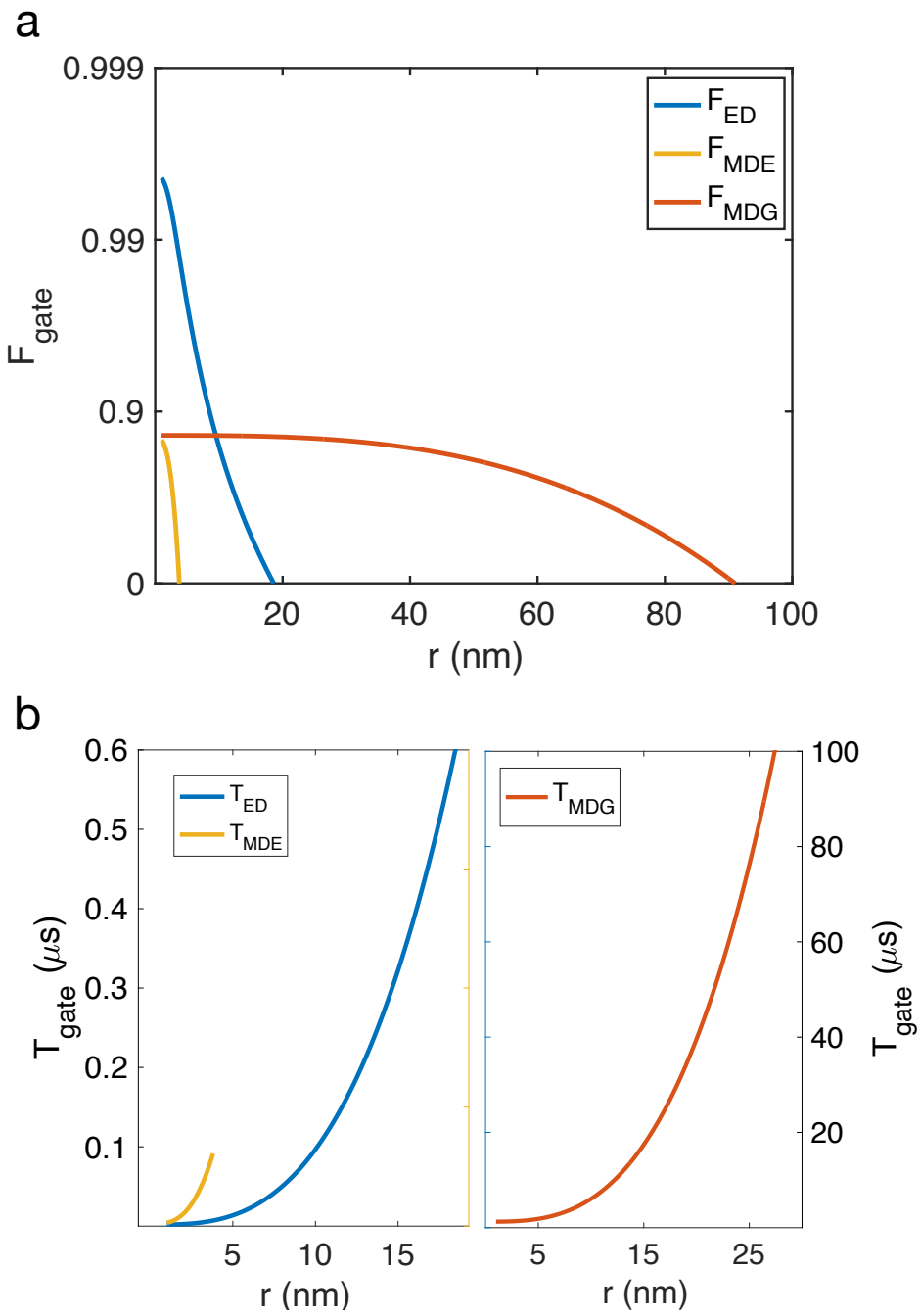

Figure 5.9: Comparison of the **(a)** fidelity (F_{gate}) and **(b)** gate time (T_{gate}) for the electric dipole gate (ED), and the magnetic dipole gate (performing in both the excited (MDE) and ground state (MDG)) with respect to the distance r between the two T centers. For each gate, only the variable ranges that yield meaningful values for fidelity are shown.

5.7.3 SIII: Magnetic dipole gate in the excited states

Here, we consider performing the magnetic dipole gate in the excited states (MDE), selecting the electron spin states in the ground state as the "passive" qubits and the hole spin states in the excited state as the "active" qubits. The anisotropy of the unpaired hole spin in the bound exciton excited state results in 12 independently addressable orientational subsets, meaning each T center would have a specific orientation [91] (see figure 5.1 **b**). We choose the first orientational subset as it has the largest g-value. To calculate the gate time and fidelity, one needs the information about the g-tensor in the excited state, but such information is not available. Assuming $g_x = g_y = g_z = 3.45$ [91] and a decay time of 100 ns between the hole spins up and down, figure 5.9 **a** (**b**) shows the fidelity F_{MDE} (gate time T_{MDE}) of the magnetic dipole gate with respect to the separation between the T centers (see section 5.5 for equations). Note the gate time T_{MDE} should be shorter than the optical decay time, the decoherence time between the excited states (hole spins), and the decoherence time between the ground states. The assumption of $g_x = g_y = g_z$ leads to a second-order error contribution of 0.02 to the fidelity. The infidelity term mentioned in section 5.5, which arises from unwanted off-resonant excitations during the application of π pulses with Rabi frequency Ω, is approximately 10^{-13}. It's important to keep in mind that this result excludes terms involving the excited-state spin dephasing rate γ_5 in the fidelity equation (5.17), as there are no measurements of this parameter for the T center. However, performing this gate in the excited states is generally unattractive, as achieving high fidelity and reasonable gate times would require the distance between the two T centers to be less than 2 nm. Therefore, implementing this gate in the excited state (hole spins) is not feasible with current technology.

5.7.4 SIV: Simple virtual photon exchange

The simple virtual photon exchange scheme (VP) is based on a cavity-assisted interaction between qubits. A phase-flip gate is performed when the two systems' optical transitions are in resonance but dispersively coupled to a cavity mode.

Using the non-Hermitian Hamiltonian approach and solving the effective non-Hermitian component of the master equation yields an analytical expression for the fidelity of the simple virtual photon exchange gate that is well approximated by [260, 252]

$$F_{\mathrm{VP}} = 1 - \frac{2\pi}{\sqrt{C}} - 2\Gamma \mathrm{T}_{\mathrm{VP}} - 0.58 \mathrm{T}_{\mathrm{VP}} \gamma^* - \frac{6\pi^2}{32}\left[\left(\frac{\mathrm{T}_{\mathrm{VP}}\Delta_\epsilon}{2\pi}\right)^2 + \left(\frac{2\pi}{\mathrm{T}_{\mathrm{VP}}\delta_{eg}}\right)^2 - \frac{12}{C}\right] \quad (5.22)$$

where Δ_ϵ is the detuning between the quantum systems' optical transitions which is small, δ_{eg} is the difference between ground-state and excited-state splittings, $\Gamma = 1/2T_{2e}$ is the effective decoherence rate for the ground state, $\gamma^* = 1/T_{2h} - \gamma/2$ is the optical pure dephasing rate, and T_{VP} is the gate time of VP scheme. Here, we consider the optimal gate time using the equation $T_{VP} = 2\pi/\gamma\sqrt{C}$, which is achieved under the condition that maximizes the gate fidelity [260]. In this equation, $\gamma = 1/T_{1h}$ is the optical decay rate, and C is the cavity cooperativity. Note that equation (5.22) includes a factor of 2 in the infidelity terms compared to the fidelity equation in [260], as the fidelity definition used here is the square of the definition used in Ref. [260]. To account for the effect of optical pure dephasing, the analytical approximation is compared with the numerical solution from simulating the master equation in the bad-cavity regime and the coefficient of 0.58 in the third infidelity term is obtained [252]. To achieve high fidelity the gate time T_{VP} must be shorter than the excited state lifetime T_{1h}, and the system should avoid entering the strong-coupling regime $g/\kappa \leq 1$ [260].

Four levels are required to perform the gate. We employ the two electron spin states in the ground state $|\downarrow_e\rangle$, $|\uparrow_e\rangle$ and the two hole spin states in the bound exciton excited state $|\downarrow_h\rangle$, $|\uparrow_h\rangle$ to perform the gate. Figure 5.10 **a** (**b**) shows fidelity F_{VP} (gate time T_{VP}) for VP scheme. The result shows obtaining favorable gate time and fidelity for the VP gate in T centers requires relatively large cavity cooperativity. Considering the current experimental

value for the cavity cooperativity of the T center [92], the largest realistic value for C in the foreseeable future would be around 100. Therefore, this gate would not be suitable for the T center in the near term. With the advent of cavity fabrication technology and increase in the C value this gate might be practicable for implementation on T center.

5.7.5 SV: Raman virtual photon exchange

Raman virtual photon exchange scheme (RVP) is another phase-flip gate between distant qubits that can be performed using virtual excitation of the cavity mode via a Raman coupling. This gate has been implemented on quantum dots and trapped ions. The proposed scheme in [260] helps to overcome the challenges of the previous proposals and also allows one to perform a phase-flip gate between qubits in systems that have unequal optical transitions.

We consider two 4-level systems where the systems are dispersively coupled to a far-detuned cavity. The levels to perform the gate in T centers are the nuclear spins associated with the electron spins in the ground state $|1\rangle$, $|3\rangle$, and $|4\rangle$ for shelving, and hole spin down $|\downarrow_h\rangle$ in the excited state.

The RVP scheme is analyzed similarly to the VP scheme, with the fidelity calculated by solving the master equation using the non-Hermitian Hamiltonian method and is well approximated by [260]

$$F_{\mathrm{RVP}} = 1 - \frac{2\pi}{\sqrt{C}} - 2\Gamma \mathrm{T}_{\mathrm{RVP}} - \frac{\pi^2}{8}\left[\left(\frac{\mathrm{T}_{\mathrm{RVP}}\delta_\epsilon}{2\pi}\right)^2 + \frac{\Delta_\epsilon^2}{\Delta^2} - \frac{18}{C}\right] \quad (5.23)$$

where δ_ϵ is a small two-photon resonance error, Δ is the detuning between the cavity mode and the resonance transition of the quantum system, $\Gamma = 1/2T_{2e}$ is the effective decoherence rate for the ground state, Δ_ϵ is a small detuning between the optical frequencies of the systems, and T_{RVP} is the gate time of RVP scheme. Under the condition that maximizes the

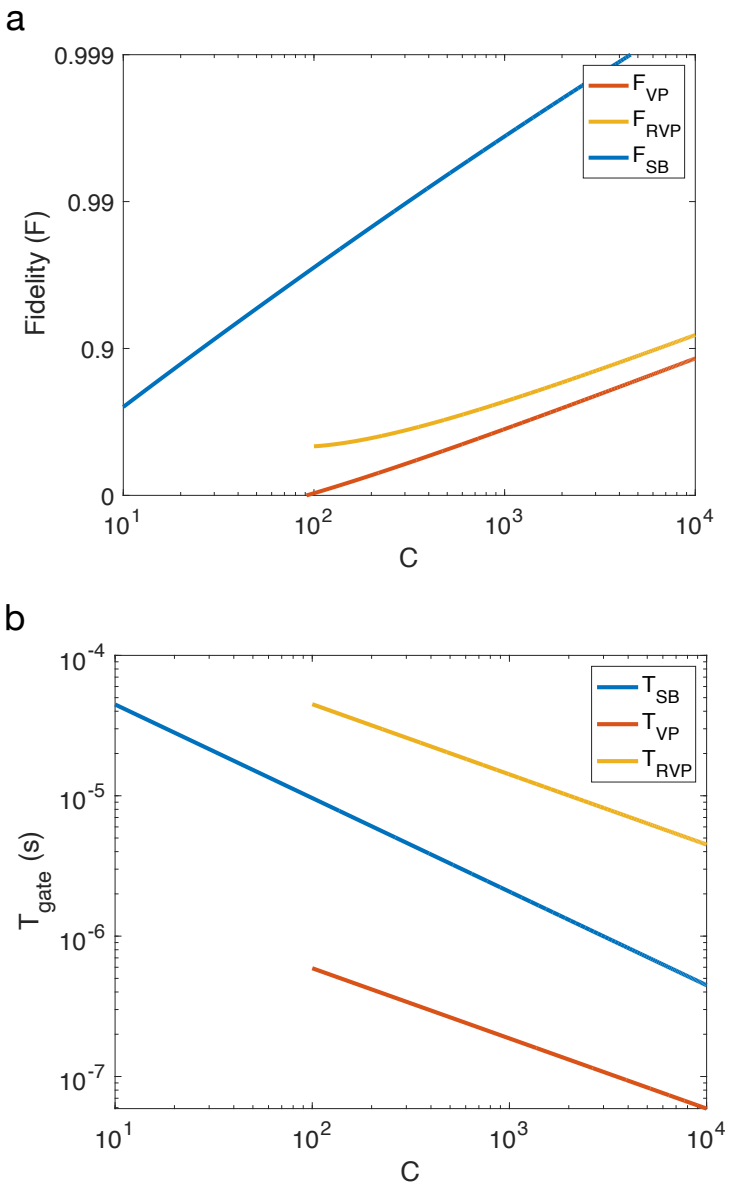

Figure 5.10: Comparison of the **(a)** fidelity (F_{gate}) and **(b)** gate time (T_{gate}) for the photon scattering-based (SB), simple virtual photon exchange (VP), and Raman virtual photon exchange (RVP) schemes with respect to the cavity cooperativity C for implementation in the T center. For the VP scheme, it is assumed that $\Delta_\epsilon = 0$, with the relevant splittings in the ground and excited states for the T center given as $\delta_{eg} = 1.62\,\text{GHz}$. For the RVP scheme, $\Delta_\epsilon = \delta_\epsilon = 0$ and $\Omega = 0.1\Delta$ are assumed. For the SB scheme, we assume $\delta_p = \delta_{\epsilon_A} = \delta_{\epsilon_B} = 0$, with $g/\kappa = 0.01$ based on experimental data [92]. For each gate, only the variable ranges that yield meaningful values for fidelity are shown.

scheme fidelity [260], the optimal gate time is given by $T_{RVP} = (\Delta/\Omega)^2\,(2\pi/\gamma\sqrt{C})$, where Ω is the Rabi frequency of the classical laser field. To achieve high fidelity the gate time T_{RVP}

should be shorter than the lifetime of the shelved state, the system should remain in the bad-cavity regime $g < \kappa$, and $\Omega \ll \Delta$ to avoid populating the excited state. Although in the RVP scheme the excited state is not populated, the fidelity in equation (5.23) represents an upper bound.

To approximately account for the detrimental effect of optical pure dephasing on fidelity, we adopt the approach in Ref. [261], which quantifies this effect by replacing the cavity cooperativity C with an effective cooperativity $C_{eff} = C/[1 + 0.7\,(T_{1h}/T_{2h} - 1)]$ in equation (5.23), indicating that optical pure dephasing effectively reduces the cavity cooperativity. Note that T_{RVP} is also dependent on the cavity cooperativity C, so one should consider the change in T_{RVP} due to optical pure dephasing when calculating the fidelity [252].

Figure 5.10 **a** (**b**) shows F_{RVP} (T_{RVP}) for RVP scheme. Employing the same values of cavity cooperativity C as the VP scheme one can achieve higher fidelity by performing the Raman scheme compared to the simple virtual scheme. However, even for the high cooperativities the time for performing the Raman gate T_{RVP} is much slower. Although a slow gate is a challenge if one wants to integrate the system in a chain of other operations, for Raman virtual gate there is no real excitation of the atoms, and so there is no limitation on the gate time compared to the simple virtual gate where the gate time should be less than the optical decoherence time.

Chapter 6

Conclusion and outlook

Global quantum networks built upon long distance quantum communication, will pave the way for a range of applications including secure communication, distributed quantum computing, and novel fundamental tests of quantum principles. Quantum repeaters, as a key component for enabling long-distance quantum communication, have attracted significant attention over the past two decades. However, their practical implementation remains challenging, as they critically depend on efficient quantum memories and reliable protocols for entanglement generation, storage, and swapping.

This thesis primarily aims to advance realistic elements for quantum networks. Given the promise of AFC memory for quantum repeater applications and the absence of a comprehensive model to describe and predict the performance of cavity-enhanced AFC quantum memories, we began by developing a theoretical framework to address the challenge of characterizing comb properties within the cavity. By incorporating measured cavity reflectivity, the model enables estimation of comb parameters and memory efficiency for memories with background absorption and arbitrary bandwidths detuned from the cavity resonance. The model provides realistic estimates of optical depth and correct efficiency trend, which peaks near resonance. Notably, the predicted efficiencies show semi-quantitative agreement with experimental data, highlighting the critical role of dispersion in accurately modeling cavity-

enhanced AFC quantum memories.

Although extensive efforts have been made toward the realization of quantum memories, a system that fully meets all the required criteria has yet to be achieved. Future quantum memories will likely benefit from a range of protocols and physical platforms, depending on specific user needs. Considering that our developed model is applicable to cavity-enhanced AFC memories based on other REICs, it could be employed to predict performance in a variety of systems. With the recent demonstration of a chip-integrated AFC quantum memory, one promising direction would be to adapt our theoretical model to a cavity incorporating a waveguide crystal instead of a bulk crystal. Another potential avenue is to explore the effect of operating in the regimes other than the impedance-matched weak coupling regime.

Inspired by the recent growing interest in T centers in silicon, we shifted our focus to single-emitter-based systems. In the second project, we explored several quantum gate implementations between individual T centers, evaluating and comparing different schemes including two probabilistic photon interference-based protocols (IB and IBF), a near-deterministic photon scattering-based (SB) approach, and a deterministic gate based on magnetic dipole interactions in the ground state (MDG). These schemes were evaluated in scenarios associated with current and anticipated experimental capabilities, using performance metrics such as fidelity, efficiency, and gate time, while incorporating realistic system imperfections and experimental constraints. We also performed a detailed analysis of the feedback-enhanced interference-based scheme (IBF), quantitatively assessing its fidelity and efficiency while accounting for optical decoherence, spin dephasing, photon loss, and imperfections in photon collection and detection.

There are several promising directions for future research. Building on the encouraging results of probabilistic photon-mediated interference-based schemes with single T centers, one avenue would be to explore the feasibility of alternative probabilistic interference-based protocols. Another direction could be applying the analytical results developed in this work to investigate the implementation of feedback-enhanced interference-based (IBF) scheme

in other solid-state platforms, such as color centers in diamond and rare-earth-ion-doped crystals. Additionally, the feasibility of realizing quantum repeaters using single T centers, similar to prior proposals for NV centers and rare-earth ions can be investigated. Finally, the potential for enabling distributed quantum computing with T centers, leveraging these various gate schemes, presents an exciting opportunity.

Bibliography

[1] Christoph Simon. Towards a global quantum network. *Nature Photonics*, 11(11):678–680, 2017.

[2] Andreas Reiserer. Colloquium: Cavity-enhanced quantum network nodes. *Reviews of Modern Physics*, 94(4):041003, 2022.

[3] Wolfgang Tittel, Mikael Afzelius, Adam Kinos, Lars Rippe, and Andreas Walther. Quantum networks using rare-earth ions. *arXiv preprint arXiv:2501.06110*, 2025.

[4] L-M Duan and Christopher Monroe. Colloquium: Quantum networks with trapped ions. *Reviews of Modern Physics*, 82(2):1209–1224, 2010.

[5] Nicolas Gisin, Grégoire Ribordy, Wolfgang Tittel, and Hugo Zbinden. Quantum cryptography. *Reviews of Modern Physics*, 74(1):145, 2002.

[6] Charles H. Bennett and Gilles Brassard. Quantum cryptography: Public key distribution and coin tossing. In *Proceedings of IEEE International Conference on Computers, Systems and Signal Processing*, pages 175–179. IEEE, 1984.

[7] Stefano Pirandola, Ulrik L Andersen, Leonardo Banchi, Mario Berta, Darius Bunandar, Roger Colbeck, Dirk Englund, Tobias Gehring, Cosmo Lupo, Carlo Ottaviani, et al. Advances in quantum cryptography. *Advances in Optics and Photonics*, 12(4):1012–1236, 2020.

[8] David Barral, F Javier Cardama, Guillermo Díaz-Camacho, Daniel Faílde, Iago F Llovo, Mariamo Mussa-Juane, Jorge Vázquez-Pérez, Juan Villasuso, César Piñeiro, Natalia Costas, et al. Review of distributed quantum computing: from single QPU to high performance quantum computing. *Computer Science Review*, 57:100747, 2025.

[9] David Rideout, Thomas Jennewein, Giovanni Amelino-Camelia, Tommaso F Demarie, Brendon L Higgins, Achim Kempf, Adrian Kent, Raymond Laflamme, Xian Ma, Robert B Mann, et al. Fundamental quantum optics experiments conceivable with satellites—reaching relativistic distances and velocities. *Classical and Quantum Gravity*, 29(22):224011, 2012.

[10] H Jeff Kimble. The quantum internet. *Nature*, 453(7198):1023–1030, 2008.

[11] Stephanie Wehner, David Elkouss, and Ronald Hanson. Quantum internet: A vision for the road ahead. *Science*, 362(6412):eaam9288, 2018.

[12] William K Wootters and Wojciech H Zurek. A single quantum cannot be cloned. *Nature*, 299(5886):802–803, 1982.

[13] Koji Azuma, Sophia E Economou, David Elkouss, Paul Hilaire, Liang Jiang, Hoi-Kwong Lo, and Ilan Tzitrin. Quantum repeaters: From quantum networks to the quantum internet. *Reviews of Modern Physics*, 95(4):045006, 2023.

[14] H-J Briegel, Wolfgang Dür, Juan I Cirac, and Peter Zoller. Quantum repeaters: the role of imperfect local operations in quantum communication. *Physical Review Letters*, 81(26):5932, 1998.

[15] Nicolas Sangouard, Christoph Simon, Hugues De Riedmatten, and Nicolas Gisin. Quantum repeaters based on atomic ensembles and linear optics. *Reviews of Modern Physics*, 83(1):33–80, 2011.

[16] Tian-Xiang Zhu, Xiao Liu, Zong-Quan Zhou, and Chuan-Feng Li. Remote quantum networks based on quantum memories. *Nanophotonics*, 14(11):1975–1992, 2025.

[17] Yisheng Lei, Faezeh Kimiaee Asadi, Tian Zhong, Alex Kuzmich, Christoph Simon, and Mahdi Hosseini. Quantum optical memory for entanglement distribution. *Optica*, 10(11):1511–1528, 2023.

[18] Mikael Afzelius, Christoph Simon, Hugues De Riedmatten, and Nicolas Gisin. Multimode quantum memory based on atomic frequency combs. *Physical Review A—Atomic, Molecular, and Optical Physics*, 79(5):052329, 2009.

[19] Mikael Afzelius and Christoph Simon. Impedance-matched cavity quantum memory. *Physical Review A—Atomic, Molecular, and Optical Physics*, 82(2):022310, 2010.

[20] Sergey A Moiseev, Sergey N Andrianov, and Firdus F Gubaidullin. Efficient multimode quantum memory based on photon echo in an optimal QED cavity. *Physical Review A—Atomic, Molecular, and Optical Physics*, 82(2):022311, 2010.

[21] Michael A Nielsen and Isaac L Chuang. *Quantum computation and quantum information*. Cambridge University Press, 2010.

[22] Thaddeus D Ladd, Fedor Jelezko, Raymond Laflamme, Yasunobu Nakamura, Christopher Monroe, and Jeremy Lloyd O'Brien. Quantum computers. *Nature*, 464(7285):45–53, 2010.

[23] David Elieser Deutsch. Quantum computational networks. *Proceedings of the Royal Society of London. A. mathematical and physical sciences*, 425(1868):73–90, 1989.

[24] L-M Duan, Mikhail D Lukin, J Ignacio Cirac, and Peter Zoller. Long-distance quantum communication with atomic ensembles and linear optics. *Nature*, 414(6862):413–418, 2001.

[25] Erwin Schrödinger. Die gegenwärtige situation in der quantenmechanik. *Naturwissenschaften*, 23(50):844–849, 1935.

[26] DGBJ Dieks. Communication by EPR devices. *Physics Letters A*, 92(6):271–272, 1982.

[27] Heng Fan, Yi-Nan Wang, Li Jing, Jie-Dong Yue, Han-Duo Shi, Yong-Liang Zhang, and Liang-Zhu Mu. Quantum cloning machines and the applications. *Physics Reports*, 544(3):241–322, 2014.

[28] Valerio Scarani, Sofyan Iblisdir, Nicolas Gisin, and Antonio Acín. Quantum cloning. *Reviews of Modern Physics*, 77(4):1225–1256, 2005.

[29] Horace P Yuen. Amplification of quantum states and noiseless photon amplifiers. *Physics Letters A*, 113(8):405–407, 1986.

[30] Howard Barnum, Carlton M Caves, Christopher A Fuchs, Richard Jozsa, and Benjamin Schumacher. Noncommuting mixed states cannot be broadcast. *Physical Review Letters*, 76(15):2818, 1996.

[31] Vladimir Bužek and Mark Hillery. Quantum copying: Beyond the no-cloning theorem. *Physical Review A*, 54(3):1844, 1996.

[32] Erwin Schrödinger. Discussion of probability relations between separated systems. In *Mathematical Proceedings of the Cambridge Philosophical Society*, volume 31, pages 555–563. Cambridge University Press, 1935.

[33] Albert Einstein, Boris Podolsky, and Nathan Rosen. Can quantum-mechanical description of physical reality be considered complete? *Physical Review*, 47(10):777, 1935.

[34] John S Bell. On the Einstein–Podolsky–Rosen paradox. *Physics Physique Fizika*, 1(3):195, 1964.

[35] John F Clauser, Michael A Horne, Abner Shimony, and Richard A Holt. Proposed experiment to test local hidden variable theories. *Physical Review Letters*, 24(10):549, 1970.

[36] Stuart J Freedman and John F Clauser. Experimental test of local hidden-variable theories. *Physical Review Letters*, 28(14):938, 1972.

[37] Alain Aspect, Philippe Grangier, and Gérard Roger. Experimental tests of realistic local theories via Bell's theorem. *Physical Review Letters*, 47(7):460, 1981.

[38] W. Tittel, J. Brendel, H. Zbinden, and N. Gisin. Violation of Bell inequalities by photons more than 10 km apart. *Physical Review Letters*, 81:3563–3566, Oct 1998.

[39] Gregor Weihs, Thomas Jennewein, Christoph Simon, Harald Weinfurter, and Anton Zeilinger. Violation of Bell's inequality under strict einstein locality conditions. *Physical Review Letters*, 81(23):5039, 1998.

[40] Mary A Rowe, David Kielpinski, Volker Meyer, Charles A Sackett, Wayne M Itano, Christopher Monroe, and David J Wineland. Experimental violation of a Bell's inequality with efficient detection. *Nature*, 409(6822):791–794, 2001.

[41] Bas Hensen, Hannes Bernien, Anaïs E Dréau, Andreas Reiserer, Norbert Kalb, Machiel S Blok, Just Ruitenberg, Raymond FL Vermeulen, Raymond N Schouten, Carlos Abellán, et al. Loophole-free Bell inequality violation using electron spins separated by 1.3 kilometres. *Nature*, 526(7575):682–686, 2015.

[42] Faezeh Kimiaee Asadi. *Long-distance quantum communication with single solid-state spins*. Doctoral thesis, University of Calgary, 2020.

[43] Norbert Lütkenhaus, John Calsamiglia, and K-A Suominen. Bell measurements for teleportation. *Physical Review A*, 59(5):3295, 1999.

[44] Warren P Grice. Arbitrarily complete Bell-state measurement using only linear optical elements. *Physical Review A—Atomic, Molecular, and Optical Physics*, 84(4):042331, 2011.

[45] Fabian Ewert and Peter van Loock. 3/4-efficient Bell measurement with passive linear optics and unentangled ancillae. *Physical Review Letters*, 113(14):140403, 2014.

[46] Matthias J Bayerbach, Simone E D'Aurelio, Peter van Loock, and Stefanie Barz. Bell-state measurement exceeding 50% success probability with linear optics. *Science Advances*, 9(32):eadf4080, 2023.

[47] Yong Yu, Fei Ma, Xi-Yu Luo, Bo Jing, Peng-Fei Sun, Ren-Zhou Fang, Chao-Wei Yang, Hui Liu, Ming-Yang Zheng, Xiu-Ping Xie, et al. Entanglement of two quantum memories via fibres over dozens of kilometres. *Nature*, 578(7794):240–245, 2020.

[48] Dario Lago-Rivera, Samuele Grandi, Jelena V Rakonjac, Alessandro Seri, and Hugues de Riedmatten. Telecom-heralded entanglement between multimode solid-state quantum memories. *Nature*, 594(7861):37–40, 2021.

[49] Xiao Liu, Jun Hu, Zong-Feng Li, Xue Li, Pei-Yun Li, Peng-Jun Liang, Zong-Quan Zhou, Chuan-Feng Li, and Guang-Can Guo. Heralded entanglement distribution between two absorptive quantum memories. *Nature*, 594(7861):41–45, 2021.

[50] Tim van Leent, Matthias Bock, Florian Fertig, Robert Garthoff, Sebastian Eppelt, Yiru Zhou, Pooja Malik, Matthias Seubert, Tobias Bauer, Wenjamin Rosenfeld, et al. Entangling single atoms over 33 km telecom fibre. *Nature*, 607(7917):69–73, 2022.

[51] Arian J Stolk, Kian L van der Enden, Marie-Christine Slater, Ingmar te Raa-Derckx, Pieter Botma, Joris van Rantwijk, JJ Benjamin Biemond, Ronald AJ Hagen, Rodolf W Herfst, Wouter D Koek, et al. Metropolitan-scale heralded entanglement of solid-state qubits. *Science Advances*, 10(44):eadp6442, 2024.

[52] Can M Knaut, Aziza Suleymanzade, Y-C Wei, Daniel R Assumpcao, P-J Stas, Yan Qi Huan, Bartholomeus Machielse, Erik N Knall, Madison Sutula, Gefen Baranes, et al. Entanglement of nanophotonic quantum memory nodes in a telecom network. *Nature*, 629(8012):573–578, 2024.

[53] Jian-Long Liu, Xi-Yu Luo, Yong Yu, Chao-Yang Wang, Bin Wang, Yi Hu, Jun Li, Ming-Yang Zheng, Bo Yao, Zi Yan, et al. Creation of memory–memory entanglement in a metropolitan quantum network. *Nature*, 629(8012):579–585, 2024.

[54] Xi-Yu Luo, Chao-Yang Wang, Ming-Yang Zheng, Bin Wang, Jian-Long Liu, Bo-Feng Gao, Jun Li, Zi Yan, Qiao-Mu Ke, Da Teng, et al. Entangling quantum memories over 420 km in fiber. *arXiv preprint arXiv:2504.05660*, 2025.

[55] Zong-Quan Zhou, Chao Liu, Chuan-Feng Li, Guang-Can Guo, Daniel Oblak, Mi Lei, Andrei Faraon, Margherita Mazzera, and Hugues de Riedmatten. Photonic integrated quantum memory in rare-earth doped solids. *Laser & Photonics Reviews*, 17(10):2300257, 2023.

[56] Yunfei Wang, Jianfeng Li, Shanchao Zhang, Keyu Su, Yiru Zhou, Kaiyu Liao, Shengwang Du, Hui Yan, and Shi-Liang Zhu. Efficient quantum memory for single-photon polarization qubits. *Nature Photonics*, 13(5):346–351, 2019.

[57] Sheng-Jun Yang, Xu-Jie Wang, Xiao-Hui Bao, and Jian-Wei Pan. An efficient quantum light–matter interface with sub-second lifetime. *Nature Photonics*, 10(6):381–384, 2016.

[58] Jürgen Appel, Eden Figueroa, Dmitry Korystov, M. Lobino, and A. I. Lvovsky. Quantum memory for squeezed light. *Physical Review Letters*, 100(9):093602, 2008.

[59] Chin-Wen Chou, Hugues De Riedmatten, Daniel Felinto, Sergey V Polyakov, Steven J Van Enk, and H Jeff Kimble. Measurement-induced entanglement for excitation stored in remote atomic ensembles. *Nature*, 438(7069):828–832, 2005.

[60] M. D. Eisaman, A. André, F. Massou, M. Fleischhauer, A. S. Zibrov, and M. D. Lukin. Electromagnetically induced transparency with tunable single-photon pulses. *Nature*, 438(7069):837–841, 2005.

[61] Jinxian Guo, Xiaotian Feng, Peiyu Yang, Zhifei Yu, L. Q. Chen, Chun-Hua Yuan, and Weiping Zhang. High-performance Raman quantum memory with optimal control in room temperature atoms. *Nature Communications*, 10:148, 2019.

[62] X. L. Zhang, J. W. Pan, X. T. Li, Z. Y. Xie, and H. L. Li. High-efficiency quantum memory for coherent light in warm atoms. *Nature Communications*, 5:3576, 2014.

[63] H. Y. Liu, Y. Z. Zhang, L. Yang, L. J. Wang, and W. T. Liu. Quantum memory for photons stored in warm rubidium vapor. *Physical Review Letters*, 110(4):043603, 2013.

[64] M. Hosseini, B. M. Sparkes, G. Campbell, P. K. Lam, and B. C. Buchler. High efficiency coherent optical memory with warm rubidium vapour. *Nature Communications*, 2:174, 2011.

[65] S. D. Jenkins, S. P. McGlynn, A. S. F. Tchekhovskoy, M. R. T. P. L., B. S. K., and T. M. McGlynn. Optical quantum memory using warm rubidium vapor. *Physical Review A*, 79(3):033839, 2009.

[66] D. F. Phillips, A. Fleischhauer, A. Mair, R. L. Walsworth, and M. D. Lukin. Storage of light in atomic vapor. *Physical Review Letters*, 86(14):783–786, 2001.

[67] Dario Lago-Rivera, Samuele Grandi, Jelena V. Rakonjac, Alessandro Seri, and Hugues de Riedmatten. Telecom-heralded entanglement between multimode solid-state quantum memories. *Nature*, 594(7861):37–40, 2021.

[68] Xianxin Liu, Yiheng Zhou, Zong-Quan Zhou, Chuan-Feng Li, Guang-Can Guo, Daniel Oblak, Mi Lei, Andrei Faraon, Margherita Mazzera, and Hugues de Riedmatten. Her-

alded entanglement distribution between two absorptive quantum memories. *Nature*, 594(7861):41–45, 2021.

[69] K. F. Reim, J. Nunn, V. O. Lorenz, B. J. Sussman, K. C. Lee, N. K. Langford, D. Jaksch, and I. A. Walmsley. Towards high-speed optical quantum memories. *Nature Photonics*, 4(4):218–221, 2010.

[70] Hugues de Riedmatten, Mikael Afzelius, Matthias U. Staudt, Christoph Simon, and Nicolas Gisin. A solid-state light–matter interface at the single-photon level. *Nature*, 456(7223):773–777, 2008.

[71] Matthias Körber, Olivier Morin, Stefan Langenfeld, Andreas Neuzner, Stephan Ritter, and Gerhard Rempe. Decoherence-protected memory for a single-photon qubit. *Nature Photonics*, 12(1):18–21, 2018.

[72] Stephan Ritter, Christian Nölleke, Carolin Hahn, Andreas Reiserer, Andreas Neuzner, Manuel Uphoff, Martin Mücke, Eden Figueroa, Joerg Bochmann, and Gerhard Rempe. An elementary quantum network of single atoms in optical cavities. *Nature*, 484(7393):195–200, 2012.

[73] Holger P. Specht, Christian Nölleke, Andreas Reiserer, Manuel Uphoff, Eden Figueroa, Stephan Ritter, and Gerhard Rempe. A single-atom quantum memory. *Nature*, 473(7346):190–193, 2011.

[74] Tatjana Wilk, Simon C. Webster, Axel Kuhn, and Gerhard Rempe. Single-atom single-photon quantum interface. *Science*, 317(5837):488–490, 2007.

[75] Stephan Kucera, Christian Haen, Elena Arenskötter, Tobias Bauer, Jonas Meiers, Marlon Schäfer, Ross Boland, Milad Yahyapour, Maurice Lessing, Ronald Holzwarth, Christoph Becher, and Jürgen Eschner. Demonstration of quantum network protocols over a 14-km urban fiber link. *npj Quantum Information*, 10(1):88, 2024.

[76] Ye Wang, Mark Um, Junhua Zhang, Shuoming An, Ming Lyu, Jing-Ning Zhang, L.-M. Duan, Dahyun Yum, and Kihwan Kim. Single-qubit quantum memory exceeding ten-minute coherence time. *Nature Photonics*, 11(10):646–650, 2017.

[77] David L. Moehring, Peter Maunz, Steven Olmschenk, Kevin C. Younge, D. N. Matsukevich, L.-M. Duan, and Christopher Monroe. Entanglement of single-atom quantum bits at a distance. *Nature*, 449(7158):68–71, 2007.

[78] M. Pompili and et al. Realization of a multinode quantum network of remote solid-state qubits. *Science*, 372(6539):259–264, 2021.

[79] H. Bernien and et al. Heralded entanglement between solid-state qubits separated by three metres. *Nature*, 497(7447):86–90, 2013.

[80] G. D. Fuchs, G. Burkard, P. V. Klimov, and D. D. Awschalom. A quantum memory intrinsic to single nitrogen vacancy centres in diamond. *Nature Physics*, 7(10):789–793, 2011.

[81] B. Hensen and et al. Loophole-free Bell inequality violation using electron spins separated by 1.3 kilometres. *Nature*, 526(7575):682–686, 2015.

[82] E. Bersin and et al. Telecom networking with a diamond quantum memory. *PRX Quantum*, 5(1):010303, 2024.

[83] P.-J. Stas and et al. Robust multi-qubit quantum network node with integrated error detection. *Science*, 378(6619):557–560, 2022.

[84] M. K. Bhaskar and et al. Experimental demonstration of memory-enhanced quantum communication. *Nature*, 580(7801):60–64, 2020.

[85] C. T. Nguyen and et al. Quantum network nodes based on diamond qubits with an efficient nanophotonic interface. *Physical Review Letters*, 123(18):183602, 2019.

[86] Jonathan M Kindem, Andrei Ruskuc, John G Bartholomew, Jake Rochman, Yan Qi Huan, and Andrei Faraon. Control and single-shot readout of an ion embedded in a nanophotonic cavity. *Nature*, 580(7802):201–204, 2020.

[87] Songtao Chen, Mouktik Raha, Christopher M Phenicie, Salim Ourari, and Jeff D Thompson. Parallel single-shot measurement and coherent control of solid-state spins below the diffraction limit. *Science*, 370(6516):592–595, 2020.

[88] Tian Zhong, Jonathan M. Kindem, John G. Bartholomew, et al. Optically addressing single rare-earth ions in a nanophotonic cavity. *Physical Review Letters*, 121:183603, 2018.

[89] Alan Dibos, Mouktik Raha, Claire Phenicie, and Jeff Thompson. Atomic source of single photons in the telecom band. *Physical Review Letters*, 120:243601, 2018.

[90] Chi Yin, Marko Rancic, Greg G. de Boo, et al. Optical addressing of an individual erbium ion in silicon. *Nature*, 497:91–95, 2013.

[91] L Bergeron, C Chartrand, ATK Kurkjian, KJ Morse, H Riemann, NV Abrosimov, P Becker, H-J Pohl, MLW Thewalt, and S Simmons. Silicon-integrated telecommunications photon-spin interface. *PRX Quantum*, 1(2):020301, 2020.

[92] Adam Johnston, Ulises Felix-Rendon, Yu-En Wong, and Songtao Chen. Cavity-coupled telecom atomic source in silicon. *Nature Communications*, 15(1):2350, 2024.

[93] Francis Afzal, Mohsen Akhlaghi, Stefanie J Beale, Olinka Bedroya, Kristin Bell, Laurent Bergeron, Kent Bonsma-Fisher, Polina Bychkova, Zachary ME Chaisson, Camille Chartrand, et al. Distributed quantum computing in silicon. *arXiv preprint arXiv:2406.01704*, 2024.

[94] Lukasz Komza, Xueyue Zhang, Hanbin Song, Yu-Lung Tang, Xin Wei, and Alp Sipahigil. Multiplexed color centers in a silicon photonic cavity array. *Optica*, 12(9):1400–1405, 2025.

[95] Hanbin Song, Xueyue Zhang, Lukasz Komza, Niccolo Fiaschi, Yihuang Xiong, Yiyang Zhi, Scott Dhuey, Adam Schwartzberg, Thomas Schenkel, Geoffroy Hautier, et al. Long-lived entanglement of a spin-qubit register in silicon photonics. *arXiv preprint arXiv:2504.15467*, 2025.

[96] Alessandro Seri, Dario Lago-Rivera, Andreas Lenhard, Giacomo Corrielli, Roberto Osellame, Margherita Mazzera, and Hugues de Riedmatten. Quantum storage of frequency-multiplexed heralded single photons. *Physical Review Letters*, 123(8):080502, 2019.

[97] Christoph Simon, Hugues De Riedmatten, Mikael Afzelius, Nicolas Sangouard, Hugo Zbinden, and Nicolas Gisin. Quantum repeaters with photon pair sources and multimode memories. *Physical Review Letters*, 98(19):190503, 2007.

[98] J Nunn, K Reim, KC Lee, VO Lorenz, BJ Sussman, IA Walmsley, and D Jaksch. Multimode memories in atomic ensembles. *Physical Review Letters*, 101(26):260502, 2008.

[99] V Krutyanskiy, M Canteri, M Meraner, V Krcmarsky, and BP Lanyon. Multimode ion-photon entanglement over 101 kilometers. *PRX Quantum*, 5(2):020308, 2024.

[100] M Canteri, ZX Koong, J Bate, A Winkler, V Krutyanskiy, and BP Lanyon. A photon-interfaced ten qubit quantum network node. *arXiv preprint arXiv:2406.09480*, 2024.

[101] Hugues De Riedmatten, Mikael Afzelius, Matthias U Staudt, Christoph Simon, and Nicolas Gisin. A solid-state light–matter interface at the single-photon level. *Nature*, 456(7223):773–777, 2008.

[102] Mikael Afzelius, Imam Usmani, Atia Amari, Björn Lauritzen, Andreas Walther, Christoph Simon, Nicolas Sangouard, Jiří Minář, Hugues De Riedmatten, Nicolas Gisin, et al. Demonstration of atomic frequency comb memory for light with spin-wave storage. *Physical Review Letters*, 104(4):040503, 2010.

[103] Pierre Jobez, Cyril Laplane, Nuala Timoney, Nicolas Gisin, Alban Ferrier, Philippe Goldner, and Mikael Afzelius. Coherent spin control at the quantum level in an ensemble-based optical memory. *Physical Review Letters*, 114(23):230502, 2015.

[104] Yu Ma, You-Zhi Ma, Zong-Quan Zhou, Chuan-Feng Li, and Guang-Can Guo. One-hour coherent optical storage in an atomic frequency comb memory. *Nature Communications*, 12(1):2381, 2021.

[105] Antonio Ortu, Adrian Holzäpfel, Jean Etesse, and Mikael Afzelius. Storage of photonic time-bin qubits for up to 20 ms in a rare-earth doped crystal. *npj Quantum Information*, 8(1):29, 2022.

[106] Imam Usmani, Mikael Afzelius, Hugues De Riedmatten, and Nicolas Gisin. Mapping multiple photonic qubits into and out of one solid-state atomic ensemble. *Nature Communications*, 1(1):12, 2010.

[107] M Bonarota, JL Le Gouët, and T Chaneliere. Highly multimode storage in a crystal. *New Journal of Physics*, 13(1):013013, 2011.

[108] Tian-Shu Yang, Zong-Quan Zhou, Yi-Lin Hua, Xiao Liu, Zong-Feng Li, Pei-Yun Li, Yu Ma, Chao Liu, Peng-Jun Liang, Xue Li, et al. Multiplexed storage and real-time manipulation based on a multiple degree-of-freedom quantum memory. *Nature Communications*, 9(1):3407, 2018.

[109] Neil Sinclair, Erhan Saglamyurek, Hassan Mallahzadeh, Joshua A Slater, Mathew George, Raimund Ricken, Morgan P Hedges, Daniel Oblak, Christoph Simon, Wolfgang

Sohler, et al. Spectral multiplexing for scalable quantum photonics using an atomic frequency comb quantum memory and feed-forward control. *Physical Review Letters*, 113(5):053603, 2014.

[110] Mohammed K Alqedra, Sebastian P Horvath, Adam Kinos, Andreas Walther, Stefan Kröll, and Lars Rippe. Stark control of solid-state quantum memory with spin-wave storage. *Physical Review A*, 109(1):012607, 2024.

[111] Matthias Ulrich Staudt, Mikael Afzelius, Hugues De Riedmatten, Sara Rose Hastings-Simon, Christoph Simon, R Ricken, <? format?> H Suche, W Sohler, and Nicolas Gisin. Interference of multimode photon echoes generated<? format?> in spatially separated solid-state atomic ensembles. *Physical Review Letters*, 99(17):173602, 2007.

[112] Zong-Quan Zhou, Wei-Bin Lin, Ming Yang, Chuan-Feng Li, and Guang-Can Guo. Realization of reliable solid-state quantum memory for photonic polarization qubit. *Physical Review Letters*, 108(19):190505, 2012.

[113] Mustafa Gündoğan, Patrick M Ledingham, Kutlu Kutluer, Margherita Mazzera, and Hugues De Riedmatten. Solid state spin-wave quantum memory for time-bin qubits. *Physical Review Letters*, 114(23):230501, 2015.

[114] Jelena V Rakonjac, Dario Lago-Rivera, Alessandro Seri, Margherita Mazzera, Samuele Grandi, and Hugues De Riedmatten. Entanglement between a telecom photon and an on-demand multimode solid-state quantum memory. *Physical Review Letters*, 127(21):210502, 2021.

[115] Mahmood Sabooni, Qian Li, Stefan Kröll, and Lars Rippe. Efficient quantum memory using a weakly absorbing sample. *Physical Review Letters*, 110(13):133604, 2013.

[116] Pierre Jobez, Imam Usmani, Nuala Timoney, Cyril Laplane, Nicolas Gisin, and Mikael Afzelius. Cavity-enhanced storage in an optical spin-wave memory. *New Journal of Physics*, 16(8):083005, 2014.

[117] Mahmood Sabooni, S Tornibue Kometa, Axel Thuresson, Stefan Kröll, and Lars Rippe. Cavity-enhanced storage—preparing for high-efficiency quantum memories. *New Journal of Physics*, 15(3):035025, 2013.

[118] RA Akhmedzhanov, LA Gushchin, AA Kalachev, NA Nizov, VA Nizov, DA Sobgayda, and IV Zelensky. Cavity-assisted atomic frequency comb memory in an isotopically pure 143nd3+: Ylif4 crystal. *Laser Physics Letters*, 13(11):115203, 2016.

[119] Jacob H Davidson, Pascal Lefebvre, Jun Zhang, Daniel Oblak, and Wolfgang Tittel. Improved light-matter interaction for storage of quantum states of light in a thulium-doped crystal cavity. *Physical Review A*, 101(4):042333, 2020.

[120] Stefano Duranti, Sören Wengerowsky, Leo Feldmann, Alessandro Seri, Bernardo Casabone, and Hugues de Riedmatten. Efficient cavity-assisted storage of photonic qubits in a solid-state quantum memory. *arXiv preprint arXiv:2307.03509*, 2023.

[121] Tian Zhong, Jonathan M Kindem, John G Bartholomew, Jake Rochman, Ioana Craiciu, Evan Miyazono, Marco Bettinelli, Enrico Cavalli, Varun Verma, Sae Woo Nam, et al. Nanophotonic rare-earth quantum memory with optically controlled retrieval. *Science*, 357(6358):1392–1395, 2017.

[122] Ioana Craiciu, Mi Lei, Jake Rochman, Jonathan M Kindem, John G Bartholomew, Evan Miyazono, Tian Zhong, Neil Sinclair, and Andrei Faraon. Nanophotonic quantum storage at telecommunication wavelength. *Physical Review Applied*, 12(2):024062, 2019.

[123] M Bonarota, JL Le Gouët, SA Moiseev, and T Chaneliere. Atomic frequency comb storage as a slow-light effect. *Journal of Physics B: Atomic, Molecular and Optical Physics*, 45(12):124002, 2012.

[124] PR Berman and J-L Le Gouët. Pulsed field transmission by atomic frequency combs and random spike media: The prominent role of dispersion. *Physical Review A*, 103(4):043723, 2021.

[125] R de L Kronig. On the theory of dispersion of x-rays. *Josa*, 12(6):547–557, 1926.

[126] Hendrik Anthony Kramers. La diffusion de la lumiere par les atomes. In *Atti Cong. Intern. Fisica (Transactions of Volta Centenary Congress) Como*, volume 2, pages 545–557, 1927.

[127] Valerio Lucarini, Jarkko J Saarinen, Kai-Erik Peiponen, and Erik M Vartiainen. *Kramers-Kronig relations in optical materials research*, volume 110. Springer Science & Business Media, 2005.

[128] Alexander I Lvovsky, Barry C Sanders, and Wolfgang Tittel. Optical quantum memory. *Nature Photonics*, 3(12):706–714, 2009.

[129] K-J Boller, A Imamoğlu, and Stephen E Harris. Observation of electromagnetically induced transparency. *Physical Review Letters*, 66(20):2593, 1991.

[130] Ya-Fen Hsiao, Pin-Ju Tsai, Hung-Shiue Chen, Sheng-Xiang Lin, Chih-Chiao Hung, Chih-Hsi Lee, Yi-Hsin Chen, Yong-Fan Chen, Ite A Yu, and Ying-Cheng Chen. Highly efficient coherent optical memory based on electromagnetically induced transparency. *Physical Review Letters*, 120(18):183602, 2018.

[131] Marcel Hain, Markus Stabel, and Thomas Halfmann. Few-photon storage on a second timescale by electromagnetically induced transparency in a doped solid. *New Journal of Physics*, 24(2):023012, 2022.

[132] J Nunn, IA Walmsley, MG Raymer, K Surmacz, FC Waldermann, Z Wang, and D Jaksch. Mapping broadband single-photon wave packets into an atomic memory. *Physical Review A—Atomic, Molecular, and Optical Physics*, 75(1):011401, 2007.

[133] Lukas Heller, Jan Lowinski, Klara Theophilo, Auxiliadora Padrón-Brito, and Hugues de Riedmatten. Raman storage of quasideterministic single photons generated by rydberg collective excitations in a low-noise quantum memory. *Physical Review Applied*, 18(2):024036, 2022.

[134] KF Reim, J Nunn, VO Lorenz, BJ Sussman, KC Lee, NK Langford, D Jaksch, and IA Walmsley. Towards high-speed optical quantum memories. *Nature Photonics*, 4(4):218–221, 2010.

[135] Dong-Sheng Ding and Dong-Sheng Ding. Raman quantum memory of photonic polarized entanglement. *Broad Bandwidth and High Dimensional Quantum Memory Based on Atomic Ensembles*, pages 91–107, 2018.

[136] SA Moiseev and Stefan Kröll. Complete reconstruction of the quantum state of a single-photon wave packet absorbed by a doppler-broadened transition. *Physical Review Letters*, 87(17):173601, 2001.

[137] Barbara Kraus, Wolfgang Tittel, Nicolas Gisin, Mattias Nilsson, Stefan Kröll, and J Ignacio Cirac. Quantum memory for nonstationary light fields based on controlled reversible inhomogeneous broadening. *Physical Review A—Atomic, Molecular, and Optical Physics*, 73(2):020302, 2006.

[138] Nicolas Sangouard, Christoph Simon, Mikael Afzelius, and Nicolas Gisin. Analysis of a quantum memory for photons based on controlled reversible inhomogeneous broadening. *Physical Review A—Atomic, Molecular, and Optical Physics*, 75(3):032327, 2007.

[139] Björn Lauritzen, Jiří Minář, Hugues De Riedmatten, Mikael Afzelius, Nicolas Sangouard, <? format?> Christoph Simon, and Nicolas Gisin. Telecommunication-wavelength solid-state memory at the single photon level. *Physical Review Letters*, 104(8):080502, 2010.

[140] Gabriel Hétet, JJ Longdell, MJ Sellars, Ping Koy Lam, and BC Buchler. Multimodal properties and dynamics of gradient echo quantum memory. *Physical Review Letters*, 101(20):203601, 2008.

[141] Mattias Nilsson and Stefan Kröll. Solid state quantum memory using complete absorption and re-emission of photons by tailored and externally controlled inhomogeneous absorption profiles. *Optics Communications*, 247(4-6):393–403, 2005.

[142] Gabriel Hetet, JJ Longdell, AL Alexander, Ping Koy Lam, and MJ Sellars. Electro-optic quantum memory for light using two-level atoms. *Physical Review Letters*, 100(2):023601, 2008.

[143] Mahdi Hosseini, Ben M Sparkes, Gabriel Hétet, Jevon J Longdell, Ping Koy Lam, and Ben C Buchler. Coherent optical pulse sequencer for quantum applications. *Nature*, 461(7261):241–245, 2009.

[144] Morgan P Hedges, Jevon J Longdell, Yongmin Li, and Matthew J Sellars. Efficient quantum memory for light. *Nature*, 465(7301):1052–1056, 2010.

[145] Mahdi Hosseini, Geoff Campbell, Ben M Sparkes, Ping K Lam, and Ben C Buchler. Unconditional room-temperature quantum memory. *Nature Physics*, 7(10):794–798, 2011.

[146] Anindya Rastogi. Light-matter interactions for quantum simulation and quantum memory experiments. Master's thesis, University of Alberta, 2018.

[147] Erhan Saglamyurek, Taras Hrushevskyi, Anindya Rastogi, Khabat Heshami, and Lindsay J LeBlanc. Coherent storage and manipulation of broadband photons via dynamically controlled autler–townes splitting. *Nature Photonics*, 12(12):774–782, 2018.

[148] Erhan Saglamyurek, Taras Hrushevskyi, Logan Cooke, Anindya Rastogi, and Lindsay J LeBlanc. Single-photon-level light storage in cold atoms using the autler-townes splitting protocol. *Physical Review Research*, 1(2):022004, 2019.

[149] Erhan Saglamyurek, Taras Hrushevskyi, Anindya Rastogi, Logan W Cooke, Benjamin D Smith, and Lindsay J LeBlanc. Storing short single-photon-level optical pulses in bose–einstein condensates for high-performance quantum memory. *New Journal of Physics*, 23(4):043028, 2021.

[150] Daniel B Higginbottom, Faezeh Kimiaee Asadi, Camille Chartrand, Jia-Wei Ji, Laurent Bergeron, Michael LW Thewalt, Christoph Simon, and Stephanie Simmons. Memory and transduction prospects for silicon t center devices. *PRX Quantum*, 4(2):020308, 2023.

[151] Feihu Xu, Xiongfeng Ma, Qiang Zhang, Hoi-Kwong Lo, and Jian-Wei Pan. Secure quantum key distribution with realistic devices. *Reviews of Modern Physics*, 92(2):025002, 2020.

[152] Chankyun Lee, Eunjoo Lee, and Wonhyuk Lee. Analysis on eavesdropper detection in bb84 quantum key distribution protocol against partial intercept-and-resend attack. *2023 International Conference on Optical Network Design and Modeling (ONDM)*, 2023.

[153] Artur K Ekert. Quantum cryptography based on Bell's theorem. *Physical Review Letters*, 67(6):661, 1991.

[154] Sheng-Kai Liao, Wen-Qi Cai, Wei-Yue Liu, Liang Zhang, Yang Li, Ji-Gang Ren, Juan Yin, Qi Shen, Yuan Cao, Zheng-Ping Li, et al. Satellite-to-ground quantum key distribution. *Nature*, 549(7670):43–47, 2017.

[155] Alberto Boaron, Gianluca Boso, Davide Rusca, Cédric Vulliez, Claire Autebert, Misael Caloz, Matthieu Perrenoud, Gaëtan Gras, Félix Bussières, Ming-Jun Li, et al.

Secure quantum key distribution over 421 km of optical fiber. *Physical Review Letters*, 121(19):190502, 2018.

[156] Sheng-Kai Liao, Wen-Qi Cai, Johannes Handsteiner, Bo Liu, Juan Yin, Liang Zhang, Dominik Rauch, Matthias Fink, Ji-Gang Ren, Wei-Yue Liu, et al. Satellite-relayed intercontinental quantum network. *Physical Review Letters*, 120(3):030501, 2018.

[157] Juan Yin, Yu-Huai Li, Sheng-Kai Liao, Meng Yang, Yuan Cao, Liang Zhang, Ji-Gang Ren, Wen-Qi Cai, Wei-Yue Liu, Shuang-Lin Li, et al. Entanglement-based secure quantum cryptography over 1,120 kilometres. *Nature*, 582(7813):501–505, 2020.

[158] Jiu-Peng Chen, Chi Zhang, Yang Liu, Cong Jiang, Weijun Zhang, Xiao-Long Hu, Jian-Yu Guan, Zong-Wen Yu, Hai Xu, Jin Lin, et al. Sending-or-not-sending with independent lasers: Secure twin-field quantum key distribution over 509 km. *Physical Review Letters*, 124(7):070501, 2020.

[159] John Preskill. Quantum computing in the nisq era and beyond. *Quantum*, 2:79, 2018.

[160] C. D. Bruzewicz, J. Chiaverini, R. McConnell, and J. M. Sage. Trapped-ion quantum computing: progress and challenges. *Applied Physics Reviews*, 6:021314, 2019.

[161] S. Bravyi, O. Dial, J. M. Gambetta, D. Gil, and Z. Nazario. The future of quantum computing with superconducting qubits. *Journal of Applied Physics*, 132:160902, 2022.

[162] S. S. Gill et al. Quantum computing: vision and challenges, 2024. Preprint at https://arxiv.org/abs/2403.02240.

[163] L. K. Grover. Quantum telecomputation. *arXiv preprint quant-ph/9704012*, 1997.

[164] J. I. Cirac, A. K. Ekert, S. F. Huelga, and C. Macchiavello. Distributed quantum computation over noisy channels. *Physical Review A*, 59:4249, 1999.

[165] L. Jiang, J. M. Taylor, A. S. Sørensen, and M. D. Lukin. Distributed quantum computation based on small quantum registers. *Physical Review A*, 76:062323, 2007.

[166] C. Monroe et al. Large-scale modular quantum-computer architecture with atomic memory and photonic interconnects. *Physical Review A*, 89:022317, 2014.

[167] J. Eisert, K. Jacobs, P. Papadopoulos, and M. B. Plenio. Optimal local implementation of nonlocal quantum gates. *Physical Review A*, 62:052317, 2000.

[168] D. Gottesman and I. L. Chuang. Demonstrating the viability of universal quantum computation using teleportation and single-qubit operations. *Nature*, 402:390–393, 1999.

[169] Wei-Bo Gao, Alexander M Goebel, Chao-Yang Lu, Han-Ning Dai, Claudia Wagenknecht, Qiang Zhang, Bo Zhao, Cheng-Zhi Peng, Zeng-Bing Chen, Yu-Ao Chen, et al. Teleportation-based realization of an optical quantum two-qubit entangling gate. *Proceedings of the National Academy of Sciences*, 107(49):20869–20874, 2010.

[170] Kevin S Chou, Jacob Z Blumoff, Christopher S Wang, Philip C Reinhold, Christopher J Axline, Yvonne Y Gao, Luigi Frunzio, MH Devoret, Liang Jiang, and RJ Schoelkopf. Deterministic teleportation of a quantum gate between two logical qubits. *Nature*, 561(7723):368–373, 2018.

[171] Yong Wan, Daniel Kienzler, Stephen D Erickson, Karl H Mayer, Ting Rei Tan, Jenny J Wu, Hilma M Vasconcelos, Scott Glancy, Emanuel Knill, David J Wineland, et al. Quantum gate teleportation between separated qubits in a trapped-ion processor. *Science*, 364(6443):875–878, 2019.

[172] D. Main et al. Distributed quantum computing across an optical network link. *Nature*, pages 1–6, 2025.

[173] Christoph Simon. Towards a global quantum network. *Nature Photonics*, 11(11):678–680, 2017.

[174] Stephanie Wehner, David Elkouss, and Ronald Hanson. Quantum internet: A vision for the road ahead. *Science*, 362(6412):eaam9288, 2018.

[175] Sheng-Kai Liao, Wen-Qi Cai, Wei-Yue Liu, Liang Zhang, Yang Li, Ji-Gang Ren, Juan Yin, Qi Shen, Yuan Cao, Zheng-Ping Li, and et al. Satellite-to-ground quantum key distribution. *Nature*, 549(7670):43–47, 2017.

[176] Juan Yin, Yuan Cao, Yu-Huai Li, Sheng-Kai Liao, Liang Zhang, Ji-Gang Ren, Wen-Qi Cai, Wei-Yue Liu, Bo Li, Hui Dai, and et al. Satellite-based entanglement distribution over 1200 kilometers. *Science*, 356(6343):1140–1144, 2017.

[177] Ji-Gang Ren, Ping Xu, Hai-Lin Yong, Liang Zhang, Sheng-Kai Liao, Juan Yin, Wei-Yue Liu, Wen-Qi Cai, Meng Yang, Li Li, et al. Ground-to-satellite quantum teleportation. *Nature*, 549(7670):70–73, 2017.

[178] K. Boone, J.-P. Bourgoin, E. Meyer-Scott, K. Heshami, T. Jennewein, and C. Simon. Entanglement over global distances via quantum repeaters with satellite links. *Physical Review A*, 91(5):052325, 2015.

[179] Mustafa Gündoğan, Thomas Jennewein, Faezeh Kimiaee Asadi, Elisa Da Ros, Erhan Saglamyurek, Daniel Oblak, Daniel Rieländer, Jasminder Sidhu, Samuele Grandi, Luca Mazzarella, and et al. Topical white paper: a case for quantum memories in space. *arXiv preprint arXiv:2111.09595*, 2021.

[180] Shahrzad Taherizadegan, Jacob H Davidson, Sourabh Kumar, Daniel Oblak, and Christoph Simon. Towards a realistic model for cavity-enhanced atomic frequency comb quantum memories. *Quantum Science and Technology*, 9(3):035049, 2024.

[181] Shahrzad Taherizadegan, Faezeh Kimiaee Asadi, Jia-Wei Ji, Daniel Higginbottom, and Christoph Simon. Exploring the feasibility of probabilistic and deterministic quantum gates between t centers in silicon. *arXiv preprint arXiv:2508.06474*, 2025.

[182] Guokui Liu and Bernard Jacquier. *Spectroscopic properties of rare earths in optical materials*, volume 83. Springer Science & Business Media, 2006.

[183] Hugues De Riedmatten and Mikael Afzelius. Quantum light storage in solid state atomic ensembles. In *Engineering the Atom-Photon Interaction: Controlling Fundamental Processes with Photons, Atoms and Solids*, pages 241–273. Springer, 2015.

[184] Y Sun, CW Thiel, RL Cone, RW Equall, and RL Hutcheson. Recent progress in developing new rare earth materials for hole burning and coherent transient applications. *Journal of Luminescence*, 98(1-4):281–287, 2002.

[185] Charles W Thiel, Thomas Böttger, and RL Cone. Rare-earth-doped materials for applications in quantum information storage and signal processing. *Journal of Luminescence*, 131(3):353–361, 2011.

[186] RM Macfarlane, RS Meltzer, and BZ Malkin. Optical measurement of the isotope shifts and hyperfine and superhyperfine interactions of nd in the solid state. *Physical Review B*, 58(9):5692, 1998.

[187] Thierry Chanelière, Jérôme Ruggiero, Matthieu Bonarota, Mikael Afzelius, and JL Le Gouët. Efficient light storage in a crystal using an atomic frequency comb. *New Journal of Physics*, 12(2):023025, 2010.

[188] Laurent Bergeron. Optical and magnetic properties of the t radiation damage centre in ^{28}si. Master's thesis, Simon Fraser University, 2019.

[189] Mihika Prabhu, Carlos Errando-Herranz, Lorenzo De Santis, Ian Christen, Changchen Chen, Connor Gerlach, and Dirk Englund. Individually addressable and spectrally programmable artificial atoms in silicon photonics. *Nature Communications*, 14(1):2380, 2023.

[190] Yoann Baron, Alrik Durand, Péter Udvarhelyi, Tobias Herzig, Mario Khoury, Sébastien Pezzagna, Jan Meijer, Isabelle Robert-Philip, Marco Abbarchi, Jean-Michel Hartmann, et al. Detection of single w-centers in silicon. *ACS Photonics*, 9(7):2337–2345, 2022.

[191] C Chartrand, L Bergeron, KJ Morse, H Riemann, NV Abrosimov, P Becker, H-J Pohl, S Simmons, and MLW Thewalt. Highly enriched si 28 reveals remarkable optical linewidths and fine structure for well-known damage centers. *Physical Review B*, 98(19):195201, 2018.

[192] AN Safonov and EC Lightowlers. Photoluminescence characterisation of hydrogen-related centres in silicon. *Materials Science and Engineering: B*, 58(1-2):39–47, 1999.

[193] Stephanie Simmons. Scalable fault-tolerant quantum technologies with silicon color centers. *PRX Quantum*, 5(1):010102, 2024.

[194] AN Safonov, EC Lightowlers, Gordon Davies, P Leary, R Jones, and Sven Öberg. Interstitial-carbon hydrogen interaction in silicon. *Physical Review Letters*, 77(23):4812, 1996.

[195] Daniel B Higginbottom, Alexander TK Kurkjian, Camille Chartrand, Moein Kazemi, Nicholas A Brunelle, Evan R MacQuarrie, James R Klein, Nicholas R Lee-Hone, Jakub Stacho, Myles Ruether, et al. Optical observation of single spins in silicon. *Nature*, 607(7918):266–270, 2022.

[196] ER MacQuarrie, Camille Chartrand, DB Higginbottom, KJ Morse, VA Karasyuk, Sjoerd Roorda, and Stephanie Simmons. Generating t centres in photonic silicon-on-insulator material by ion implantation. *New Journal of Physics*, 23(10):103008, 2021.

[197] NS Minaev and AV Mudryi. Thermally-induced defects in silicon containing oxygen and carbon. *physica status solidi (a)*, 68(2):561–565, 1981.

[198] E Irion, N Burger, K Thonke, and R Sauer. The defect luminescence spectrum at 0.9351 ev in carbon-doped heat-treated or irradiated silicon. *Journal of Physics C: Solid State Physics*, 18(26):5069, 1985.

[199] AN Safonov and Edward C Lightowlers. Hydrogen related optical centers in radiation damaged silicon. In *Materials Science Forum*, volume 143, pages 903–908. Trans Tech Publ, 1993.

[200] P Leary, R Jones, and Sven Öberg. Interaction of hydrogen with substitutional and interstitial carbon defects in silicon. *Physical Review B*, 57(7):3887, 1998.

[201] Adam DeAbreu, Camille Bowness, Amirhossein Alizadeh, Camille Chartrand, NA Brunelle, ER MacQuarrie, NR Lee-Hone, Myles Ruether, Moein Kazemi, ATK Kurkjian, et al. Waveguide-integrated silicon t centres. *Optics Express*, 31(9):15045–15057, 2023.

[202] Fariba Islam, Chang-Min Lee, Samuel Harper, Mohammad Habibur Rahaman, Yuqi Zhao, Neelesh Kumar Vij, and Edo Waks. Cavity-enhanced emission from a silicon t center. *Nano Letters*, 24(1):319–325, 2023.

[203] Y-W Cho, GT Campbell, JL Everett, J Bernu, DB Higginbottom, MT Cao, J Geng, NP Robins, PK Lam, and BC Buchler. Highly efficient optical quantum memory with long coherence time in cold atoms. *Optica*, 3(1):100–107, 2016.

[204] YO Dudin, L Li, and A Kuzmich. Light storage on the time scale of a minute. *Physical Review A—Atomic, Molecular, and Optical Physics*, 87(3):031801, 2013.

[205] Nikolai Lauk, Christopher O'Brien, and Michael Fleischhauer. Fidelity of photon propagation in electromagnetically induced transparency in the presence of four-wave mixing. *Physical Review A—Atomic, Molecular, and Optical Physics*, 88(1):013823, 2013.

[206] Peter Christian Maurer, Georg Kucsko, Christian Latta, Liang Jiang, Norman Ying Yao, Steven D Bennett, Fernando Pastawski, David Hunger, Nicholas Chisholm, Matthew Markham, et al. Room-temperature quantum bit memory exceeding one second. *Science*, 336(6086):1283–1286, 2012.

[207] P-J Stas, Yan Qi Huan, Bartholomeus Machielse, Erik N Knall, Aziza Suleymanzade, Benjamin Pingault, Madison Sutula, Sophie W Ding, Can M Knaut, Daniel R Assumpcao, et al. Robust multi-qubit quantum network node with integrated error detection. *Science*, 378(6619):557–560, 2022.

[208] CT Nguyen, DD Sukachev, MK Bhaskar, Bartholomeus Machielse, DS Levonian, EN Knall, Pavel Stroganov, Ralf Riedinger, Hongkun Park, M Lončar, et al. Quantum network nodes based on diamond qubits with an efficient nanophotonic interface. *Physical Review Letters*, 123(18):183602, 2019.

[209] Sean D Barrett and Pieter Kok. Efficient high-fidelity quantum computation using matter qubits and linear optics. *Physical Review A*, 71(6):060310, 2005.

[210] Matteo Pompili, Sophie LN Hermans, Simon Baier, Hans KC Beukers, Peter C Humphreys, Raymond N Schouten, Raymond FL Vermeulen, Marijn J Tiggelman, Laura dos Santos Martins, Bas Dirkse, et al. Realization of a multinode quantum network of remote solid-state qubits. *Science*, 372(6539):259–264, 2021.

[211] Can M Knaut, Aziza Suleymanzade, Yan-Cheng Wei, Daniel R Assumpcao, Pieter-Jan Stas, Yan Qi Huan, Bartholomeus Machielse, Erik N Knall, Madison Sutula, Gefen Baranes, et al. Entanglement of nanophotonic quantum memory nodes in a telecommunication network. *arXiv preprint arXiv:2310.01316*, 2023.

[212] Christoph Simon, Mikael Afzelius, Jürgen Appel, A Boyer de La Giroday, SJ Dewhurst, Nicolas Gisin, CY Hu, F Jelezko, Stefan Kröll, JH Müller, et al. Quantum memories. *The European Physical Journal D*, 58(1):1–22, 2010.

[213] Khabat Heshami, Duncan G England, Peter C Humphreys, Philip J Bustard, Victor M Acosta, Joshua Nunn, and Benjamin J Sussman. Quantum memories: emerging applications and recent advances. *Journal of Modern Optics*, 63(20):2005–2028, 2016.

[214] Lijun Ma, Oliver Slattery, and Xiao Tang. Optical quantum memory and its applications in quantum communication systems. *Journal of Research of the National Institute of Standards and Technology*, 125, 2020.

[215] Félix Bussières, Nicolas Sangouard, Mikael Afzelius, Hugues De Riedmatten, Christoph Simon, and Wolfgang Tittel. Prospective applications of optical quantum memories. *Journal of Modern Optics*, 60(18):1519–1537, 2013.

[216] Mustafa Gündoğan, Margherita Mazzera, Patrick M Ledingham, Matteo Cristiani, and Hugues de Riedmatten. Coherent storage of temporally multimode light using a spin-wave atomic frequency comb memory. *New Journal of Physics*, 15(4):045012, 2013.

[217] Antonio Ortu, Jelena V Rakonjac, Adrian Holzäpfel, Alessandro Seri, Samuele Grandi, Margherita Mazzera, Hugues de Riedmatten, and Mikael Afzelius. Multimode capacity of atomic-frequency comb quantum memories. *Quantum Science and Technology*, 7(3):035024, 2022.

[218] Pierre Jobez, Nuala Timoney, Cyril Laplane, Jean Etesse, Alban Ferrier, Philippe Goldner, Nicolas Gisin, and Mikael Afzelius. Towards highly multimode optical quantum memory for quantum repeaters. *Physical Review A*, 93(3):032327, 2016.

[219] Shi-Hai Wei, Bo Jing, Xue-Ying Zhang, Jin-Yu Liao, Hao Li, Li-Xing You, Zhen Wang, You Wang, Guang-Wei Deng, Hai-Zhi Song, et al. Quantum storage of 1650 modes of single photons at telecom wavelength. *npj Quantum Information*, 10(1):19, 2024.

[220] Mucheng Guo, Shuping Liu, Weiye Sun, Miaomiao Ren, Fudong Wang, and Manjin Zhong. Rare-earth quantum memories: The experimental status quo. *Frontiers of Physics*, 18(2):21303, 2023.

[221] Adrian Holzäpfel, Jean Etesse, Krzysztof T Kaczmarek, Alexey Tiranov, Nicolas Gisin, and Mikael Afzelius. Optical storage for 0.53 s in a solid-state atomic frequency comb memory using dynamical decoupling. *New Journal of Physics*, 22(6):063009, jun 2020.

[222] Antonio Ortu, Adrian Holzäpfel, Jean Etesse, and Mikael Afzelius. Storage of photonic time-bin qubits for up to 20 ms in a rare-earth doped crystal. *npj Quantum Information*, 8(1):29, Mar 2022.

[223] M Bonarota, J Ruggiero, J-L Le Gouët, and T Chanelière. Efficiency optimization for atomic frequency comb storage. *Physical Review A*, 81(3):033803, 2010.

[224] S Yasui, M Hiraishi, A Ishizawa, H Omi, T Inaba, X Xu, R Kaji, S Adachi, and T Tawara. Creation of a high-resolution atomic frequency comb and optimization of the pulse sequence for high-efficiency quantum memory in 167 er: Y 2 sio 5. *Optics Continuum*, 1(9):1896–1908, 2022.

[225] Wolfgang Tittel, Mikael Afzelius, Thierry Chaneliere, Rufus L Cone, Stefan Kröll, Sergey A Moiseev, and Matthew Sellars. Photon-echo quantum memory in solid state systems. *Laser & Photonics Reviews*, 4(2):244–267, 2010.

[226] Sergey A. Moiseev, Sergey N. Andrianov, and Firdus F. Gubaidullin. Efficient multimode quantum memory based on photon echo in an optimal QED cavity. *Physical Review A*, 82:022311, Aug 2010.

[227] Markus Pollnau and Marc Eichhorn. Spectral coherence, part i: Passive-resonator linewidth, fundamental laser linewidth, and schawlow-townes approximation. *Progress in Quantum Electronics*, page 100255, 2020.

[228] Anthony E Siegman. *Lasers*. University Science Books, 1986.

[229] John S Toll. Causality and the dispersion relation: logical foundations. *Physical review*, 104(6):1760, 1956.

[230] Bahaa E. A. Saleh and Malvin Carl Teich. *Fundamentals of Photonics*. John Wiley & Sons, Inc., August 1991.

[231] David E Zelmon, David L Small, and Ralph Page. Refractive-index measurements of undoped yttrium aluminum garnet from 0.4 to 5.0 μm. *Applied Optics*, 37(21):4933–4935, 1998.

[232] J Hrabovskỳ, M Kučera, L Paloušová, Lei Bi, and Martin Veis. Optical characterization of y 3 al 5 o 12 and lu 3 al 5 o 12 single crystals. *Optical Materials Express*, 11(4):1218–1223, 2021.

[233] Youn Seok Lee, Kimia Mohammadi, Lindsay Babcock, Brendon L Higgins, Hugh Podmore, and Thomas Jennewein. Robotized polarization characterization platform for free-space quantum communication optics. *Review of Scientific Instruments*, 93(3), 2022.

[234] Thomas Jennewein, Christoph Simon, Andre Fougeres, Francois Babin, Faezeh Kimiaee Asadi, Katanya B Kuntz, Mathieu Maisonneuve, Brian Moffat, Kimia Mohammadi, and Denis Panneton. Qeyssat 2.0–white paper on satellite-based quantum communication missions in canada. *arXiv preprint arXiv:2306.02481*, 2023.

[235] Hugh Podmore, I D'Souza, J Cain, T Jennewein, BL Higgins, YS Lee, A Koujelev, D Hudson, and A McColgan. QKD terminal for canada's quantum encryption and science satellite (qeyssat). In *International Conference on Space Optics—ICSO 2020*, volume 11852, pages 203–212. SPIE, 2021.

[236] JP Bourgoin, Evan Meyer-Scott, Brendon L Higgins, B Helou, Chris Erven, Hannes Huebel, B Kumar, D Hudson, Ian D'Souza, Ralph Girard, et al. A comprehensive design and performance analysis of low earth orbit satellite quantum communication. *New Journal of Physics*, 15(2):023006, 2013.

[237] Valerio Lucarini. Tools for data analysis in optics, acoustics, signal processing. `https://www.mathworks.com/matlabcentral/fileexchange/8135-tools-for-data-analysis-in-optics-//acoustics-signal-processing`, 2023.

[238] Lucile Veissier, Charles W. Thiel, Thomas Lutz, Paul E. Barclay, Wolfgang Tittel, and Rufus L. Cone. Quadratic zeeman effect and spin-lattice relaxation of Tm^{3+}:YAG at high magnetic fields. *Physical Review B*, 94:205133, Nov 2016.

[239] Atia Amari, Andreas Walther, Mahmood Sabooni, Maomao Huang, Stefan Kröll, M Afzelius, I Usmani, B Lauritzen, N Sangouard, H De Riedmatten, et al. Towards an efficient atomic frequency comb quantum memory. *Journal of Luminescence*, 130(9):1579–1585, 2010.

[240] Mustafa Gündoğan, Patrick M. Ledingham, Kutlu Kutluer, Margherita Mazzera, and Hugues de Riedmatten. Solid state spin-wave quantum memory for time-bin qubits. *Physical Review Letters*, 114:230501, Jun 2015.

[241] N. Timoney, I. Usmani, P. Jobez, M. Afzelius, and N. Gisin. Single-photon-level optical storage in a solid-state spin-wave memory. *Physical Review A*, 88:022324, Aug 2013.

[242] Sebastian P Horvath, Mohammed K Alqedra, Adam Kinos, Andreas Walther, Jan Marcus Dahlström, Stefan Kröll, and Lars Rippe. Noise-free on-demand atomic frequency comb quantum memory. *Physical Review Research*, 3(2):023099, 2021.

[243] Subhojit Dutta, Yuqi Zhao, Uday Saha, Demitry Farfurnik, Elizabeth A Goldschmidt, and Edo Waks. An atomic frequency comb memory in rare-earth-doped thin-film lithium niobate. *ACS Photonics*, 10(4):1104–1109, 2023.

[244] Tian Zhong and Philippe Goldner. Emerging rare-earth doped material platforms for quantum nanophotonics. *Nanophotonics*, 8(11):2003–2015, 2019.

[245] Hassan Mallahzadeh. Cavity-enhanced waveguide quantum memory. Master's thesis, University of Calgary, 2015.

[246] Tian Zhong, Jonathan M Kindem, Evan Miyazono, and Andrei Faraon. Nanophotonic coherent light–matter interfaces based on rare-earth-doped crystals. *Nature Communications*, 6(1):8206, 2015.

[247] Tian Zhong, Jonathan M Kindem, Jake Rochman, and Andrei Faraon. Interfacing broadband photonic qubits to on-chip cavity-protected rare-earth ensembles. *Nature Communications*, 8(1):14107, 2017.

[248] Mi Lei, Rikuto Fukumori, Jake Rochman, Bihui Zhu, Manuel Endres, Joonhee Choi, and Andrei Faraon. Many-body cavity quantum electrodynamics with driven inhomogeneous emitters. *Nature*, 617(7960):271–276, 2023.

[249] Maximilian Ruf, Noel H Wan, Hyeongrak Choi, Dirk Englund, and Ronald Hanson. Quantum networks based on color centers in diamond. *Journal of Applied Physics*, 130(7), 2021.

[250] Manuel Grimm, Adrian Beckert, Gabriel Aeppli, and Markus Müller. Universal quantum computing using electronuclear wavefunctions of rare-earth ions. *PRX Quantum*, 2(1):010312, 2021.

[251] Nicklas Ohlsson, R Krishna Mohan, and Stefan Kröll. Quantum computer hardware based on rare-earth-ion-doped inorganic crystals. *Optics Communications*, 201(1-3):71–77, 2002.

[252] F Kimiaee Asadi, SC Wein, and C Simon. Protocols for long-distance quantum communication with single 167Er ions. *Quantum Science and Technology*, 5(4):045015, 2020.

[253] Hannes Bernien, Bas Hensen, Wolfgang Pfaff, Gerwin Koolstra, Machiel S Blok, Lucio Robledo, Tim H Taminiau, Matthew Markham, Daniel J Twitchen, Lilian Childress, et al. Heralded entanglement between solid-state qubits separated by three metres. *Nature*, 497(7447):86–90, 2013.

[254] Ruffin E Evans, Mihir K Bhaskar, Denis D Sukachev, Christian T Nguyen, Alp Sipahigil, Michael J Burek, Bartholomeus Machielse, Grace H Zhang, Alexander S Zibrov, Edward Bielejec, et al. Photon-mediated interactions between quantum emitters in a diamond nanocavity. *Science*, 362(6415):662–665, 2018.

[255] Matthew W Day, Kelsey M Bates, Christopher L Smallwood, Rachel C Owen, Tim Schröder, Edward Bielejec, Ronald Ulbricht, and Steven T Cundiff. Coherent interactions between silicon-vacancy centers in diamond. *Physical Review Letters*, 128(20):203603, 2022.

[256] A. N. Safonov, E. C. Lightowlers, Gordon Davies, P. Leary, R. Jones, and S. Öberg. Interstitial-carbon hydrogen interaction in silicon. *Physical Review Letters*, 77:4812–4815, Dec 1996.

[257] Diana Dhaliah, Yihuang Xiong, Alp Sipahigil, Sinéad M Griffin, and Geoffroy Hautier. First-principles study of the T center in silicon. *Physical Review Materials*, 6(5):L053201, 2022.

[258] Leigh S Martin and K Birgitta Whaley. Single-shot deterministic entanglement between non-interacting systems with linear optics. *arXiv preprint arXiv:1912.00067*, 2019.

[259] Stephen C Wein, Jia-Wei Ji, Yu-Feng Wu, Faezeh Kimiaee Asadi, Roohollah Ghobadi, and Christoph Simon. Analyzing photon-count heralded entanglement generation between solid-state spin qubits by decomposing the master-equation dynamics. *Physical Review A*, 102(3):033701, 2020.

[260] F Kimiaee Asadi, SC Wein, and Christoph Simon. Cavity-assisted controlled phase-flip gates. *Physical Review A*, 102(1):013703, 2020.

[261] Mahsa Karimi, Faezeh Kimiaee Asadi, Stephen C Wein, and Christoph Simon. Comparing the performance of practical two-qubit gates for individual ^{171}Yb ions in yttrium orthovanadate. *arXiv preprint arXiv:2410.23613*, 2024.

[262] Yuan Liang Lim, Almut Beige, and Leong Chuan Kwek. Repeat-until-success linear optics distributed quantum computing. *Physical Review Letters*, 95(3):030505, 2005.

[263] David L Moehring, Peter Maunz, Steve Olmschenk, Kelly C Younge, Dzmitry N Matsukevich, L-M Duan, and Christopher Monroe. Entanglement of single-atom quantum bits at a distance. *Nature*, 449(7158):68–71, 2007.

[264] Andrei Ruskuc, Chun-Ju Wu, Emanuel Green, Sophie LN Hermans, Joonhee Choi, and Andrei Faraon. Scalable multipartite entanglement of remote rare-earth ion qubits. *arXiv preprint arXiv:2402.16224*, 2024.

[265] Stephen Wein, Khabat Heshami, Christopher A Fuchs, Hari Krovi, Zachary Dutton, Wolfgang Tittel, and Christoph Simon. Efficiency of an enhanced linear optical Bell-state measurement scheme with realistic imperfections. *Physical Review A*, 94(3):032332, 2016.

[266] Thomas Grange, Gaston Hornecker, David Hunger, Jean-Philippe Poizat, Jean-Michel Gérard, Pascale Senellart, and Alexia Auffèves. Cavity-funneled generation of indistinguishable single photons from strongly dissipative quantum emitters. *Physical Review Letters*, 114(19):193601, 2015.

[267] DB Higginbottom, A DeAbreu, C Bowness, A Alizadeh, C Chartrand, NA Brunelle, ER MacQuarrie, NR Lee-Hone, M Ruether, M Kazemi, et al. Integrated silicon t centers for quantum technologies. In *Quantum Computing, Communication, and Simulation III*, volume 12446, pages 165–173. SPIE, 2023.

[268] Chang-Min Lee, Fariba Islam, Samuel Harper, Mustafa Atabey Buyukkaya, Daniel Higginbottom, Stephanie Simmons, and Edo Waks. High-efficiency single photon emission from a silicon T center in a nanobeam. *ACS Photonics*, 10(11):3844–3849, 2023.

[269] J Chang, JWN Los, JO Tenorio-Pearl, Niels Noordzij, R Gourgues, A Guardiani, JR Zichi, SF Pereira, HP Urbach, Val Zwiller, et al. Detecting telecom single photons with 99.5- 2.07+ 0.5% system detection efficiency and high time resolution. *APL Photonics*, 6(3), 2021.

[270] Dileep V Reddy, Robert R Nerem, Sae Woo Nam, Richard P Mirin, and Varun B Verma. Superconducting nanowire single-photon detectors with 98% system detection efficiency at 1550 nm. *Optica*, 7(12):1649–1653, 2020.

[271] Peng Hu, Hao Li, Lixing You, Heqing Wang, You Xiao, Jia Huang, Xiaoyan Yang, Weijun Zhang, Zhen Wang, and Xiaoming Xie. Detecting single infrared photons toward optimal system detection efficiency. *Optics Express*, 28(24):36884–36891, 2020.

[272] Alec Jenkins, Joanna W Lis, Aruku Senoo, William F McGrew, and Adam M Kaufman. Ytterbium nuclear-spin qubits in an optical tweezer array. *Physical Review X*, 12(2):021027, 2022.

[273] Camille Bowness, Simon A Meynell, Michael Dobinson, Chloe Clear, Kais Jooya, Nicholas Brunelle, Mehdi Keshavarz, Katarina Boos, Melanie Gascoine, Shahrzad Taherizadegan, et al. Laser-induced spectral diffusion and excited-state mixing of silicon T centres. *arXiv preprint arXiv:2504.09908*, 2025.

[274] Kinfung Ngan and Shuo Sun. Performance analysis of different photon-mediated entanglement generation schemes under optical dephasing and spectral diffusion. *arXiv preprint arXiv:2412.09976*, 2024.

[275] F Kimiaee Asadi, SC Wein, and Christoph Simon. Erratum to cavity-assisted controlled phase-flip gates. erratum in preparation, 2025.

[276] L-M Duan and HJ Kimble. Scalable photonic quantum computation through cavity-assisted interactions. *Physical Review Letters*, 92(12):127902, 2004.

[277] L-M Duan, B Wang, and HJ Kimble. Robust quantum gates on neutral atoms with cavity-assisted photon scattering. *Physical Review A*, 72(3):032333, 2005.

[278] Yun-Feng Xiao, Xiu-Min Lin, Jie Gao, Yong Yang, Zheng-Fu Han, and Guang-Can Guo. Realizing quantum controlled phase flip through cavity QED. *Physical Review A*, 70(4):042314, 2004.

[279] Chris O'Brien, Tian Zhong, Andrei Faraon, and Christoph Simon. Nondestructive photon detection using a single rare-earth ion coupled to a photonic cavity. *Physical Review A*, 94:043807, Oct 2016.

[280] DF Walls and Gerard J Milburn. Quantum information. In *Quantum Optics*, pages 307–346. Springer, 2008.

[281] Lieven MK Vandersypen and Isaac L Chuang. NMR techniques for quantum control and computation. *Reviews of Modern Physics*, 76(4):1037–1069, 2004.

[282] Charles D Hill, Eldad Peretz, Samuel J Hile, Matthew G House, Martin Fuechsle, Sven Rogge, Michelle Y Simmons, and Lloyd CL Hollenberg. A surface code quantum computer in silicon. *Science Advances*, 1(9):e1500707, 2015.

[283] Chloe Clear, Sara Hosseini, Amirhossein AlizadehKhaledi, Nicholas Brunelle, Austin Woolverton, Joshua Kanaganayagam, Moein Kazemi, Camille Chartrand, Mehdi Keshavarz, Yihuang Xiong, et al. Optical-transition parameters of the silicon T center. *Physical Review Applied*, 22(6):064014, 2024.

[284] Erika Janitz, Mihir K Bhaskar, and Lilian Childress. Cavity quantum electrodynamics with color centers in diamond. *Optica*, 7(10):1232–1252, 2020.

[285] Chris O'Brien, Tian Zhong, Andrei Faraon, and Christoph Simon. Nondestructive photon detection using a single rare-earth ion coupled to a photonic cavity. *Physical Review A*, 94(4):043807, 2016.

[286] Frederik Thiele, Niklas Lamberty, Thomas Hummel, Nina A Lange, Lorenzo M Procopio, Aishi Barua, Sebastian Lengeling, Viktor Quiring, Christof Eigner, Christine Silberhorn, et al. Cryogenic feedforward of a photonic quantum state. *Optica*, 12(5):720–727, 2025.

[287] J Metz and SD Barrett. Effect of frequency-mismatched photons in quantum-information processing. *Physical Review A—Atomic, Molecular, and Optical Physics*, 77(4):042323, 2008.

[288] Benjamin Kambs and Christoph Becher. Limitations on the indistinguishability of photons from remote solid state sources. *New Journal of Physics*, 20(11):115003, 2018.

[289] Mehmet T Uysal and Jeff D Thompson. Rephasing spectral diffusion in time-bin spin-spin entanglement protocols. *Physical Review A*, 110(5):052606, 2024.

[290] Xueyue Zhang, Niccolo Fiaschi, Lukasz Komza, Hanbin Song, Thomas Schenkel, and Alp Sipahigil. Laser-induced spectral diffusion of t centers in silicon nanophotonic devices. *arXiv preprint arXiv:2504.08898*, 2025.

[291] DL McAuslan, Jevon Joseph Longdell, and MJ Sellars. Strong-coupling cavity QED using rare-earth-metal-ion dopants in monolithic resonators: What you can do with a weak oscillator. *Physical Review A—Atomic, Molecular, and Optical Physics*, 80(6):062307, 2009.

[292] F Kimiaee Asadi, N Lauk, S Wein, N Sinclair, C O'Brien, and C Simon. Quantum repeaters with individual rare-earth ions at telecommunication wavelengths. *Quantum*, 2:93, 2018.

[293] Jia-Wei Ji, Yu-Feng Wu, Stephen C Wein, Faezeh Kimiaee Asadi, Roohollah Ghobadi, and Christoph Simon. Proposal for room-temperature quantum repeaters with nitrogen-vacancy centers and optomechanics. *Quantum*, 6:669, 2022.

[294] Filip Rozpędek, Raja Yehia, Kenneth Goodenough, Maximilian Ruf, Peter C Humphreys, Ronald Hanson, Stephanie Wehner, and David Elkouss. Near-term quantum-repeater experiments with nitrogen-vacancy centers: Overcoming the limitations of direct transmission. *Physical Review A*, 99(5):052330, 2019.

[295] D Main, P Drmota, DP Nadlinger, EM Ainley, A Agrawal, BC Nichol, R Srinivas, G Araneda, and DM Lucas. Distributed quantum computing across an optical network link. *Nature*, pages 1–6, 2025.

Appendix A

Copyright permissions

This appendix provides the copyright permissions required for the inclusion of first and second papers in this thesis.

A.1 Journals copyright permissions

Each of these papers is published in a journal that allows its inclusion in this thesis. Figures A.1-A.3 present screenshots from the journal websites as proof of permission.

A.2 Co-authors permissions

My co-authors have also agreed to the inclusion of material from our joint publications in this thesis. The relevant confirmations are shown in figures A.4-A.10.

- Christoph Simon, Fig. A.4
- Daniel Oblak, Fig. A.5
- Daniel Higginbottom, Fig. A.6
- Jacob H. Davidson, Fig. A.7

- Sourabh Kumar, Fig. A.8
- Faezeh Kimiaee Asadi, Fig. A.9
- Jia-Wei Ji, Fig. A.10

A.3 Permission to include figures 2.3 and 5.3

For including figure 2.3 in my thesis, I obtained the permission from both the journal and the lead author. The corresponding confirmations are shown in figures A.11-A.13. For including figure 5.3 in my thesis, I obtained the permission from the lead author. The corresponding confirmation is shown in figure A.14.

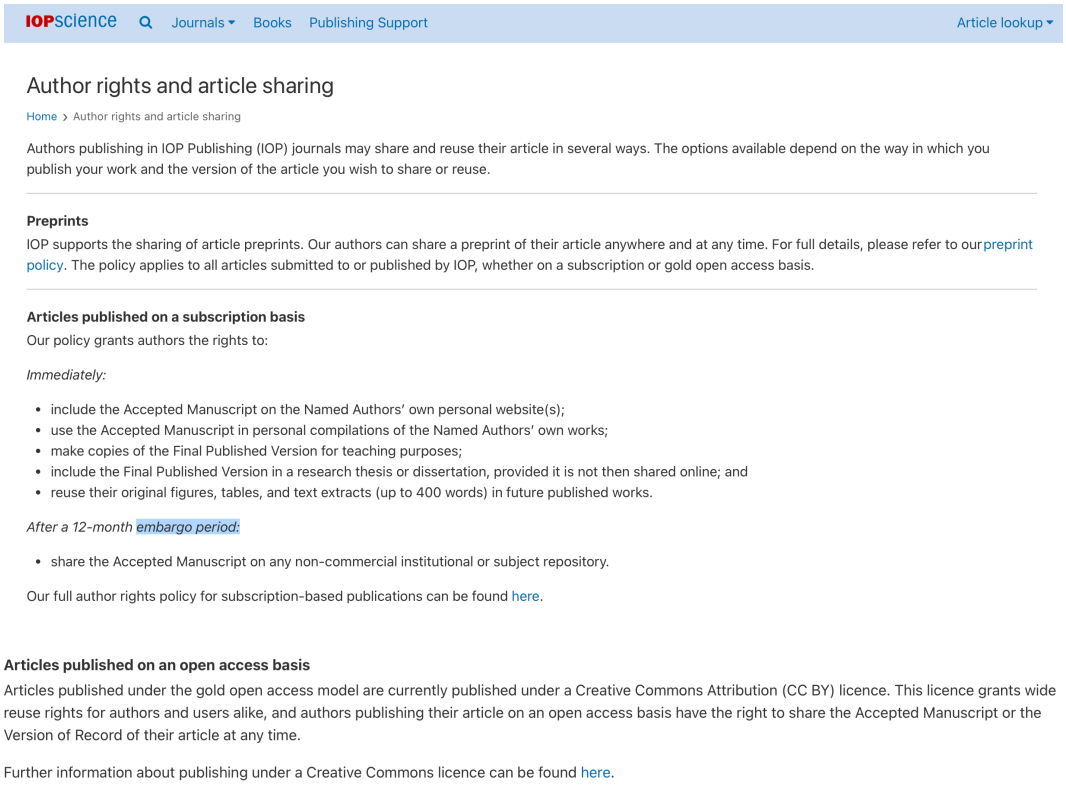

IOPscience Journals Books Publishing Support Article lookup

Author rights and article sharing

Home › Author rights and article sharing

Authors publishing in IOP Publishing (IOP) journals may share and reuse their article in several ways. The options available depend on the way in which you publish your work and the version of the article you wish to share or reuse.

Preprints

IOP supports the sharing of article preprints. Our authors can share a preprint of their article anywhere and at any time. For full details, please refer to our preprint policy. The policy applies to all articles submitted to or published by IOP, whether on a subscription or gold open access basis.

Articles published on a subscription basis

Our policy grants authors the rights to:

Immediately:

- include the Accepted Manuscript on the Named Authors' own personal website(s);
- use the Accepted Manuscript in personal compilations of the Named Authors' own works;
- make copies of the Final Published Version for teaching purposes;
- include the Final Published Version in a research thesis or dissertation, provided it is not then shared online; and
- reuse their original figures, tables, and text extracts (up to 400 words) in future published works.

After a 12-month embargo period:

- share the Accepted Manuscript on any non-commercial institutional or subject repository.

Our full author rights policy for subscription-based publications can be found here.

Articles published on an open access basis

Articles published under the gold open access model are currently published under a Creative Commons Attribution (CC BY) licence. This licence grants wide reuse rights for authors and users alike, and authors publishing their article on an open access basis have the right to share the Accepted Manuscript or the Version of Record of their article at any time.

Further information about publishing under a Creative Commons licence can be found here.

Figure A.1: Copyright confirmation for first paper, published open access in Quantum Science and Technology, an Institute of Physics (IOPscience) journal.

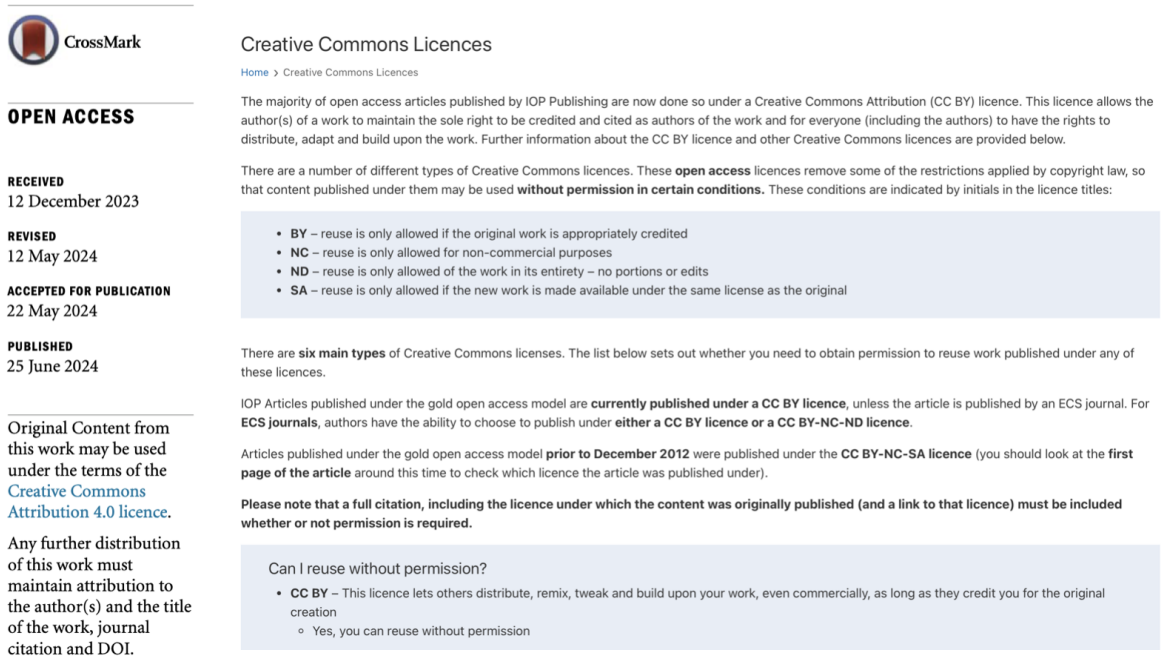

CrossMark

OPEN ACCESS

RECEIVED
12 December 2023

REVISED
12 May 2024

ACCEPTED FOR PUBLICATION
22 May 2024

PUBLISHED
25 June 2024

Creative Commons Licences

Home › Creative Commons Licences

The majority of open access articles published by IOP Publishing are now done so under a Creative Commons Attribution (CC BY) licence. This licence allows the author(s) of a work to maintain the sole right to be credited and cited as authors of the work and for everyone (including the authors) to have the rights to distribute, adapt and build upon the work. Further information about the CC BY licence and other Creative Commons licences are provided below.

There are a number of different types of Creative Commons licences. These **open access** licences remove some of the restrictions applied by copyright law, so that content published under them may be used **without permission in certain conditions.** These conditions are indicated by initials in the licence titles:

- **BY** – reuse is only allowed if the original work is appropriately credited
- **NC** – reuse is only allowed for non-commercial purposes
- **ND** – reuse is only allowed of the work in its entirety – no portions or edits
- **SA** – reuse is only allowed if the new work is made available under the same license as the original

There are **six main types** of Creative Commons licenses. The list below sets out whether you need to obtain permission to reuse work published under any of these licences.

IOP Articles published under the gold open access model are **currently published under a CC BY licence**, unless the article is published by an ECS journal. For **ECS journals**, authors have the ability to choose to publish under **either a CC BY licence or a CC BY-NC-ND licence**.

Articles published under the gold open access model **prior to December 2012** were published under the **CC BY-NC-SA licence** (you should look at the **first page of the article** around this time to check which licence the article was published under).

Please note that a full citation, including the licence under which the content was originally published (and a link to that licence) must be included whether or not permission is required.

Can I reuse without permission?

- **CC BY** – This licence lets others distribute, remix, tweak and build upon your work, even commercially, as long as they credit you for the original creation
  - Yes, you can reuse without permission

Figure A.2: Illustration of the open access license associated with the first paper, published in Quantum Science and Technology (IOPscience). The left panel specifies the Creative Commons Attribution 4.0 (CC BY 4.0) licence applied to the paper, while the right panel provides the corresponding terms and conditions under which the work may be reused.

arXiv Permissions and Reuse

will appear, such as at arXiv:2201.04182.

Home
About
Help
arXiv Help Contents
Submit an Article
Find and Read Articles
Finding Articles

I want to include a paper of mine from arXiv in my thesis, do I need specific permission?

If you are the copyright holder of the work, you do not need arXiv's permission to reuse the full text.

Figure A.3: Copyright confirmation for second paper, available as a preprint on arXiv.

Outlook

Re: Request for permission to include publications in thesis

From Christoph Simon
Date Thu 14/08/2025 10:19
To Shahrzad Taheri

[△EXTERNAL]

Hi Shahrzad,
You have my permission.
Best,
Christoph

On Thu, Aug 14, 2025 at 10:09 AM Shahrzad Taheri wrote:

> Hi Christoph,
>
> I would like to include the following two papers in my thesis and wanted to confirm that you are okay with this. Could you please send me a short email granting permission?
>
> 1. Taherizadegan, S., Kimiaee Asadi, F., Ji, J.-W., Higginbottom, D., and Simon, C. *Exploring the feasibility of various quantum gates between T centers in silicon*. arXiv preprint arXiv:2508.06474, 2025.
>
> 2. Taherizadegan, S., Davidson, J. H., Kumar, S., Oblak, D., and Simon, C. *Towards a Realistic Model for Cavity-Enhanced Atomic Frequency Comb Quantum Memories*. Quantum Science and Technology, 9(3):035049, 2024.
>
> Thank you,
> Shahrzad

Figure A.4: Permission e-mail from Christoph Simon regarding inclusion of his co-authored papers in this thesis

Outlook

Re: Request for permission to include publication in thesis

From Daniel Oblak
Date Thu 14/08/2025 11:01
To Shahrzad Taheri

Hello Shahrzad,

Yes, I grant you permission to include the paper in your PhD thesis.

Best
Daniel

From: Shahrzad Taheri
Sent: Thursday, August 14, 2025 10:18:32 AM
To: Daniel Oblak
Subject: Request for permission to include publication in thesis

Hi Daniel,

I would like to include the following paper in my thesis and wanted to confirm that you are okay with this. Could you please send me a short email granting permission?

> Taherizadegan, S., Davidson, J. H., Kumar, S., Oblak, D., and Simon, C. *Towards a Realistic Model for Cavity-Enhanced Atomic Frequency Comb Quantum Memories*. Quantum Science and Technology, 9(3):035049, 2024.

Thank you,
Shahrzad

Figure A.5: Permission e-mail from Daniel Oblak regarding inclusion of his co-authored papers in this thesis

Outlook

RE: Request for permission to include publication in thesis

From Daniel Higginbottom
Date Thu 14/08/2025 10:20
To Shahrzad Taheri

[△EXTERNAL]

Yes of course 😊

Best regards,
Daniel

From: Shahrzad Taheri
Sent: Thursday, August 14, 2025 9:12 AM
To: Daniel Higginbottom
Subject: Request for permission to include publication in thesis

Hi Daniel,

I would like to include the following paper in my thesis and wanted to confirm that you are okay with this. Could you please send me a short email granting permission?

1. Taherizadegan, S., Kimiaee Asadi, F., Ji, J.-W., Higginbottom, D., and Simon, C. *Exploring the feasibility of various quantum gates between T centers in silicon*. arXiv preprint arXiv:2508.06474, 2025.

Thank you,
Shahrzad

Figure A.6: Permission e-mail from Daniel Higginbottom regarding inclusion of his co-authored papers in this thesis

Outlook

Re: Request for permission to include publication in thesis

From Jake Davidson
Date Thu 14/08/2025 13:40
To Shahrzad Taheri

[△EXTERNAL]

Hi Shahrzad, I grant permission for you to use this paper in your thesis!

Congratulations!

Cheers,
-Jake

On Thu, Aug 14, 2025, 12:16 PM Shahrzad Taheri wrote:

> Hi Jake,
>
> I would like to include the following paper in my thesis and wanted to confirm that you are okay with this. Could you please send me a short email granting permission?
>
> > Taherizadegan, S., Davidson, J. H., Kumar, S., Oblak, D., and Simon, C. *Towards a Realistic Model for Cavity-Enhanced Atomic Frequency Comb Quantum Memories*. Quantum Science and Technology, 9(3):035049, 2024.
>
> Thank you,
> Shahrzad

Figure A.7: Permission e-mail from Jacob H. Davidson regarding inclusion of his co-authored papers in this thesis

Outlook

Re: Request for permission to include publication in thesis

From Sourabh Kumar
Date Fri 15/08/2025 14:20
To Shahrzad Taheri

Hi Shahrzad,

Yes, it's alright. All the best for your defense!

Best,
Sourabh

From: Shahrzad Taheri
Sent: Thursday, August 14, 2025 10:17:42 AM
To: Sourabh Kumar
Subject: Request for permission to include publication in thesis

Hi Sourabh,

I would like to include the following paper in my thesis and wanted to confirm that you are okay with this. Could you please send me a short email granting permission?

> Taherizadegan, S., Davidson, J. H., Kumar, S., Oblak, D., and Simon, C. *Towards a Realistic Model for Cavity-Enhanced Atomic Frequency Comb Quantum Memories*. Quantum Science and Technology, 9(3):035049, 2024.

Thank you,
Shahrzad

Figure A.8: Permission e-mail from Sourabh Kumar regarding inclusion of his co-authored papers in this thesis

Outlook

Re: Request for permission to include publication in thesis

From Faezeh Kimiaee Asadi
Date Thu 14/08/2025 17:22
To Shahrzad Taheri

[△EXTERNAL]

Hi Shahrzad,

Sure, You have my permission to include it.

Cheers,
Faezeh

On Thu, Aug 14, 2025 at 10:13 AM Shahrzad Taheri wrote:

> Hi Faezeh,
>
> I would like to include the following paper in my thesis and wanted to confirm that you are okay with this. Could you please send me a short email granting permission?
>
> > Taherizadegan, S., Kimiaee Asadi, F., Ji, J.-W., Higginbottom, D., and Simon, C. *Exploring the feasibility of various quantum gates between T centers in silicon*. arXiv preprint arXiv:2508.06474, 2025.
>
> Thank you,
> Shahrzad

Figure A.9: Permission e-mail from Faezeh Kimiaee Asadi regarding inclusion of his co-authored papers in this thesis

Outlook

Re: Request for permission to include publication in thesis

From Jiawei Ji
Date Thu 14/08/2025 10:20
To Shahrzad Taheri

Hi Shahrzad,

Of course! You have my permission to include this paper in your thesis.

Cheers,
Jiawei

From: Shahrzad Taheri
Date: Thursday, August 14, 2025 at 10:14 am
To: Jiawei Ji
Subject: Request for permission to include publication in thesis

Hi Jiawei,

I would like to include the following paper in my thesis and wanted to confirm that you are okay with this. Could you please send me a short email granting permission?

1. Taherizadegan, S., Kimiaee Asadi, F., Ji, J.-W., Higginbottom, D., and Simon, C. *Exploring the feasibility of various quantum gates between T centers in silicon*. arXiv preprint arXiv:2508.06474, 2025.

Thank you,
Shahrzad

Figure A.10: Permission e-mail from Jia-Wei Ji regarding inclusion of his co-authored papers in this thesis

American Physical Society
Reuse and Permissions License

03-Sep-2025

This license agreement between the American Physical Society ("APS") and Shahrzad Taherizadegan ("You") consists of your license details and the terms and conditions provided by the American Physical Society and SciPris.

Licensed Content Information

License Number:	**RNP/25/SEP/096174**
License date:	03-Sep-2025
DOI:	10.1103/PhysRevLett.101.203601
Title:	Multimodal Properties and Dynamics of Gradient Echo Quantum Memory
Author:	G. Hétet et al.
Publication:	Physical Review Letters
Publisher:	American Physical Society
Cost:	USD $ 0.00

Request Details

Does your reuse require significant modifications: No

Specify intended distribution locations:	Worldwide
Reuse Category:	Reuse in a thesis/dissertation
Requestor Type:	Student
Items for Reuse:	Figures/Tables
Number of Figure/Tables:	1
Figure/Tables Details:	Figure 1 in the paper
Format for Reuse:	Electronic

Information about New Publication:

University/Publisher:	University of Calgary
Title of dissertation/thesis:	Toward realistic elements for long-distance quantum networks with solid-state spin systems
Author(s):	Shahrzad Taherizadegan
Expected completion date:	Sep. 2025

License Requestor Information

Name:	Shahrzad Taherizadegan
Affiliation:	Individual
Country:	Canada

Figure A.11: Permission from the journal to reproduce the figure in this thesis (first page).

American Physical Society
Reuse and Permissions License

TERMS AND CONDITIONS

The American Physical Society (APS) is pleased to grant the Requestor of this license a non-exclusive, non-transferable permission, limited to Electronic format, provided all criteria outlined below are followed.

1. You must also obtain permission from at least one of the lead authors for each separate work, if you haven't done so already. The author's name and affiliation can be found on the first page of the published Article.
2. For electronic format permissions, Requestor agrees to provide a hyperlink from the reprinted APS material using the source material's DOI on the web page where the work appears. The hyperlink should use the standard DOI resolution URL, http://dx.doi.org/{DOI}. The hyperlink may be embedded in the copyright credit line.
3. For print format permissions, Requestor agrees to print the required copyright credit line on the first page where the material appears: "Reprinted (abstract/excerpt/figure) with permission from [(FULL REFERENCE CITATION) as follows: Author's Names, APS Journal Title, Volume Number, Page Number and Year of Publication.] Copyright (YEAR) by the American Physical Society."
4. Permission granted in this license is for a one-time use and does not include permission for any future editions, updates, databases, formats or other matters. Permission must be sought for any additional use.
5. Use of the material does not and must not imply any endorsement by APS.
6. APS does not imply, purport or intend to grant permission to reuse materials to which it does not hold copyright. It is the requestor's sole responsibility to ensure the licensed material is original to APS and does not contain the copyright of another entity, and that the copyright notice of the figure, photograph, cover or table does not indicate it was reprinted by APS with permission from another source.
7. The permission granted herein is personal to the Requestor for the use specified and is not transferable or assignable without express written permission of APS. This license may not be amended except in writing by APS.
8. You may not alter, edit or modify the material in any manner.
9. You may translate the materials only when translation rights have been granted.
10. APS is not responsible for any errors or omissions due to translation.
11. You may not use the material for promotional, sales, advertising or marketing purposes.
12. The foregoing license shall not take effect unless and until APS or its agent, Aptara, receives payment in full in accordance with Aptara Billing and Payment Terms and Conditions, which are incorporated herein by reference.
13. Should the terms of this license be violated at any time, APS or Aptara may revoke the license with no refund to you and seek relief to the fullest extent of the laws of the USA. Official written notice will be made using the contact information provided with the permission request. Failure to receive such notice will not nullify revocation of the permission.
14. APS reserves all rights not specifically granted herein.
15. This document, including the Aptara Billing and Payment Terms and Conditions, shall be the entire agreement between the parties relating to the subject matter hereof.

Figure A.12: Permission from the journal to reproduce the figure in this thesis (second page).

Outlook

Re: Permission to reuse Figure 1 from PRL 101, 203601 (2008) in my PhD thesis

From gabriel hetet
Date Fri 05/09/2025 00:42
To Shahrzad Taheri

[ΔEXTERNAL]

Dear Shahrzad,

No problems !

I grant Shahrzad Taherizadegan permission to reproduce Figure 1 from Hétet et al., Phys. Rev. Lett. 101, 203601 (2008), in her doctoral thesis.

Best, and good luck with the writing !

Gabriel

Le 05/09/2025 à 02:06, Shahrzad Taheri a écrit :

> Dear Dr. Hétet,
>
> My name is Shahrzad Taherizadegan, a PhD candidate at the University of Calgary. I have defended my PhD and am finalizing my thesis for submission. I would like to include Figure 1 from your paper, “Multimodal Properties and Dynamics of Gradient Echo Quantum Memory,” Phys. Rev. Lett. 101, 203601 (2008) (DOI: 10.1103/PhysRevLett.101.203601), in my thesis.
> I have obtained an APS reuse license for this one-time, non-commercial use (copy attached). As APS requests, I’m also seeking permission from a lead author. Would you kindly grant permission for me to reproduce Figure 1 in the electronic version of my thesis? I will not modify the figure and will include the full citation and DOI hyperlink.
> If convenient, a brief reply such as the following would be perfect:
> “I grant Shahrzad Taherizadegan permission to reproduce Figure 1 from Hétet et al., Phys. Rev. Lett. 101, 203601 (2008), in her doctoral thesis.”
> Thank you very much for your time and consideration.
>
> Best regards,
> Shahrzad Taherizadegan

Figure A.13: Permission from Gabriel Hetet to reproduce the figure in this thesis.

Outlook

Re: Permission to reuse Figure 1 (c) from arXiv:1912.00067 in my PhD thesis

From Leigh S Martin
Date Fri 12/09/2025 09:38
To Shahrzad Taheri

[ΔEXTERNAL]

Hi Shahrzad,

Yes, please feel free to use the figure!

I grant Shahrzad Taherizadegan permission to reproduce Figure 1 (c) from Martin et al., arXiv:1912.00067 (2019), in her doctoral thesis.

Could you send me a PDF of your thesis when it is done? I'd be curious to learn more.

Best wishes,

Leigh

El vie, 12 de sept de 2025, 07:38, Shahrzad Taheri escribió:

> Dear Dr. Martin,
>
> My name is Shahrzad Taherizadegan, a PhD candidate at the University of Calgary. I have defended my PhD and am finalizing my thesis for submission. I would like to include Figure 1 (c) from your arxiv paper, "**Single-shot deterministic entanglement between non-interacting systems with linear optics**,"arXiv:1912.00067, in my thesis.
>
> Would you kindly grant permission for me to reproduce Figure 1 (c) in the electronic version of my thesis? I will not modify the figure and will include the full citation.
> If convenient, a brief reply such as the following would be perfect:
>
> "I grant Shahrzad Taherizadegan permission to reproduce Figure 1 (c) from Martin et al.,

Figure A.14: Permission from Leigh Martin to reproduce the figure in this thesis.